

Gradient Field Transduction of Nanomechanical Resonators

Dissertation
an der Fakultät für Physik
der Ludwig–Maximilians–Universität
München



vorgelegt von
Quirin P. Unterreithmeier
aus Augsburg

München, August 2010

Gradient Field Transduction of Nanomechanical Resonators

Dissertation
an der Fakultät für Physik
der Ludwig-Maximilians-Universität München



vorgelegt von
Quirin P. Unterreithmeier
aus Augsburg

München, August 2010

Erstgutachter: Prof. Dr. J. P. Kotthaus

Zweitgutachter: Prof. Dr. W. Zwerger

Tag der mündlichen Prüfung: 21.10.2010

"On ne finit pas un œuvre, on l'abandonne."
Gustave Flaubert

Zusammenfassung

Das Forschungsgebiet nanomechanischer Systeme betrachtet die Bewegung von Strukturen, deren Länge in mindestens einer Richtung deutlich unter einem Mikrometer liegt. Meist werden dabei Auslenkungen untersucht, die in der Nähe einer mechanischen Resonanz angetrieben werden. Das wissenschaftliche Interesse an solchen Strukturen hat mehrere Gründe: aufgrund der kleinen Masse und oftmals geringen Dämpfung (d.h. hohe Güte) reagieren solche nanomechanischen Systeme sehr empfindlich auf Änderungen ihrer Umgebung oder ihrer eigenen Eigenschaften wie etwa ihrer Masse. Die große Vielfalt der nanomechanischen Systeme erlaubt die Kopplung an verschiedenste physikalische Größen wie (Umgebungs-)Druck, Licht, elektrische/magnetische Felder. Dies ermöglicht, die Wechselwirkung selbst zu untersuchen oder entsprechende Änderungen empfindlich zu detektieren.

Im Rahmen der vorliegenden Arbeit wurde die Resonator Bewegung von doppelseitig eingespannten Balken untersucht; diese wurden mit konventioneller Mikrofabrikation aus verspanntem Silizium-Nitrid gefertigt. Die große Zugspannung in den Balken führt zu einer hohen mechanischen Stabilität und ebenso zu hohen mechanischen Güten.

Ein Teil der Arbeit befasste sich mit der Entwicklung neuer Detektions- und Antriebsmechanismen. Unter Ausnutzung der Polarisierbarkeit des Resonators wurde ein lokaler Antrieb realisiert, der sich durch besondere Einfachheit auszeichnet. Ebenso wurden Fortschritte in der optischen Detektion erzielt. Ein Photodetektor konnte innerhalb einer optischen Wellenlänge Abstand zum Resonator plaziert werden; dies ermöglicht die lokale Detektion seiner Bewegung.

Hochempfindliche Messungen nutzen oft optische Resonanzen; bisherige Umsetzungen basieren auf Reflexionen und sind daher auf Objekte beschränkt, die größer als die verwendete Wellenlänge sind. In einer Zusammenarbeit mit Prof. Kippenberge konnte diese Beschränkung umgangen werden, indem geführtes Licht in einem Mikro-Toroiden verwendet wurde.

Weiter wurde in der Arbeit die resonante Bewegung selbst untersucht. Im Bereich hoher Amplituden zeigt die rücktreibende Kraft nichtlineares Verhalten. Das sich dadurch ergebende bistabile Verhalten des Resonators wurde mit Hilfe von kurzen, resonanten Pulsen untersucht; schnelles Schalten wurde erreicht.

Die mechanische Dämpfung der Siliziumnitrid Resonatoren wurde untersucht. Die hohen Güten von Systemen unter Zugspannung konnte erklärt werden durch

die sich ergebende erhöhte gespeicherte elastische Energie; im Gegensatz zu einem veränderten Dämpfungsverhalten.

Abstract

In the field of nanomechanical systems the mechanical motion of objects is studied that have at least one dimension that is well below 1 μm . In most yet not all cases the displacement is studied when exciting near a mechanical resonance. They attract scientific attention for several reasons: because of their small masses and their often little mechanical damping, that is high mechanical quality factors, these systems sensitively react to changes in their environment as well as to changes of their own properties such as their mass. In addition, the huge variety of nanomechanical systems facilitates the optimization of coupling these to very diverse physical quantities such as ambient pressure, (visible) light, electro/magnetostatic fields and mass. This enables to either study the interaction itself or to measure such changes with high precision.

In the framework of this thesis the resonant motion of a doubly clamped beam was investigated that was fabricated by conventional top-down lithographic methods from pre-stressed silicon nitride. The mechanical beams are therefore under high tensile stress resulting in an exceptional structural stability as well as high mechanical quality factors.

As part of this thesis new transduction mechanisms were developed. The polarizability of the resonator has been utilized to create a local and widely applicable dielectric transduction scheme. Several advances have been achieved concerning the interferometric detection of nanomechanical displacement. Creating a photodetector within a distance on the order of an optical wavelength to the resonator enabled the local optical detection of its motion.

In order to increase the detection sensitivity optical resonances are employed; previous implementations however suffer from their restriction to objects larger than the wavelength because they rely on specular reflection. In a cooperation with the group of Prof. Kippenberg a setup was realized that overcomes this limitation using near-field coupling to guided light circulating in micro-toroid.

Apart from the task of transduction, the resonant motion of the nanomechanical beams itself was investigated: oscillating at high amplitudes, the restoring force exhibits nonlinear terms. In the resulting bistable regime, additional short pulses are utilized to map the stability diagram and enable fast switching of a nanomechanical memory element.

The mechanical damping of the fabricated silicon nitride resonators has been

studied. In particular the high quality factors exhibited by the pre-stressed nanobeams could be deduced to be a result of the increased stored elastic energy with pre-stress rather than a large modification of the damping characteristics.

Contents

Introduction	1
Scope of the thesis	2
References	5
1 Dielectric Transduction	9
References	13
2 Stroboscopic Downconversion	15
References	19
3 Near-field cavity optomechanics	21
References	25
4 On-chip Interferometric Detection	27
References	31
5 Nonlinear Switching Dynamics	33
References	37
6 Damping Characteristics	39
References	43
Summary and Perspectives	45
References	49
A Universal transduction scheme for nanomechanical systems based on dielectric forces	51
B Coherent detection of nonlinear nanomechanical motion using a stroboscopic downconversion technique	55
C Near-field cavity optomechanics with nanomechanical oscillators technique	59
D On-Chip Interferometric Detection of Nanomechanical Motion	65

E	Nonlinear switching dynamics in a nanomechanical resonator	69
F	Damping of Nanomechanical Resonators	73
G	Supporting Information	77
G.1	Frequency of a pulled string	77
G.2	Supplement to Dielectric Actuation	78
G.2.1	Electrical heat dissipation	78
G.2.2	Electrical sensitivity	78
G.2.3	Long-term drift of the resonance frequency	79
G.3	Nonlinear characteristics of a vibrating pre-stressed string	79
G.4	Supplement to On-chip Detection	81
G.4.1	Device Dimensions	81
G.4.2	Heating of the beam	81
G.5	Perturbation solution of the Duffing equation	82
G.6	Supplement to Damping Characteristics	84
G.6.1	Damping Model	84
G.6.2	Elastic Energy of a Pre-Stressed Beam	85
G.6.3	Frequency-dependent Loss Modulus	86
G.6.4	Linewidth of the Mechanical Resonance	86
G.6.5	Microscopic Damping Mechanisms	87
G.6.6	Reduced Quality Factor	88
G.6.7	Spatially Inhomogeneous Loss Modulus	89
G.7	Nonlinear Damping	90
	References	93
	Danksagung	95
	Lebenslauf	97

Introduction

Since the development of the first centimeter-sized transistor developed 1947 at the Bell Labs [1], a rapid technical development emerged that now allows the fabrication of structures with sizes that are well below 100 nm. Whereas the focus of this development was primarily to produce ever-faster electrical logics, the techniques can be equally employed to create mechanical structures of small sizes.

This enables mass-fabrication as well as the integration of mechanical systems to electrical circuits [2–4], leading to the development of so-called Microelectromechanical Systems (MEMS). Depending on the desired task, these can be processed to have high quality factors [4–6], small spring constants [7, 8] and high frequencies [4, 5]. A variety of applications has emerged, including frequency filters [4, 9], chemical sensors [10, 11] and ultra-sensitive force sensors capable of detecting the presence of few nuclear spins [12], single electrons [13], or dipolar forces [14]. It is noteworthy that force sensitivity scales inversely with resonance frequency; high resolution setups therefore incorporate long and soft cantilevers that are attributed to the MEMS regime [7, 12].

In a ground-breaking work performed by Cleland and Roukes a further reduction in the size of the mechanical element was achieved [15], leading to a sub-micron sized paddle oscillator capable of detecting charge variations of less than a single electron [16]. As the characteristic length scales of the employed resonators are partly well below 1 μm , these are called Nanoelectromechanical Systems (NEMS).

Their most notably different parameter when compared with MEMS probably is the reduced mass, leading to a very high mass resolution when implemented as sensors [17, 18]. The low mass translates into fairly low spring constants at high frequencies, a favorable combination when a coherent quantum mechanical control of the mechanical element is aimed at [19].

However, reducing the size is accompanied with several obstacles: the smaller size typically complicates the transduction of the resonator motion; oscillators used in AFM scanning setups are still based on MEMS. Another example of this difficulty can be inferred from the fact that the first and still sole demonstrated resonator observed in its quantum mechanical ground state is a MEMS resonator [20].

In addition, with decreasing size the surface-to-volume ratio increases; as the fabrication typically introduces surface defects, the quality factor of the structures degrade [6, 21–23].

Yet, the nanoscopic world may offer a unique solution to this latter problem:

several NEMS resonator have recently been demonstrated that were fabricated by chemical growth, avoiding the top-down fabrication. Thereby, ultra-clean resonators have been achieved [24, 25]. In addition, such resonators can be composed of materials that are inherently reduced in their dimensionality d , namely carbon nanotubes [25, 26] (1d) and graphene [27] (2d). Such materials avoid any intrinsic compositional or sterical impurities that cause dissipation [28, 29], as the entire material likewise forms the surface. Such implementations of mechanical resonators also seem to represent the ultimate reduction in size.

Scope of the thesis

The present work is organized as follows: as it is cumulative; each chapter (1 - 6) is a summary of a publication that can be found in the appendix (A - F). A redundancy of information is therefore unavoidable, yet enables the independent readability, which is hopefully of convenience to the reader. Although new processing techniques have been developed, these are not presented as a separate chapter, because these have been described in detail elsewhere [30]. Additional information, including the supplement of the publications and calculations can be found in the appendix; the thesis is concluded by a discussion of possible continuations. In the following, a short overview of each project is given.

Throughout this thesis, the resonant motion of high aspect ratio nanomechanical beams is investigated; these are fabricated from silicon nitride layers that are under high tensile stress. As a result, the released strings are subject to a high pre-stress of approximately 830 MPa. The experiments are carried at room temperature and in vacuum to avoid gas damping.

Chapter 1 of this work deals with the above mentioned problem of transducing the nanomechanical motion, presenting a near-field scheme that solely relies on the polarizability of the nanomechanical beams. As a result, it was possible for the first time to locally transduce the motion of the resonator using electrical signals without introducing any restriction on material or additional mechanical damping. The latter problem is commonly associated with electric transduction, as most schemes necessitate the deposition of conducting metal onto the resonator that has been shown to introduce large mechanical damping [31]. The experimental realization consist of two metal wires placed besides and oriented along the resonator and is therefore very easy to implement.

Chapter 2 demonstrates an optical stroboscopic implementation of the well-established down-conversion method. Such methods avoid the processing of high frequency signals by introducing a suitable modulation of the detection signal [32, 33]. In the experiment an intensity-modulated light beam is focused onto the resonator and the reflection is analyzed, similar to [34]. As the displacement of the beam causes an additional intensity modulation, it is now possible to detect the beating of the

two signals, whose frequency can be chosen at will. Thereby the bandwidth of the employed photodetector imposes no longer a restriction, enabling here the detection of higher order mechanical modes. Based on the observed frequency spectrum and the nonlinear characteristics of the mechanical oscillation, it was possible for the first time, to quantitatively measure the elastic parameter of the strained resonator.

In chapter 3 a very sophisticated setup to transduce the nanomechanical displacement is introduced. Compared to the previous chapter, the focus here is not (yet) to provide a simple and widely applicable detection scheme; it is rather a high precision setup to sensitively detect the displacement of a nanomechanical object. Sensitive optical schemes incorporate optical cavities, see e.g. [35–38]; the measured object forms one end of the cavity [35–37], or is placed within the light field [38]. However, reducing the size of the mechanical object introduces scattering of the photons out of the cavity or limits the interaction strength with the light field. In both cases the transduction sensitivity reduces. To circumvent this limitation, the optical resonance of a micro toroid is chosen [39]; the mechanical nanoresonator is placed in the near-field of the toroid; its displacement thereby causes a shift in the optical resonance frequency. The effect of scattering in this configuration is shown to be negligible.

The next chapter (4) also deals with detection of nanomechanical motion. It represents a combination of electrical and optical detection: the detection mechanism still relies on an interference effect. However, complementary to previous realizations [40] the resulting optical intensity modulation caused by the beam displacement is now detected in the near-field of the mechanical element. This enables the creation of individual, local electrical signals, a prerequisite to implement mechanical based logic [41]. In addition, the optical setup reduces to a light source.

The remaining chapters present fundamental studies of the oscillatory mechanical response: in chapter 5, the nonlinear response of the nanobeam is investigated in greater detail. Subject to suitable actuation, a nonlinear oscillator displays bistability (see e.g. [42]); therefore its response is hysteretic, i.e., it depends on the history. In the bistable regime, the state of the resonator represent a simple memory element [43]. As part of this thesis a suitable switching scheme has been established based on additional excitation pulses that allows for the first time to switch directly and fast between the stable states. In addition this represents an investigation on the attractor characteristics of the stable states [44, 45].

Lastly, the damping properties of the investigated beams are analyzed (chapter 6). Apart from the mechanical robustness, prestressed silicon nitride resonators of moderate frequencies display unusual high mechanical quality factors, i.e. sharp resonances [46]. A quantitative analysis adapting Zener’s phenomenological model of damping [47] to pre-stressed system has been achieved, the measured quality factors could be quantitatively reproduced with a single fit-parameter. This analysis shows that the enhanced quality factors result from the increased stored energy of oscillating with applied stress. In particular, the damping characteristics of the material are not influenced by the pre-stress, in contrast to existing speculations [48].

References

- [1] J. Bardeen and W. H. Brattain, “The Transistor, A Semi-Conductor Triode” *Phys. Rev.* **74**, 230– (1948).
- [2] L. J. Yang, T. W. Huang, and P. Z. Chang, “CMOS microelectromechanical bandpass filters” *Sens. Actuators, A* **90**, 148 (2001).
- [3] J. F. Rhoads, S. W. Shaw, K. L. Turner, and R. Baskaran, “Tunable Microelectromechanical Filters that Exploit Parametric Resonance” *J. Vib. Acoust.* **127**, 423–430 (2005).
- [4] C. T. C. Nguyen, “MEMS technology for timing and frequency control” *IEEE T. Ultrason. Ferr.* **54**, 251–270 (2007).
- [5] J. E. Y. Lee and A. A. Seshia, “5.4-MHz single-crystal silicon wine glass mode disk resonator with quality factor of 2 million” *Sens. Actuators, A* **156**, 28–35 (2009).
- [6] K. Y. Yasumura, T. D. Stowe, E. M. Chow, T. Pfafman, T. W. Kenny, B. C. Stipe, and D. Rugar, “Quality factors in micron- and submicron-thick cantilevers” *J. Microelectromech. S.* **9**, 117–125 (2000).
- [7] T. D. Stowe, K. Yasumura, T. W. Kenny, D. Botkin, K. Wago, and D. Rugar, “Attonewton force detection using ultrathin silicon cantilevers” *Appl. Phys. Lett.* **71**, 288–290 (1997).
- [8] H. J. Mamin, M. Poggio, C. L. Degen, and D. Rugar, “Nuclear magnetic resonance imaging with 90-nm resolution” *Nat. Nanotechnol.* **2**, 301–306 (2007).
- [9] L. Lin, R. Howe, and A. Pisano, “Microelectromechanical filters for signal processing” *J. Microelectromech. S.* **7**, 286 (1998).
- [10] N. V. Lavrik, M. J. Sepaniak, and P. G. Datskos, “Cantilever transducers as a platform for chemical and biological sensors” *Rev. Sci. Instrum.* **75**, 2229–2253 (2004).
- [11] C. Ziegler, “Cantilever-based biosensors” *Anal. Bioanal. Chem.* **379**, 946 (2004).
- [12] C. L. Degen, M. Poggio, H. J. Mamin, C. T. Rettner, and D. Rugar, “Nanoscale magnetic resonance imaging” *P. Natl. Acad. Sci. USA* **106**, 1313–1317 (2009).

- [13] S. D. Bennett, L. Cockins, Y. Miyahara, P. Grütter, and A. A. Clerk, “Strong Electromechanical Coupling of an Atomic Force Microscope Cantilever to a Quantum Dot” *Phys. Rev. Lett.* **104**, 017 203 (2010).
- [14] B. C. Stipe, H. J. Mamin, T. D. Stowe, T. W. Kenny, and D. Rugar, “Non-contact Friction and Force Fluctuations between Closely Spaced Bodies” *Phys. Rev. Lett.* **87**, 096 801 (2001).
- [15] A. N. Cleland and M. L. Roukes, “Fabrication of high frequency nanometer scale mechanical resonators from bulk Si crystals” *Appl. Phys. Lett.* **69**, 2653–2655 (1996).
- [16] A. N. Cleland and M. L. Roukes, “A nanometre-scale mechanical electrometer” *Nature* **392**, 160 (1998).
- [17] Y. Yang, C. Callegari, X. Feng, K. Ekinici, and M. Roukes, “Zeptogram-Scale Nanomechanical Mass Sensing” *Nano Lett.* **6**, 583–586 (2006).
- [18] K. Jensen, K. Kim, and A. Zettl, “An atomic-resolution nanomechanical mass sensor” *Nat. Nanotechnol.* **3**, 533 (2008).
- [19] P. Rabl, P. Cappellaro, M. V. G. Dutt, L. Jiang, J. R. Maze, and M. D. Lukin, “Strong magnetic coupling between an electronic spin qubit and a mechanical resonator” *Phys. Rev. B* **79**, 041 302 (2009).
- [20] A. D. O’Connell, M. Hofheinz, M. Ansmann, R. C. Bialczak, M. Lenander, E. Lucero, M. Neeley, D. Sank, H. Wang, M. Weides, J. Wenner, J. M. Martinis, and A. N. Cleland, “Quantum ground state and single-phonon control of a mechanical resonator” *Nature* **464**, 697–703 (2010).
- [21] D. W. Carr, S. Evoy, L. Sekaric, H. G. Craighead, and J. M. Parpia, “Measurement of mechanical resonance and losses in nanometer scale silicon wires” *Appl. Phys. Lett.* **75**, 920–922 (1999).
- [22] J. L. Yang, T. Ono, and M. Esashi, “Energy dissipation in submicrometer thick single-crystal silicon cantilevers” *J. Microelectromech. S.* **11**, 775–783 (2002).
- [23] Q. P. Unterreithmeier, T. Faust, and J. P. Kotthaus, “Damping of Nanomechanical Resonators” *Phys. Rev. Lett.* **105**, 027 205 (2010).
- [24] X. L. Feng, R. He, P. Yang, and M. L. Roukes, “Very High Frequency Silicon Nanowire Electromechanical Resonators” *Nano Lett.* **7**, 1953–1959 (2007).
- [25] A. K. Huettel, G. A. Steele, B. Witkamp, M. Poot, L. P. Kouwenhoven, and H. S. J. van der Zant, “Carbon Nanotubes as Ultrahigh Quality Factor Mechanical Resonators” *Nano Lett.* **9**, 2547–2552 (2009).
- [26] G. A. Steele, A. K. Huttel, B. Witkamp, M. Poot, H. B. Meerwaldt, L. P. Kouwenhoven, and H. S. J. van der Zant, “Strong Coupling Between Single-Electron Tunneling and Nanomechanical Motion” *Science* **325**, 1103–1107 (2009).

-
- [27] D. Garcia-Sanchez, A. M. van der Zande, A. S. Paulo, B. Lassagne, P. L. McEuen, and A. Bachtold, “Imaging Mechanical Vibrations in Suspended Graphene Sheets” *Nano Lett.* **8**, 1399–1403 (2008).
- [28] J. JACKLE, “Ultrasonic Attenuation In Glasses At Low-temperatures” *Z. Phys.* **257**, 212–223 (1972).
- [29] S. Y. Kim and H. S. Park, “The Importance of Edge Effects on the Intrinsic Loss Mechanisms of Graphene Nanoresonators” *Nano Lett.* **9**, 969–974 (2009).
- [30] T. Faust, “Nanomechanik zugverspannter Siliziumnitridresonatoren” Diplomarbeit (2009).
- [31] L. Sekaric, J. M. Parpia, H. G. Craighead, T. Feygelson, B. H. Houston, and J. E. Butler, “Nanomechanical resonant structures in nanocrystalline diamond” *Appl. Phys. Lett.* **81**, 4455–4457 (2002).
- [32] T. Tachizaki, T. Muroya, O. Matsuda, Y. Sugawara, D. H. Hurley, and O. B. Wright, “Scanning ultrafast Sagnac interferometry for imaging two-dimensional surface wave propagation” *Rev. Sci. Instrum.* **77**, 043 713–12 (2006).
- [33] R. He, X. L. Feng, M. L. Roukes, and P. Yang, “Self-Transducing Silicon Nanowire Electromechanical Systems at Room Temperature” *Nano Lett.* **8**, 1756–1761 (2008).
- [34] H. Martinussen, A. Aksnes, and H. E. Engan, “Wide frequency range measurements of absolute phase and amplitude of vibrations in micro- and nanostructures by optical interferometry” *Opt. Express* **15**, 11 370–11 384 (2007).
- [35] Y. Hadjar, P. F. Cohadon, C. G. Aminoff, M. Pinard, and A. Heidmann, “High-sensitivity optical measurement of mechanical Brownian motion” *Europhys. Lett.* **47**, 545–551 (1999).
- [36] H. R. Bohm, S. Gigan, F. Blaser, A. Zeilinger, M. Aspelmeyer, G. Langer, D. Bauerle, J. B. Hertzberg, and K. C. Schwab, “High reflectivity high-Q micromechanical Bragg mirror” *Appl. Phys. Lett.* **89**, 223 101 (2006).
- [37] O. Arcizet, P.-F. Cohadon, T. Briant, M. Pinard, A. Heidmann, J.-M. Mackowski, C. Michel, L. Pinard, O. Francais, and L. Rousseau, “High-Sensitivity Optical Monitoring of a Micromechanical Resonator with a Quantum-Limited Optomechanical Sensor” *Phys. Rev. Lett.* **97**, 133 601 (2006).
- [38] J. D. Thompson, B. M. Zwickl, A. M. Jayich, F. Marquardt, S. M. Girvin, and J. G. E. Harris, “Strong dispersive coupling of a high-finesse cavity to a micromechanical membrane” *Nature* **452**, 72–75 (2008).
- [39] D. K. Armani, T. J. Kippenberg, S. M. Spillane, and K. J. Vahala, “Ultra-high-Q toroid microcavity on a chip” *Nature* **421**, 925–928 (2003).

- [40] N. O. Azak, M. Y. Shagam, D. M. Karabacak, K. L. Ekinici, D. H. Kim, and D. Y. Jang, “Nanomechanical displacement detection using fiber-optic interferometry” *Appl. Phys. Lett.* **91**, 093 112 (2007).
- [41] I. Mahboob and H. Yamaguchi, “Bit storage and bit flip operations in an electromechanical oscillator” *Nat. Nanotechnol.* **3**, 275 (2008).
- [42] A. H. Nayfeh and D. T. Mook, *Nonlinear Oscillations* (Wiley, New York, 1995).
- [43] R. L. Badzey, G. Zolfagharkhani, A. Gaidarzhy, and P. Mohanty, “A controllable nanomechanical memory element” *Appl. Phys. Lett.* **85**, 3587–3589 (2004).
- [44] J. S. Aldridge and A. N. Cleland, “Noise-Enabled Precision Measurements of a Duffing Nanomechanical Resonator” *Phys. Rev. Lett.* **94**, 156 403 (2005).
- [45] I. Kozinsky, H. W. C. Postma, O. Kogan, A. Husain, and M. L. Roukes, “Basins of Attraction of a Nonlinear Nanomechanical Resonator” *Phys. Rev. Lett.* **99**, 207 201 (2007).
- [46] S. S. Verbridge, J. M. Parpia, R. B. Reichenbach, L. M. Bellan, and H. G. Craighead, “High quality factor resonance at room temperature with nanostings under high tensile stress” *J. Appl. Phys.* **99**, 124 304 (2006).
- [47] C. Zener, “Internal Friction in Solids II. General Theory of Thermoelastic Internal Friction” *Phys. Rev.* **53**, 90–99 (1938).
- [48] D. R. Southworth, R. A. Barton, S. S. Verbridge, B. Ilic, A. D. Fefferman, H. G. Craighead, and J. M. Parpia, “Stress and Silicon Nitride: A Crack in the Universal Dissipation of Glasses” *Phys. Rev. Lett.* **102**, 225 503 (2009).

Chapter 1

Dielectric Transduction

The present chapter is based on the publication shown in chapter A, see pages 51 et seq.

A prerequisite to study the resonant oscillations of nanomechanical elements is the ability to actuate these. This can be provided by the thermal noise [1], yet for many purposes a coherently driven signal is necessary. There are many implementations in order to exert a force on a nanoresonator. Experiments incorporate capacitive [2, 3], magnetomotive [4], piezoactive [5], inertial [6] and local heating [7, 8] schemes. An ideal actuation mechanism has several desirable characteristics:

- simple setup, ideally no external components required
- local actuation scalable to resonator arrays
- high bandwidth, frequency-independent actuation efficiency
- no restriction on resonator material and geometry
- temperature-independence, no unnecessary heating of the sample
- access to higher harmonics

For example the widely used magnetomotive scheme requires the metallization of the sample [4] which is accompanied by a degradation in mechanical quality factor [9], requires large magnetic fields and cannot actuate higher harmonics.

Complementary to the above mentioned implementations, we introduce a modification of the capacitive scheme [2, 10, 11] in which the resonator forms one electrode of a capacitor and therefore has to be highly conductive. In our approach the capacitor is formed by two electrodes, the mechanical element is placed in its local, non-uniform electric field. As a result of its polarizability the resonator gets attracted towards larger fields. A typical experimental implementation is shown in Fig. 1.1(a,b). Related experiments using micromechanical resonators are described in [12].

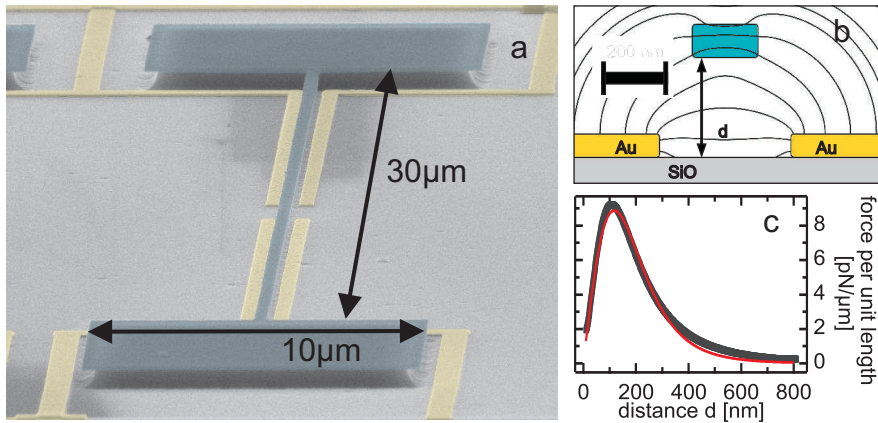


Figure 1.1: **SEM picture, cross section and force acting on a typical nanomechanical resonator.** **a** Scanning electron micrograph of a typical device. Shown in green is the silicon nitride forming resonator and its supports; the gold electrodes (yellow) are biased by DC and RF voltages. **b** Schematic cross-section, including the electric field lines provided by a finite elements simulation. **c** Simulated dielectric force vs. distance from the substrate d applying a voltage of 2V to the electrodes.

The applied electric field influences a dipolar moment in the resonator, here most prominently in-plane. The dipole in turn gets attracted towards larger fields which is towards the electrodes. As both effects are linear in the electric field, the force is proportional to the square of the applied voltage. To resonantly and efficiently actuate the beam, a combination of voltages is therefore chosen, a large DC voltage and a small RF voltage. Most conveniently, one can think of this as the DC field influencing the dipolar moment; the RF component exerting an oscillating force on the dipole.

Here, the applied detection scheme is based on optical interference [13] and shall be explained in greater detail in chapter 2 and 4. The performance of the actuation is shown in Fig. 1.2; in (a) the Brownian motion of the resonator is displayed; as its magnitude is predicted by theory [14] it offers a calibration to convert the measured signal into displacement. In (b) the oscillation amplitude of the actuated beam is shown vs. frequency; the response is precisely described by a Lorentzian lineshape, as expected for a harmonic oscillator. Part (c) is composed of several such frequency sweeps with different DC voltages, the measured signal power is color-coded. The resonance frequency can be seen to shift downwards with DC bias in a quadratic manner. This can be readily understood as the attractive dielectric force is strongly distance dependent, see Fig. 1.1(c). Applying a DC field, the resonator relaxes in a new equilibrium position, the resulting increase in strain and the accompanying frequency shift, see e.g. [15] is calculated in G.1.

The up-shift however is overcompensated by the following effect: for sufficiently

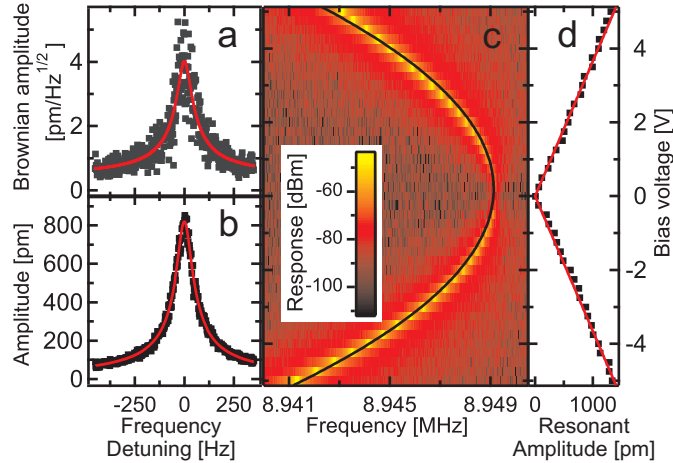


Figure 1.2: **Response of the mechanical beam.** **a** Measured Brownian motion (black) of the beam at room temperature. **b** Dielectrically excited oscillation applying $V_{\text{DC}} + V_{\text{RF}} = 1 \text{ V} \pm 0.2 \text{ mV}$; the data is fitted using a Lorentzian lineshape. **c** and **d** Response of the resonator as function of frequency and DC-bias; applying an $V_{\text{RF}} = \pm 0.06 \text{ mV}$; in **c** the power response is color-coded, one can see that the resonance frequency quadratically decreases with applied DC-voltage (fit as black line). The resonant amplitude is shown in **d**; the linear dependence on bias reflects the coupling to the dipolar moment provided by the DC-voltage.

small amplitudes the remaining part of the dielectric force is linear in displacement ($F = \partial_x F \delta x$). This modifies the intrinsic spring constant k_0 and therefore the resonance frequency f ; as the force is quadratic in applied voltage V_{DC} , it follows (with c being a constant, m effective resonator mass):

$$f = \frac{1}{2\pi} \sqrt{\frac{k}{m}} = \frac{1}{2\pi} \sqrt{\frac{k_0 - cV_{\text{DC}}^2}{m}} \approx \frac{1}{2\pi} f_0 \left(1 - \frac{cV_{\text{DC}}^2}{2k_0} \right) \quad (1.1)$$

Consequently, a quadratic detuning of the resonance frequency is anticipated, in accordance with the data, highlighted by the solid black line in (c). Lastly, part (d) shows the mechanical amplitude on resonance; its magnitude is directly proportional to the DC bias, as expected.

The detuning range can be as large as 200 kHz, corresponding to 2000 FWHM (full width at half max). The voltage-tunability also facilitates the actuation of parametric oscillation, see e.g. [16]. Even in the absence of an external force, modulating the resonance frequency can lead to the spontaneous build-up of an oscillation; this happens most efficiently if the modulation occurs at twice the resonance frequency [16]. In Fig 1.3(a) the mechanical response near such a parametric resonance is shown as a function of applied RF power and frequency. Please note that the oscillation is detected at half the actuation frequency.

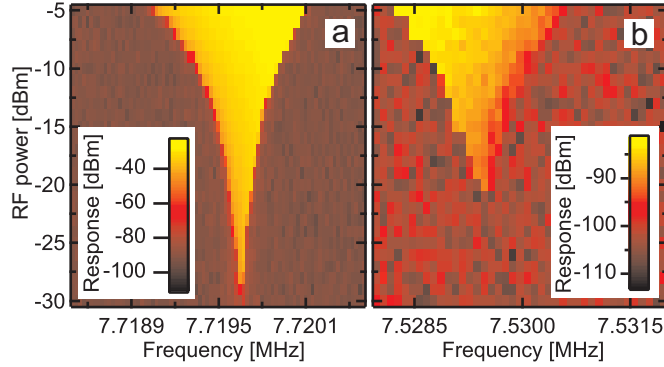


Figure 1.3: **Parametric Oscillation and Dielectric Detection** **a** Interferometrically measured power response subject to parametric actuation at twice the displayed frequency and $V_{\text{DC}} = 3 \text{ V}$. **c** The resonator is parametrically actuated using $V_{\text{DC}} = 20 \text{ V}$; the resulting response is dielectrically detected by biasing the underlying electrodes and measuring the their capacitance change with beam displacement.

Complementary to a driven harmonic resonance, the oscillation amplitude vanishes completely outside a specific parameter range leading to the tongue-like image. Within the tongue-like range it is limited by the onset of nonlinear effects [17].

We utilize the parametric resonance to separate actuation and detection frequency and thereby suppress resonant cross-talk. This facilitates the dielectric detection of the mechanical motion; in this detection scheme the oscillating resonator modulates the mutual capacitance of the gold electrodes, similar to previous implementations of the capacitive scheme [2, 18]. When biased, this leads to the generation of charge. We establish a preliminary setup in which the current is detected with a near-chip current-voltage converter. In Fig. 1.1(a) two pairs of gold electrodes can be seen; one pair serves to actuate the mechanical resonator; the second pair is biased and detects the oscillatory motion. Fig. 1.3(b) shows the same parametric resonance, measured dielectrically. Comparing the signal strength and noise background, one can estimate a sensitivity of approximately $20 \text{ pm}/\sqrt{\text{Hz}}$.

This sensitivity could be readily improved using the same techniques as in capacitive detection schemes by either resonantly enhancing the created charge [2] or converting the change in capacitance into a frequency modulation of an LC circuit [18, 19] (see also section G.2.2). Therefore, a complete transduction based on electrical signals is possible that merely requires two nearby metal gates to the mechanical resonator.

References

- [1] Y. Hadjar, P. F. Cohadon, C. G. Aminoff, M. Pinard, and A. Heidmann, “High-sensitivity optical measurement of mechanical Brownian motion” *Europhys. Lett.* **47**, 545–551 (1999).
- [2] P. A. Truitt, J. B. Hertzberg, C. C. Huang, K. L. Ekinici, and K. C. Schwab, “Efficient and Sensitive Capacitive Readout of Nanomechanical Resonator Arrays” *Nano Lett.* **7**, 120–126 (2007).
- [3] R. G. Knobel and A. N. Cleland, “Nanometre-scale displacement sensing using a single electron transistor” *Nature* **424**, 291–293 (2003).
- [4] A. N. Cleland and M. L. Roukes, “Fabrication of high frequency nanometer scale mechanical resonators from bulk Si crystals” *Appl. Phys. Lett.* **69**, 2653–2655 (1996).
- [5] S. C. Masmanidis, R. B. Karabalin, I. De Vlaminck, G. Borghs, M. R. Freeman, and M. L. Roukes, “Multifunctional Nanomechanical Systems via Tunably Coupled Piezoelectric Actuation” *Science* **317**, 780–783 (2007).
- [6] S. S. Verbridge, J. M. Parpia, R. B. Reichenbach, L. M. Bellan, and H. G. Craighead, “High quality factor resonance at room temperature with nanostings under high tensile stress” *J. Appl. Phys.* **99**, 124 304 (2006).
- [7] S. S. Verbridge, L. M. Bellan, J. M. Parpia, and H. G. Craighead, “Optically Driven Resonance of Nanoscale Flexural Oscillators in Liquid” *Nano Lett.* **6**, 2109–2114 (2006).
- [8] I. Bargatin, I. Kozinsky, and M. L. Roukes, “Efficient electrothermal actuation of multiple modes of high-frequency nanoelectromechanical resonators” *Appl. Phys. Lett.* **90**, 093 116 (2007).
- [9] L. Sekaric, J. M. Parpia, H. G. Craighead, T. Feygelson, B. H. Houston, and J. E. Butler, “Nanomechanical resonant structures in nanocrystalline diamond” *Appl. Phys. Lett.* **81**, 4455–4457 (2002).
- [10] D. Rugar and P. Grütter, “Mechanical parametric amplification and thermo-mechanical noise squeezing” *Phys. Rev. Lett.* **67**, 699–702 (1991).

- [11] J. F. Rhoads, S. W. Shaw, K. L. Turner, and R. Baskaran, “Tunable Microelectromechanical Filters that Exploit Parametric Resonance” *J. Vib. Acoust.* **127**, 423–430 (2005).
- [12] S. Schmid, M. Wendlandt, D. Junker, and C. Hierold, “Nonconductive polymer microresonators actuated by the Kelvin polarization force” *Appl. Phys. Lett.* **89**, 163 506 (2006).
- [13] N. O. Azak, M. Y. Shagam, D. M. Karabacak, K. L. Ekinici, D. H. Kim, and D. Y. Jang, “Nanomechanical displacement detection using fiber-optic interferometry” *Appl. Phys. Lett.* **91**, 093 112 (2007).
- [14] D. T. Gillespie, “The mathematics of Brownian motion and Johnson noise” *Am. J. Phys.* **64**, 225–240 (1996).
- [15] W. Y. Fung, E. N. Dattoli, and W. Lu, “Radio frequency nanowire resonators and in situ frequency tuning” *Appl. Phys. Lett.* **94**, 203 104 (2009).
- [16] K. L. Turner, S. A. Miller, P. G. Hartwell, N. C. MacDonald, S. H. Strogatz, and S. G. Adams, “Five parametric resonances in a microelectromechanical system” *Nature* **396**, 149 (1998).
- [17] A. H. Nayfeh and D. T. Mook, *Nonlinear Oscillations* (Wiley, New York, 1995).
- [18] K. R. Brown, J. Britton, R. J. Epstein, J. Chiaverini, D. Leibfried, and D. J. Wineland, “Passive Cooling of a Micromechanical Oscillator with a Resonant Electric Circuit” *Phys. Rev. Lett.* **99**, 137 205 (2007).
- [19] C. A. Regal, J. D. Teufel, and K. W. Lehnert, “Measuring nanomechanical motion with a microwave cavity interferometer” *Nat. Phys.* **4**, 555 (2008).

Chapter 2

Stroboscopic Downconversion

The present chapter is based on the publication shown in chapter B, see pages 55 et seq.

Various optical detection schemes have been established to detect [1–9] or actuate [8, 10, 11] nanomechanical motion. In the detection schemes scattering and interference lead to intensity modulations with beam displacement. We utilize a basic version of such a scheme [1, 6]: the bare end of a cleaved fibre is closely positioned above the mechanical resonator. The beam and its surroundings are illuminated; the reflected light partly couples back into the fibre; its intensity is measured using a photodetector.

In general, to detect the resulting high frequency signals requires either a fast measurement setup or suitable downconversion [3, 12–16]. These implementations utilize two different strategies: the first measures the envelope of the oscillation [14–16] rather than performing a linear position measurement. To increase sensitivity, the actuation strength is modulated and thereby the magnitude of the envelope oscillates. The second introduces an additional pre-modulation of the later detected signal [3, 12, 13]. Therefore the product of both modulations (pre- and probe) is generated; it includes sum and difference frequencies. A suitable choice of pre-modulation frequency allows the latter to be a low-frequency signal; the former will be neglected.

We adapt the concept previously employed in electrical setups [12, 13] and in optical large-scale setups [17] to our optical scheme; the illumination is modulated by switching on and off the light source. The signal path now is as follows, see Fig 2.1: an electrical signal of frequency f_{LO} is converted to $f_{RF} - f_{LO}$ using a second frequency f_{RF} and actuates the mechanical resonator (the mechanism has been explained in the previous chapter 1). The second signal is converted into an intensity modulation at f_{RF} , the resulting beat in light intensity (at f_{LO}) is measured.

The setup significantly surpasses the bandwidth of the employed photodetector (PDA55, 10 MHz); it is sensitive to the phase of the mechanical oscillation. In Fig. 2.2(a,d) the mechanical response vs. applied actuation frequency is shown. The

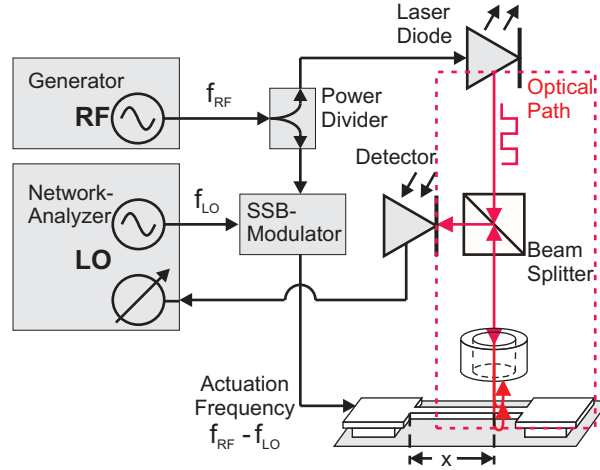


Figure 2.1: **Schematic transduction setup** the nanomechanical resonator is mounted in vacuum below the bare end of a cleaved glass fiber. The electronic path provides dielectric actuation at $f_{\text{RF}} - f_{\text{LO}}$ and an illumination intensity modulated at f_{RF} , creating a coherent signal at f_{LO} .

increased bandwidth enables us to record several mechanical harmonics, yielding more information of the system, e.g. enables the determination of mass and position of attached particles [18].

In order to identify the measured resonances, we scan along the nano strings and record the phase of the oscillation; whenever an oscillation node is crossed one expects the phase to jump by π , in accordance with the data, see Fig. 2.2(b). Please note that although there is no focusing objective in our setup; the spatial resolution can be estimated to be around $1\mu\text{m}$, this is a result of the fact that backscattered light that is not in the center of the optical beam does not couple back into the glass fibre. Fig.2.2(b) displays frequency and quality factor of the obtained resonances versus mode index (i.e. the number of antinodes). The quality factor will be treated in greater detail in chapter 6; here we focus on the frequency. One can deduce from the linear dependence on mode index that the mechanical resonator can be accurately treated as an oscillating string under tensile stress (as opposed to a stiff beam).

We utilize the model to extract the elastic parameters of the beam; method and results represents a novelty in the field of nanomechanics. The restoring force of the oscillatory mode can easily be calculated as shown in the appendix G.3 (see also [19]). The utilized parameters and their measured or extracted values are listed in table 2.1.

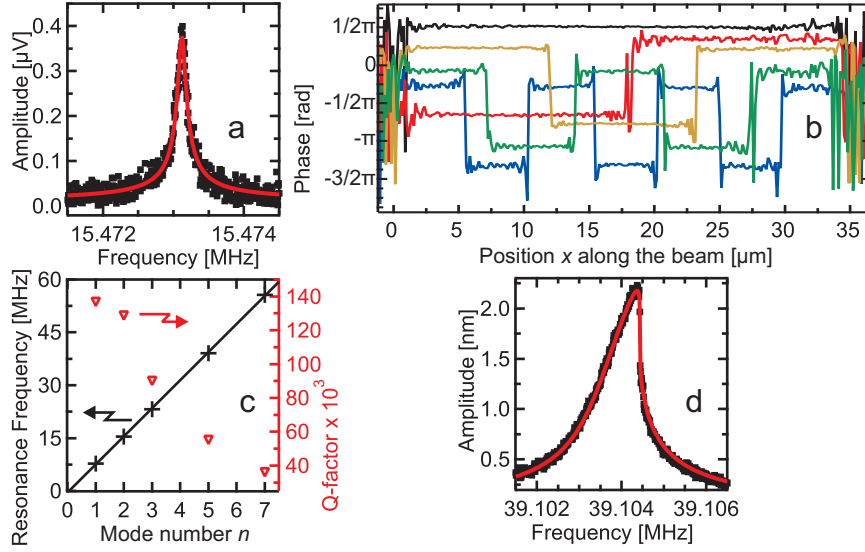


Figure 2.2: **Stroboscopically measured Response** **a** Lorentzian resonance of a nanomechanical resonator of dimensions $35 \cdot 0.2 \cdot 0.1 \mu\text{m}^3$, length, width, height, respectively, actuated at the second harmonic. **b** Spatial distribution of the measured phase of the observed modes scanning along the beam. **c** Resonance frequency and quality factor of the resonances; the frequencies display a string-like linear dependence on mode index. **d** Nonlinear response and fit of the resonator strongly actuated at its 5th harmonic; the fit enables the conversion to displacement amplitudes and the determination of Young's Modulus.

$$\frac{F[a]}{m_{\text{eff}}} = \underbrace{\frac{\pi^2 \sigma_0}{\rho l^2}}_{\equiv (2\pi f_0)^2} a + \underbrace{\frac{\pi^4 E}{4\rho l^4}}_{\equiv \alpha_3} a^3 \quad (2.1)$$

For sufficiently small oscillation amplitudes a as in Fig 2.2(a), the measurement of the resonance frequency thereby yields the pre-stress σ_0 . With increasing amplitude, nonlinear effects become noticeable, the lineshape bends over to higher frequencies [20, 21] as seen in Fig. 2.2(d). The nonlinear response shall be treated in greater detail in chapter 5 and G.5.

To obtain the cubic correction α_3 and thereby E , first the Brownian motion of the fundamental mode is measured, see chapter 1. Thereby the measured signal can be calibrated into displacement. Then the beam is strongly actuated, its nonlinear response is measured and fitted with a solution of the nonlinear (so-called Duffing) equation. We thereby obtain α_3 for the fundamental mode and are able to calculate Young's modulus.

The nonlinear contribution α_3 can now be calculated for higher harmonics as well from eq. 2.1, $\alpha_3 \propto l_n^{-4}$. Here, l_n is the length of the resonator divided by the mode

designation	symbol	value
density [22]	ρ	$2.8 \cdot 10^3 \text{ kg/m}^3$
length	l	$35 \text{ }\mu\text{m}$
resonance frequency	f_0	7.71 MHz
prestress	σ_0	850 MPa
cubic part of the restoring force (fundamental mode)	α_3	$8.1 \cdot 10^{26} \text{ m}^{-2}\text{s}^{-2}$
Young's Modulus	E	165 GPa

Table 2.1: **Geometric and elastic Parameters of the Employed Nanoresonator**

index l/n , i.e. the distance between adjacent antinodes. The nonlinear response of higher harmonics is now fitted and rescaled to match the calculated α_3 , as shown in Fig. 2.2(d). We thereby achieve a displacement calibration, although the Brownian motion of the higher harmonics can not be resolved.

Related experiments have been reported in Ref. [23], yet the material parameters could not be retrieved and therefore quantitative exact amplitude could be calculated.

References

- [1] D. W. Carr, L. Sekaric, and H. G. Craighead, “Measurement of nanomechanical resonant structures in single-crystal silicon” *J. Vac. Sci. Technol. B* **16**, 3821–3824 (1998).
- [2] T. Thundat, E. Finot, Z. Hu, R. H. Ritchie, G. Wu, and A. Majumdar, “Chemical sensing in Fourier space” *Appl. Phys. Lett.* **77**, 4061–4063 (2000).
- [3] I. Bargatin, E. B. Myers, J. Arlett, B. Gudlewski, and M. L. Roukes, “Sensitive detection of nanomechanical motion using piezoresistive signal downmixing” *Appl. Phys. Lett.* **86**, 133 109 (2005).
- [4] H. R. Bohm, S. Gigan, F. Blaser, A. Zeilinger, M. Aspelmeyer, G. Langer, D. Bauerle, J. B. Hertzberg, and K. C. Schwab, “High reflectivity high-Q micromechanical Bragg mirror” *Appl. Phys. Lett.* **89**, 223 101 (2006).
- [5] D. Karabacak, T. Kouh, C. C. Huang, and K. L. Ekinci, “Optical knife-edge technique for nanomechanical displacement detection” *Appl. Phys. Lett.* **88**, 193 122 (2006).
- [6] N. O. Azak, M. Y. Shagam, D. M. Karabacak, K. L. Ekinci, D. H. Kim, and D. Y. Jang, “Nanomechanical displacement detection using fiber-optic interferometry” *Appl. Phys. Lett.* **91**, 093 112 (2007).
- [7] I. Favero, S. Stapfner, D. Hunger, P. Paulitschke, J. Reichel, H. Lorenz, E. M. Weig, and K. Karrai, “Fluctuating nanomechanical system in a high finesse optical microcavity” *Opt. Express* **17**, 12 813–12 820 (2009).
- [8] G. Anetsberger, O. Arcizet, Q. P. Unterreithmeier, R. Riviere, A. Schliesser, E. M. Weig, J. P. Kotthaus, and T. J. Kippenberg, “Near-field cavity optomechanics with nanomechanical oscillators” *Nat. Phys.* **5**, 909–914 (2009).
- [9] M. Eichenfield, R. Camacho, J. Chan, K. J. Vahala, and O. Painter, “A picogram- and nanometre-scale photonic-crystal optomechanical cavity” *Nature* **459**, 550–556 (2009).
- [10] B. Ilic, S. Krylov, K. Aubin, R. Reichenbach, and H. G. Craighead, “Optical excitation of nanoelectromechanical oscillators” *Appl. Phys. Lett.* **86**, 193 114 (2005).

- [11] S. S. Verbridge, L. M. Bellan, J. M. Parpia, and H. G. Craighead, “Optically Driven Resonance of Nanoscale Flexural Oscillators in Liquid” *Nano Lett.* **6**, 2109–2114 (2006).
- [12] I. Kozinsky, H. W. C. Postma, O. Kogan, A. Husain, and M. L. Roukes, “Basins of Attraction of a Nonlinear Nanomechanical Resonator” *Phys. Rev. Lett.* **99**, 207 201 (2007).
- [13] R. He, X. L. Feng, M. L. Roukes, and P. Yang, “Self-Transducing Silicon Nanowire Electromechanical Systems at Room Temperature” *Nano Lett.* **8**, 1756–1761 (2008).
- [14] A. S. Paulo, J. P. Black, R. M. White, and J. Bokor, “Detection of nanomechanical vibrations by dynamic force microscopy in higher cantilever eigenmodes” *Appl. Phys. Lett.* **91**, 053 116 (2007).
- [15] D. Garcia-Sanchez, A. San Paulo, M. J. Esplandiu, F. Perez-Murano, L. Forró, A. Aguasca, and A. Bachtold, “Mechanical Detection of Carbon Nanotube Resonator Vibrations” *Phys. Rev. Lett.* **99**, 085 501 (2007).
- [16] D. Garcia-Sanchez, A. M. van der Zande, A. S. Paulo, B. Lassagne, P. L. McEuen, and A. Bachtold, “Imaging Mechanical Vibrations in Suspended Graphene Sheets” *Nano Lett.* **8**, 1399–1403 (2008).
- [17] H. Martinussen, A. Aksnes, and H. E. Engan, “Wide frequency range measurements of absolute phase and amplitude of vibrations in micro- and nanostructures by optical interferometry” *Opt. Express* **15**, 11 370–11 384 (2007).
- [18] S. Dohn, W. Svendsen, A. Boisen, and O. Hansen, “Mass and position determination of attached particles on cantilever based mass sensors” *Rev. Sci. Instrum.* **78**, 103 303 (2007).
- [19] W. Weaver, S. P. Timoshenko, and D. H. Young, *Vibration Problems in Engineering* (Wiley, New York, 1990).
- [20] A. H. Nayfeh and D. T. Mook, *Nonlinear Oscillations* (Wiley, New York, 1995).
- [21] B. Yurke, D. S. Greywall, A. N. Pargellis, and P. A. Busch, “Theory of amplifier-noise evasion in an oscillator employing a nonlinear resonator” *Phys. Rev. A* **51**, 4211–4229 (1995).
- [22] M. G. el Hak, *The MEMS Handbook* (CRC Press, 2001).
- [23] D. W. Carr, S. Evoy, L. Sekaric, H. G. Craighead, and J. M. Parpia, “Measurement of mechanical resonance and losses in nanometer scale silicon wires” *Appl. Phys. Lett.* **75**, 920–922 (1999).

Chapter 3

Near-field cavity optomechanics

The present chapter is based on the publication shown in chapter C, see pages 59 et seq.

Coupling optical and mechanical degrees of freedom has become a prospering field in science since the experimental realization of cooling a cantilever's thermal motion using an intrinsically passive method [1]. In these experiments, mechanical displacement detunes an optical [2–4] or LC [5, 6] resonance. The resulting phase shift of the electromagnetic wave with displacement allows the sensitive detection of motion [2–4, 6], at the same time the field exerts force on the mechanical element. As this force does not react instantaneously to a change in position because of the finite lifetime of the stored photons, force and position are out of phase. This phase lag can lead to either cooling or heating of the mechanical degree of freedom. The ultimate reduction in displacement noise would reveal the quantum nature of the system. This could illuminate the transfer of photon shot-noise to the mechanical oscillation [7, 8] and might help to understand the process of decoherence [8, 9].

Recently, the mechanical ground state has been reached using a very different setup [10]. Instead of parametrically coupling the motion to a resonance and thereby allowing a linear position measurement, the mechanical oscillation is resonantly coupled to a phase qubit. Because of its strong nonlinear dependence on photon number [11] it allows the preparation of states of discrete energy quanta [10, 11] (Fock-states). Tuning the qubit in resonance with the mechanical element, the excitation oscillates between both systems. The mechanical degree of freedom is realized as bulk oscillations of a piezoelectric resonator. In this configuration a change in size of the resonator leaves the essential characteristics unchanged, as the effect of smaller zero-point displacement with increasing size is compensated by increased electro-mechanical interaction. The cooling in this experiment is provided by standard cryogenic techniques.

In a more typical setup a small resonator has advantageous properties; it enables at the same time high resonance frequencies and low effective masses. This leads to a large energy spacing that mitigates the temperature requirements and large

zero-point motion facilitating the detection of displacement [12, 13].

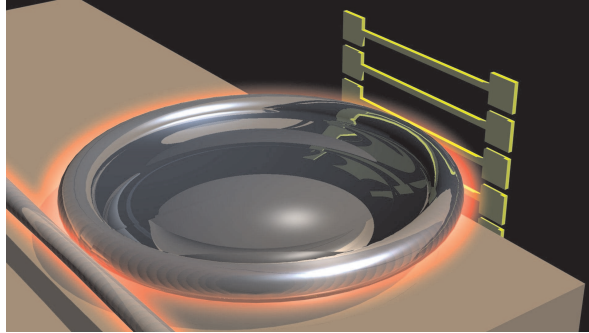


Figure 3.1: **Evanescent coupling to a microtoroid** Schematic image of setup, showing a tapered fibre, its traveling mode is coupled to the optical whispering gallery mode of a microresonator. The nanomechanical beams are dispersively coupled to the evanescent light field of the toroid.

However, previous optical setups relying on free-space beams [4, 14, 15] do not allow a reduction in size of the mechanical element below the wavelength of the light as the increasing scattering rate decreases the finesse of the optical cavity. To overcome this limitation, a micro-toroid with a high finesse is used, see Fig. 3.1; the light is guided along the circumference of the ring because of total internal reflection, referred to as whispering-gallery mode. The optical mode couples to the evanescent light field of a nearby tapered glass-fibre [16]. As the coupling is adiabatic, i.e. changes in the effective index of refraction occur slowly on length scales of the wavelength it introduces negligible scattering.

This coupling mechanism is now utilized once again as the whispering-gallery mode also has an evanescent tail extending into the vacuum. A nanomechanical resonator is placed in close proximity to the toroid; its (optical) dielectric constant leads to a local change in effective refractive index of the optical mode. Consequently the optical resonance frequency shifts, this is shown in fig. 3.2 versus the (static) distance of the mechanical resonator. The coupling rate can be seen to decrease exponentially with the distance reflecting the field intensity distribution. At the same time the finesse of the optical mode does not degrade as can be inferred from the unaffected linewidth demonstrating that the optomechanical interaction is dispersive.

To sensitively detect the displacement of the nanomechanical beam, a laser is locked to the cavity resonance, using an optical phase shift technique [2, 17]. The transmission through the optical fibre equally gets phase shifted with mechanical oscillation; the resulting intensity modulation is detected. This setup has been shown to allow near-quantum limited sensitivity [2]; its imprecision is (nearly) limited by photon shot noise. Figure 3.3 shows the displacement spectrum of a nanomechanical resonator, exhibiting a dynamic range of 60 dB. Remarkably, the imprecision of the

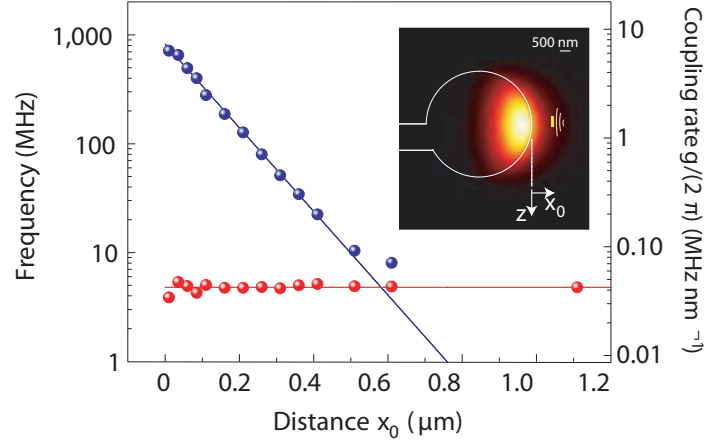


Figure 3.2: **Measured coupling rate and linewidth** The optomechanical coupling rate (blue) is displayed vs. toroid-resonator separation (see inset); its exponential dependence reflects the intensity profile of the evanescent optical field. The optical linewidth (i.e. the finesse of the cavity) can be seen not to degrade even at the smallest distances.

measurement is below the standard quantum limit (SQL) which is the minimum achievable detection sensitivity. Please note that the imprecision can be lower than the sensitivity, as the detection necessarily impinges noise on the resonator. In addition, the mechanical resonance frequency is larger than the photon loss rate; the setup is in the so-called resolved sideband regime, a prerequisite to allow cavity assisted ground state cooling [12, 13].

Although higher optical sensitivities had been reported earlier [2, 18], this was the first to fall below the SQL. After submission a measurement implementing a microwave-setup demonstrated a measurement imprecision at the SQL [19]. In the summary (pages 47 et seq.) a further improvement of the setup is briefly discussed.

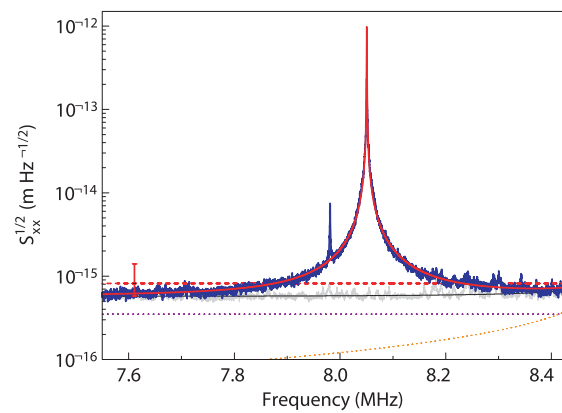


Figure 3.3: **Displacement Measurement** Room temperature Brownian motion of the fundamental mode of a nanomechanical string with dimensions $110 \text{ nm} \cdot 800 \text{ nm} \cdot 35 \mu\text{m}$. The measurement imprecision at an optical input power of $65 \mu\text{W}$ is $570 \text{ am Hz}^{1/2}$ (grey line), below the standard quantum limit of $820 \text{ am Hz}^{1/2}$ (red dashed line). The background noise is laser shot noise (40%, purple), thermorefractive noise (orange) and detector noise.

References

- [1] C. H. Metzger and K. Karrai, “Cavity cooling of a microlever” *Nature* **432**, 1002 (2004).
- [2] O. Arcizet, P.-F. Cohadon, T. Briant, M. Pinard, A. Heidmann, J.-M. Mackowski, C. Michel, L. Pinard, O. Francais, and L. Rousseau, “High-Sensitivity Optical Monitoring of a Micromechanical Resonator with a Quantum-Limited Optomechanical Sensor” *Phys. Rev. Lett.* **97**, 133 601 (2006).
- [3] A. Schliesser, R. Riviere, G. Anetsberger, O. Arcizet, and T. J. Kippenberg, “Resolved-sideband cooling of a micromechanical oscillator” *Nat. Phys.* **4**, 415–419 (2008).
- [4] J. D. Thompson, B. M. Zwickl, A. M. Jayich, F. Marquardt, S. M. Girvin, and J. G. E. Harris, “Strong dispersive coupling of a high-finesse cavity to a micromechanical membrane” *Nature* **452**, 72–75 (2008).
- [5] K. R. Brown, J. Britton, R. J. Epstein, J. Chiaverini, D. Leibfried, and D. J. Wineland, “Passive Cooling of a Micromechanical Oscillator with a Resonant Electric Circuit” *Phys. Rev. Lett.* **99**, 137 205 (2007).
- [6] C. A. Regal, J. D. Teufel, and K. W. Lehnert, “Measuring nanomechanical motion with a microwave cavity interferometer” *Nat. Phys.* **4**, 555 (2008).
- [7] P. Verlot, A. Tavernarakis, T. Briant, P.-F. Cohadon, and A. Heidmann, “Scheme to Probe Optomechanical Correlations between Two Optical Beams Down to the Quantum Level” *Phys. Rev. Lett.* **102**, 103 601– (2009).
- [8] F. Marquardt and S. Girvin, “Optomechanics” *Phys.* **2**, 40 (2009).
- [9] S. Bose, K. Jacobs, and P. L. Knight, “Scheme to probe the decoherence of a macroscopic object” *Phys. Rev. A* **59**, 3204– (1999).
- [10] A. D. O’Connell, M. Hofheinz, M. Ansmann, R. C. Bialczak, M. Lenander, E. Lucero, M. Neeley, D. Sank, H. Wang, M. Weides, J. Wenner, J. M. Martinis, and A. N. Cleland, “Quantum ground state and single-phonon control of a mechanical resonator” *Nature* **464**, 697–703 (2010).
- [11] M. Hofheinz, E. M. Weig, M. Ansmann, R. C. Bialczak, E. Lucero, M. Neeley, A. D. O’Connell, H. Wang, J. M. Martinis, and A. N. Cleland, “Generation of Fock states in a superconducting quantum circuit” *Nature* **454**, 310–314 (2008).

- [12] F. Marquardt, J. P. Chen, A. A. Clerk, and S. M. Girvin, “Quantum Theory of Cavity-Assisted Sideband Cooling of Mechanical Motion” *Phys. Rev. Lett.* **99**, 093 902 (2007).
- [13] I. Wilson-Rae, N. Nooshi, W. Zwerger, and T. J. Kippenberg, “Theory of Ground State Cooling of a Mechanical Oscillator Using Dynamical Backaction” *Phys. Rev. Lett.* **99**, 093 901– (2007).
- [14] S. Gigan, H. R. Bohm, M. Paternostro, F. Blaser, G. Langer, J. B. Hertzberg, K. C. Schwab, D. Bauerle, M. Aspelmeyer, and A. Zeilinger, “Self-cooling of a micromirror by radiation pressure” *Nature* **444**, 67–70 (2006).
- [15] I. Favero, S. Stapfner, D. Hunger, P. Paulitschke, J. Reichel, H. Lorenz, E. M. Weig, and K. Karrai, “Fluctuating nanomechanical system in a high finesse optical microcavity” *Opt. Express* **17**, 12 813–12 820 (2009).
- [16] D. K. Armani, T. J. Kippenberg, S. M. Spillane, and K. J. Vahala, “Ultra-high-Q toroid microcavity on a chip” *Nature* **421**, 925–928 (2003).
- [17] R. W. P. DREVER, J. L. HALL, F. V. KOWALSKI, J. HOUGH, G. M. FORD, A. J. MUNLEY, and H. WARD, “Laser Phase And Frequency Stabilization Using An Optical-Resonator” *Appl. Phys. B - Photo.* **31**, 97–105 (1983).
- [18] M. Eichenfield, R. Camacho, J. Chan, K. J. Vahala, and O. Painter, “A picogram- and nanometre-scale photonic-crystal optomechanical cavity” *Nature* **459**, 550–556 (2009).
- [19] J. D. Teufel, T. Donner, M. A. Castellanos-Beltran, J. W. Harlow, and K. W. Lehnert, “Nanomechanical motion measured with an imprecision below that at the standard quantum limit” *Nat. Nanotechnol.* **4**, 820–823 (2009).

Chapter 4

On-chip Interferometric Detection

The present chapter is based on the publication shown in chapter D, see pages 65 et seq.

Complementary to the setup of the previous chapter, optimized to yield a very high displacement sensitivity, here a method is presented that provides a very integrable transduction. It can be seen as a modification of the optical detection setup introduced in chapter 2. Existing detection schemes either rely completely on optical [1–9] or electrical [10–16] signals. Whereas optical schemes offer the advantage of being material independent and can easily be designed not to introduce damping [17] they require external optical components. In particular in all these schemes the optical signal is measured off-chip, making these schemes less integrable, although research is pushing into on-chip optical signal processing [18–20].

Demonstrated electrical schemes however require the (partial) conductance of the resonator and often introduce damping that is inherently connected to the generation of the electrical signal [10, 12].

We present a detection scheme that relies on an optical interference effect, yet the intensity modulation is detected in the direct vicinity of the resonator, providing on-chip electrical signals. Figure 4.1 shows the detection principle: as in chapter 2 the mechanical resonator and its surroundings are illuminated. The light gets partly reflected forming a standing wave; the exact intensity profile will strongly depend on geometry. In particular a displacement of the beam will result in changes of the light pattern. We locally detect this modulation by placing two gold electrodes in the direct vicinity of the beam that are in contact with the silicon substrate. Thereby a Schottky-contact forms, see e.g. [21]; the light intensity leads to a photocurrent that is amplified and its modulation is detected.

Figure 4.2 displays the characteristics of the setup. In (a) the DC-response of the Schottky-contact is shown for different light intensities, it clearly displays the expected diode-like IV-curve.

Subject to (dielectrical, see chapter 1) actuation; a strong modulation of the photocurrent is recorded, see Fig. 4.2(b). It is composed of two contributions, a

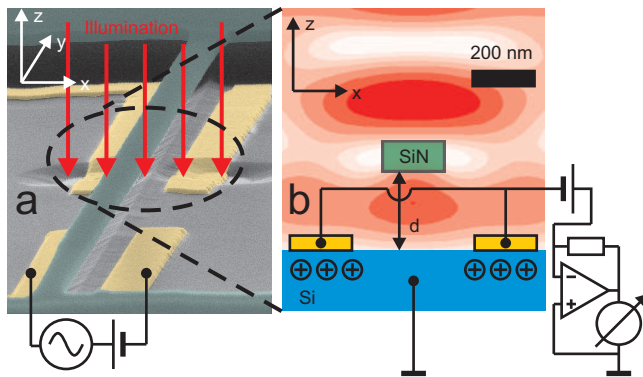


Figure 4.1: **Setup and Detection Principle** **a** SEM picture (false color) of the sample; two pairs of electrodes (yellow) provide actuation (lower pair) and detection. The latter are partly in direct contact to the underlying silicon as seen in the encircled area. **b** Cross-section; the contact leads to the formation of a Schottky-contact; the intensity modulation of the optical near-field pattern with beam displacement leads to a modulated photocurrent.

frequency-independent electric cross-talk and a sharp Lorentzian resonance corresponding to the mechanical displacement. The data can be accurately fitted using the sum of the two effects.

To convert the photocurrent into displacement, we successfully detect the Brownian motion of the resonator, see Fig. 4.2(c). We thereby obtain a calibration, as theory predicts the magnitude [22]. It also enables the determination of the setup sensitivity; as a bandwidth of 50 Hz was chosen, we conservatively estimate it to be $1 \text{ pm/Hz}^{1/2}$.

We further check the linearity of our setup by exciting the resonator to large amplitudes as shown in Fig. 4.2(d). The quadrature components of the signal are parametrically plotted versus applied frequency. The measured data points are found to be aligned on a circle until a sudden jumps to lower amplitudes occurs, as expected for a Duffing oscillator [23]. Any deviation from linear transduction would have lead to distortions from the observed behavior, we therefore conclude that the scheme remains linear up to amplitudes of $\pm 45 \text{ nm}$.

To demonstrate the applicability of our detection scheme, we implement a self-oscillator that is the detected signal is amplified and fed back to actuate the resonator. The signal path therefore forms a closed loop; in order to sustain an oscillation, the signal has to accumulate $2\pi \cdot k$, (k : integer) phase during one round-trip and the gain has to be greater or equal 1, see e.g. [24, 25]. As broad-band cross-talk likely enables such a resonance condition as well, one has to sufficiently suppress its magnitude. Here, this is accomplished by introducing a reference line in parallel to the sample; it is designed to produce a similar output as the cross-talk yet shifted

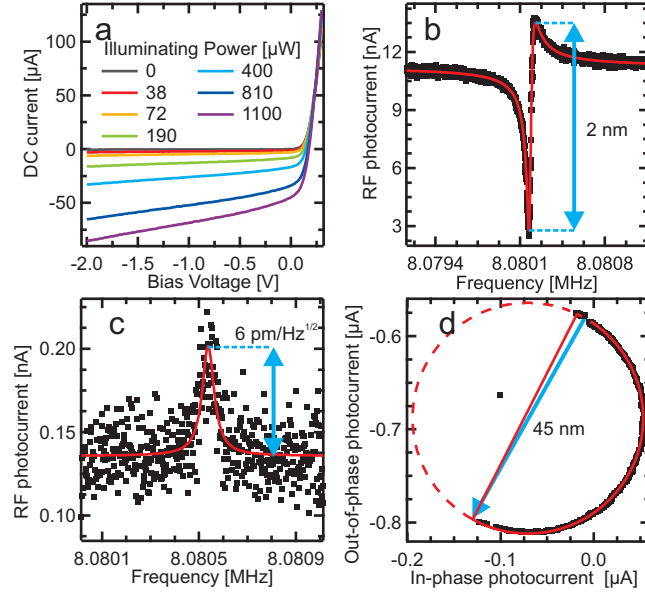


Figure 4.2: DC and resonant characteristics of the Schottky Detection a Subject to different illumination intensities, the photocurrent is measured vs. applied bias. **b** The RF-photocurrent is displayed when resonantly actuating the resonator; the data (black) can be accurately fitted using the sum of a mechanical Lorentzian and a flat cross-talk. **c** The Brownian Motion of the resonator leads to an RF-photocurrent in the absence of actuation; it allows the quantitative conversion of signal into displacement. **d** The quadrature components of the signal are displayed, the resonator is actuated well in the nonlinear regime; the response lies on the segment of a circle, confirming the linearity of the detection scheme up to amplitudes of 45 nm.

by π over the relevant frequency range. The sum of the signals will cancel except for the mechanically induced signal; frequency components that are far off-resonant are suppressed by a bandpass filter.

It is noteworthy that the use of a downconversion technique as in chapter 2 also evades such crosstalk, yet it requires an external frequency source.

Figure 4.3(a) shows the obtained frequency spectrum: a sharp spike that peaks out of a nearly flat background. In (b) we plot the single-sided spectrum versus frequency offset. This is often referred to as phase noise [24], and ultimately limited by the Brownian motion of the resonator, as shown in the figure. We have therefore successfully implemented a nanomechanical oscillator [26], able to operate at room temperature, that solely requires a light source as external component.

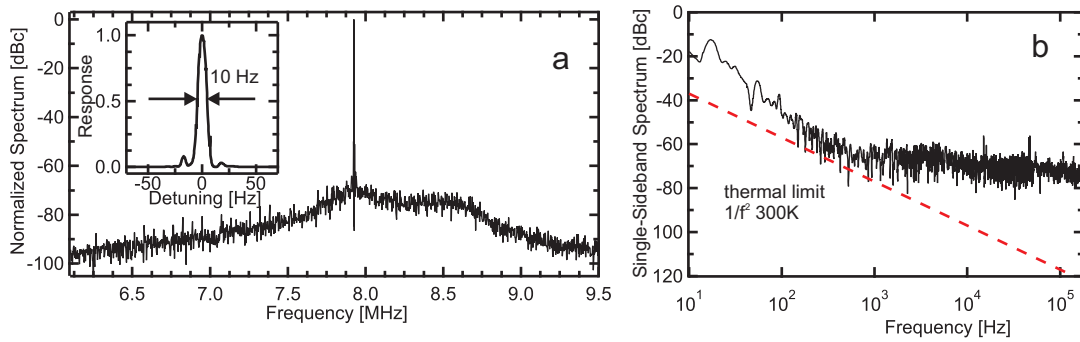


Figure 4.3: **Nanomechanical Oscillator** We suitably feed back the detected signal to the actuation electrodes and obtain self-oscillation, applying an optical power of 1 mW and -2 V Schottky bias). **a** Measured power spectrum normalized to the maximum; the inset shows a zoom of the sharp peak, exhibiting a linewidth of 10 Hz. **b** The single-sideband noise is shown (black); for comparison the theoretical minimum given by the thermal noise of the resonator is shown.

References

- [1] D. W. Carr, L. Sekaric, and H. G. Craighead, “Measurement of nanomechanical resonant structures in single-crystal silicon” *J. Vac. Sci. Technol. B* **16**, 3821–3824 (1998).
- [2] T. Thundat, E. Finot, Z. Hu, R. H. Ritchie, G. Wu, and A. Majumdar, “Chemical sensing in Fourier space” *Appl. Phys. Lett.* **77**, 4061–4063 (2000).
- [3] H. R. Bohm, S. Gigan, F. Blaser, A. Zeilinger, M. Aspelmeyer, G. Langer, D. Bauerle, J. B. Hertzberg, and K. C. Schwab, “High reflectivity high-Q micromechanical Bragg mirror” *Appl. Phys. Lett.* **89**, 223 101 (2006).
- [4] N. O. Azak, M. Y. Shagam, D. M. Karabacak, K. L. Ekinci, D. H. Kim, and D. Y. Jang, “Nanomechanical displacement detection using fiber-optic interferometry” *Appl. Phys. Lett.* **91**, 093 112 (2007).
- [5] M. Li, W. H. P. Pernice, C. Xiong, T. Baehr-Jones, M. Hochberg, and H. X. Tang, “Harnessing optical forces in integrated photonic circuits” *Nature* **456**, 480–484 (2008).
- [6] M. Li, W. H. P. Pernice, and H. X. Tang, “Broadband all-photonic transduction of nanocantilevers” *Nat. Nanotechnol.* **4**, 377–382 (2009).
- [7] I. Favero, S. Stapfner, D. Hunger, P. Paulitschke, J. Reichel, H. Lorenz, E. M. Weig, and K. Karrai, “Fluctuating nanomechanical system in a high finesse optical microcavity” *Opt. Express* **17**, 12 813–12 820 (2009).
- [8] G. Anetsberger, O. Arcizet, Q. P. Unterreithmeier, R. Riviere, A. Schliesser, E. M. Weig, J. P. Kotthaus, and T. J. Kippenberg, “Near-field cavity optomechanics with nanomechanical oscillators” *Nat. Phys.* **5**, 909–914 (2009).
- [9] M. Eichenfield, R. Camacho, J. Chan, K. J. Vahala, and O. Painter, “A picogram- and nanometre-scale photonic-crystal optomechanical cavity” *Nature* **459**, 550–556 (2009).
- [10] A. N. Cleland and M. L. Roukes, “External control of dissipation in a nanometer-scale radiofrequency mechanical resonator” *Sens. Actuators, A* **72**, 256–261 (1999).
- [11] M. D. LaHaye, O. Buu, B. Camarota, and K. C. Schwab, “Approaching the Quantum Limit of a Nanomechanical Resonator” *Science* **304**, 74–77 (2004).

- [12] P. A. Truitt, J. B. Hertzberg, C. C. Huang, K. L. Ekinci, and K. C. Schwab, “Efficient and Sensitive Capacitive Readout of Nanomechanical Resonator Arrays” *Nano Lett.* **7**, 120–126 (2007).
- [13] R. He, X. L. Feng, M. L. Roukes, and P. Yang, “Self-Transducing Silicon Nanowire Electromechanical Systems at Room Temperature” *Nano Lett.* **8**, 1756–1761 (2008).
- [14] S. Etaki, M. Poot, I. Mahboob, K. Onomitsu, H. Yamaguchi, and H. S. J. van der Zant, “Motion detection of a micromechanical resonator embedded in a d.c. SQUID” *Nat. Phys.* **4**, 785–788 (2008).
- [15] C. A. Regal, J. D. Teufel, and K. W. Lehnert, “Measuring nanomechanical motion with a microwave cavity interferometer” *Nat. Phys.* **4**, 555 (2008).
- [16] A. K. Huettel, G. A. Steele, B. Witkamp, M. Poot, L. P. Kouwenhoven, and H. S. J. van der Zant, “Carbon Nanotubes as Ultrahigh Quality Factor Mechanical Resonators” *Nano Lett.* **9**, 2547–2552 (2009).
- [17] C. H. Metzger and K. Karrai, “Cavity cooling of a microlever” *Nature* **432**, 1002 (2004).
- [18] J. Rosenberg, Q. Lin, and O. Painter, “Static and dynamic wavelength routing via the gradient optical force” *Nat. Photonics.* **3**, 478–483 (2009).
- [19] G. S. Wiederhecker, L. Chen, A. Gondarenko, and M. Lipson, “Controlling photonic structures using optical forces” *Nature* **462**, 633–636 (2009).
- [20] C. Xiong, W. Pernice, M. Li, M. Rooks, and H. X. Tang, “Adiabatic embedment of nanomechanical resonators in photonic microring cavities” *Appl. Phys. Lett.* **96**, 263 101 (2010).
- [21] S. M. Sze, *Physics of Semiconductor Devices* (Wiley, New York, 1969).
- [22] D. T. Gillespie, “The mathematics of Brownian motion and Johnson noise” *Am. J. Phys.* **64**, 225–240 (1996).
- [23] A. H. Nayfeh and D. T. Mook, *Nonlinear Oscillations* (Wiley, New York, 1995).
- [24] G. Gonzales, *Foundations of Oscillator Circuit Design* (Artech House, 2007).
- [25] B. Yurke, D. S. Greywall, A. N. Pargellis, and P. A. Busch, “Theory of amplifier-noise evasion in an oscillator employing a nonlinear resonator” *Phys. Rev. A* **51**, 4211–4229 (1995).
- [26] X. L. Feng, C. J. White, A. Hajimiri, and M. L. Roukes, “A self-sustaining ultrahigh-frequency nanoelectromechanical oscillator” *Nat. Nanotechnol.* **3**, 342–346 (2008).

Chapter 5

Nonlinear Switching Dynamics

The present chapter is based on the publication shown in chapter E, see pages 69 et seq.

Exciting an oscillator to large amplitudes, the approximation of a linear restoring force often has to be extended to include higher order components. The systems exhibiting nonlinearity are diverse including the relativistic motion of electrons in a magnetic field [1], light passing through nonlinear media [2] current through a Josephson junction [3], and carbon nanotubes [4].

Subject to suitable actuation a bistability regime develops [5] involving phenomena such as jumps [2], hysteresis [1] and transitions between the stable states [5–9]. These are mediated by a rapid change in frequency [5] or noise [6–9]. Complementary, we utilize resonant RF-pulses to actively manipulate the resonator's state and thereby obtain a basic version of a mechanical memory element [10, 11].

Nanomechanical oscillators provide convenient means to study nonlinear phenomena as they exhibit fairly low drifts and fast response times that allow to map out a large set parameters [5].

The resonator is excited using the dielectric actuation scheme, described in chapter 1, its motion is recorded with an on-chip photodetector, see chapter 4. The equation of motion is the so called Duffing equation (with $x[t]$, f_0 , Q , α_3 , k , f displacement, resonance frequency, mechanical quality factor, cubic restoring force parameter, actuation strength and frequency).

$$x''[t] + \frac{2\pi f_0}{Q}x'[t] + (2\pi f_0)^2x[t] + \alpha_3x[t]^3 = k \cos[2\pi ft] \quad (5.1)$$

As shown in the appendix (section G.5) this equation is solved to describe the dynamics of the oscillatory state $x[t] = a[t] \cos[2\pi ft + \gamma[t]]$:

$$\begin{aligned}
a'[t] &= -\frac{\pi f_0 a[t]}{Q} + \frac{k \sin[\gamma[t]]}{4\pi f_0} \\
\gamma'[t] &= 2\pi(f - f_0) - \frac{3\alpha_3 a[t]^2}{16\pi f_0} + \frac{k \cos[\gamma[t]]}{4\pi f_0 a[t]}
\end{aligned}
\tag{5.2}$$

We determine the mechanical parameters of eq. 5.1 by measuring a nonlinear resonance as seen in chapter 2 and fitting a quasistatic solution of eqs. 5.2 to the data.

Any initial state converges towards one of the two stable states, dividing the resonator's phase space into two areas (basins) of attraction. For a fixed actuation frequency we calculate [5] the stable states and the area from eq. 5.2 as shown in fig. 5.1(a) as black and white areas.

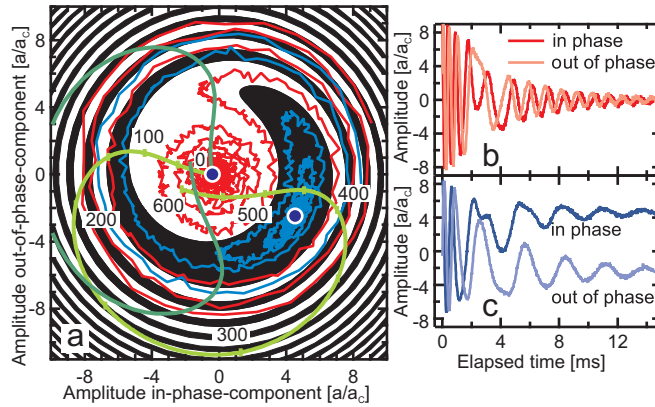


Figure 5.1: **Time evolution of the resonator state** **a** The resonator's phase space is shown as the quadrature components of the oscillation. Subject to hard excitation two stable states exist (blue points). Each state has a (calculated) area (basin) of attraction shown in black and white. The traces (red and blue) display the measured convergence of an excited state towards the stable states. The smooth green curves show the calculated response starting from the lower stable state subject to an 18-fold larger additional excitation and relative phase $\phi = 262^\circ, 172^\circ$ (light and dark green, respectively). **b** and **c** display the same experimentally obtained relaxation curve as **a**, the quadrature components are plotted versus time.

We shall first consider relaxation towards the stable states and utilize this behavior to quantify the action of applying pulses. We therefore prepare the resonator in the bistable regime by applying a constant actuation at a frequency of 1 kHz above the resonance frequency of the string. We then apply a short and resonant RF-pulse to move the resonator state away from equilibrium. Immediately after the end of the pulse we record the resonator's relaxing towards one of the stable states as shown as red and blue traces in Figure 5.1(a).

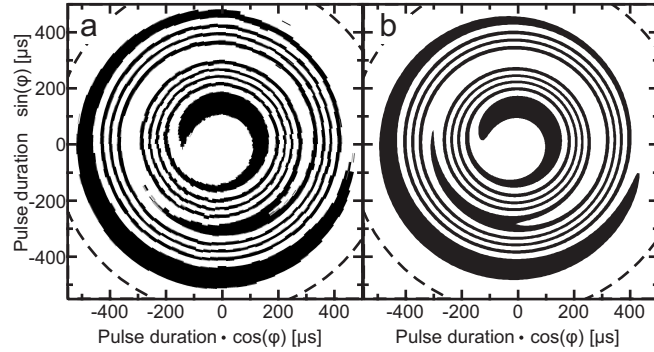


Figure 5.2: **Time evolution during RF-pulse** **a** the measured final state (after the relaxation) is shown as black/white after vs. length and phase of the applied an RF-pulse. The excitation amplitude is always the same; the resonator is prepared in the lower stable state before the pulse is applied. **b** Simulation of the measurement employing no fit parameters.

Figure 5.1(b,c) show the same data with the two oscillatory quadrature components plotted versus time. The two green traces in Fig. 5.1(a) display the calculated mechanical response if in addition to the constant drive the RF pulse actuates the resonator. It is this response that we want to study in detail. We therefore prepare the resonator in its lower stable state and apply an RF pulse of fixed amplitude and systematically vary its duration and phase (with respect to the constant background actuation).

Figure 5.2(a) shows the measured data arranged in a polar plot; (b) is a calculation based on the numerical integration of eqs. 5.2, employing no fit parameters.

The agreement allows us to quantitatively predict the action of the pulse and calculate the parameters necessary in order to directly switch between the stable states (without any post-pulse relaxation).

In fig. 5.3(a) we show the out-of-phase component of the oscillation versus time as we apply a properly chosen pulse. Immediately after the end of the end of the pulse the recorded state can be seen to be stationary, complementary to the traces displayed in fig. 5.1(b,c).

We therefore conclude that we are able to directly address the desired stable state. The same holds true if we apply another pulse having different parameters to switch back to the initial stable state, see fig. 5.3(a) and apply these consecutively 5.3(b,c). As no relaxation is needed to switch or record the state our scheme overcomes typical response time scales $Q/f_0 \approx 20$ ms and thereby exceeds demonstrated controlled switching speeds by a factor of 1000, ref. [11, 12].

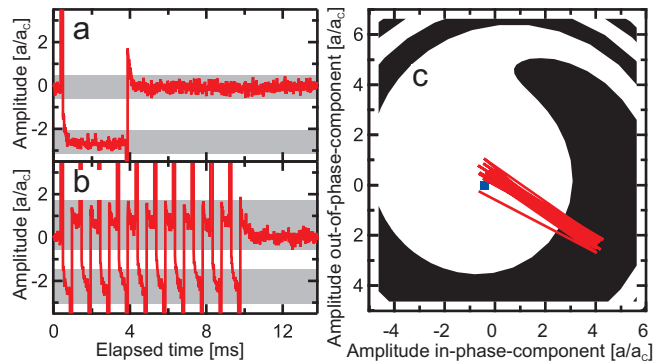


Figure 5.3: **Switching between the stable states** **a** Measured out of phase component of the oscillation amplitude; the gray areas highlight the stable states. Applying a suitable RF-pulse directly switches between the stable states (the visible overshoots are a result of cross-talk). **b** Consecutive switching with a repetition rate is 1 kHz, faster than the relaxation rate given by $\omega_0/Q \approx 50$ Hz. **c** Same data, plotted in phase space.

References

- [1] G. Gabrielse, H. Dehmelt, and W. Kells, “Observation of a Relativistic, Bistable Hysteresis in the Cyclotron Motion of a Single Electron” *Phys. Rev. Lett.* **54**, 537–539 (1985).
- [2] B. Ritchie and C. M. Bowden, “Dynamical response and switching of an optically bistable anharmonic oscillator” *Phys. Rev. A* **32**, 2293 (1985).
- [3] I. Siddiqi, R. Vijay, F. Pierre, C. M. Wilson, M. Metcalfe, C. Rigetti, L. Frunzio, and M. H. Devoret, “RF-Driven Josephson Bifurcation Amplifier for Quantum Measurement” *Phys. Rev. Lett.* **93**, 207 002 (2004).
- [4] A. Alippi and A. Bettucci, “Nonlinear strings as bistable elements in acoustic wave propagation” *Phys. Rev. Lett.* **63**, 1230 (1989).
- [5] I. Kozinsky, H. W. C. Postma, O. Kogan, A. Husain, and M. L. Roukes, “Basins of Attraction of a Nonlinear Nanomechanical Resonator” *Phys. Rev. Lett.* **99**, 207 201 (2007).
- [6] J. S. Aldridge and A. N. Cleland, “Noise-Enabled Precision Measurements of a Duffing Nanomechanical Resonator” *Phys. Rev. Lett.* **94**, 156 403 (2005).
- [7] C. Stambaugh and H. B. Chan, “Supernarrow Spectral Peaks near a Kinetic Phase Transition in a Driven Nonlinear Micromechanical Oscillator” *Phys. Rev. Lett.* **97**, 110 602 (2006).
- [8] R. Almog, S. Zaitsev, O. Shtempluck, and E. Buks, “Signal amplification in a nanomechanical Duffing resonator via stochastic resonance” *Appl. Phys. Lett.* **90**, 013 508 (2007).
- [9] R. L. Badzey and P. Mohanty, “Coherent signal amplification in bistable nanomechanical oscillators by stochastic resonance” *Nature* **437**, 995–998 (2005).
- [10] R. L. Badzey, G. Zolfagharkhani, A. Gaidarzhy, and P. Mohanty, “A controllable nanomechanical memory element” *Appl. Phys. Lett.* **85**, 3587–3589 (2004).
- [11] I. Mahboob and H. Yamaguchi, “Bit storage and bit flip operations in an electromechanical oscillator” *Nat. Nanotechnol.* **3**, 275 (2008).

References

- [12] D. N. Guerra, M. Imboden, and P. Mohanty, “Electrostatically actuated silicon-based nanomechanical switch at room temperature” *Appl. Phys. Lett.* **93**, 033515 (2008).

Chapter 6

Damping Characteristics

The present chapter is based on the publication shown in chapter F, see pages 73 et seq.

A central characteristic of an oscillatory motion is its energy loss that is mostly parameterized as the quality (Q) factor. It is defined as the energy stored in the oscillatory motion divided by the energy loss per oscillation

$$Q \equiv 2\pi \frac{U}{\Delta U} \quad (6.1)$$

A high quality factor means that the oscillatory degree of freedom is only weakly coupled to its environment. The corresponding sharp resonance enhances the sensitivity of the resonator, see e.g. [1, 2], facilitates cooling of the thermal motion [3–5]. Yet in most cases a fundamental understanding of the physical processes has not been achieved. This may be partially caused by the fact that a broad spectrum of different resonators is investigated [6–10], varying in material as well as fabrication methods.

In 2006 it was experimentally shown that doubly-clamped silicon nitride resonators under high tensile stress exhibit largely enhanced quality factors when compared to stress-free resonators fabricated from the same material [11] at comparable frequencies. This effect has been reproduced with GaAs microresonators [12], polymer resonators [9] and in simulations on metal wires [13] and graphene [14]. The underlying mechanism of the enhancement however has not yet been explained, in particular it has been speculated that stress causes decreased damping [15].

We present investigations based on continuum elastic theory that relate the damping to the local oscillatory strain in the mechanical resonator. The strain can be inferred from the spatial profile $u[x]$ of the oscillation, as schematically depicted in Fig. 6.1. We therefore solve the corresponding differential equation (h, ρ, f are height, density and eigenfrequency of the resonator; E_1, σ_0 are the (unknown) real elastic Young's Modulus and pre-stress):

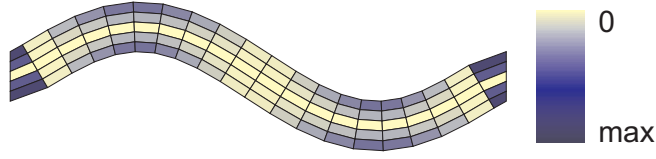


Figure 6.1: **Strain Distribution** The strain caused by the oscillation is schematically shown. In order to emphasize that the sign of the stress (tensile or compressive) is irrelevant in our damping model, the absolute value is color-coded.

$$\frac{1}{12}E_1h^2\frac{\partial^4}{\partial x^4}u[x] - \sigma\frac{\partial^2}{\partial x^2}u[x] - \rho(2\pi f)^2u[x] = 0 \quad (6.2)$$

A set of resonances, varying in resonator length and harmonic mode are measured using transduction methods as explained in chapter 1. The solution of eq. 6.2 satisfying the boundary conditions of a doubly-clamped beam is fitted to reproduce the measured frequencies as seen in fig. 6.2.

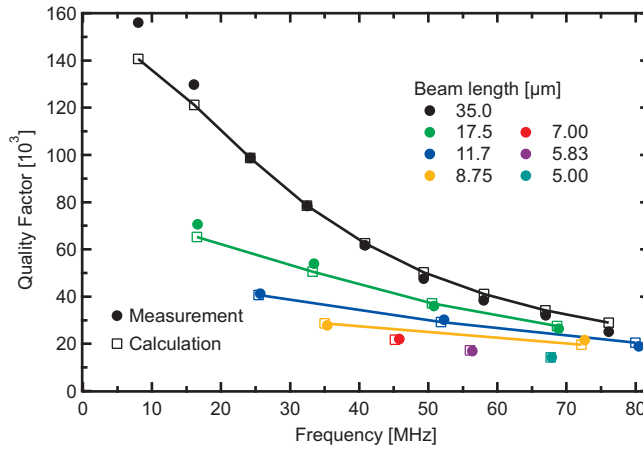


Figure 6.2: **Resonance Frequency and Mechanical Quality Factor** Measured and calculated response of the mechanical resonators; the different beam lengths are color-coded; the harmonic modes of the same beam are interconnected for clarity. The frequencies are reproduced using continuum elastic theory, fitting to the frequencies yields $E_1 = 163$ GPa, $\sigma_0 = 839$ MPa Young's Modulus and pre-stress. The quality factor is calculated from the strain profile using a Zener model with one fit parameter.

We thereby obtain the elastic parameters namely $E = 163$ GPa and $\sigma_0 = 839$ MPa in excellent agreement with the values obtained by the investigation of the nonlinear behavior in chapter 2.

To relate the oscillating local strain with energy dissipation, we apply the model of Zener [16], modifying the (scalar) stress-strain relation to account for phase lags ($\sigma = E\epsilon$ with $E = E_1 + \iota E_2$ complex). This leaves a single fit parameter to reproduce the measured quality factors as shown in fig. 6.2. The agreement is seen to be excellent, it can be further improved by letting E_2 depend on frequency, see section G.6.3.

A similar calculation can be found in Ref. [17] considering thermoelastic damping [18]. Yet the effect is shown to be negligible and the underlying enhancement in quality factor is not specified, as we do now.

The strain caused by the oscillation can be separated into two contributions: local bending and overall elongation; please refer to section G.6.1 for details. It is found that the effect of elongation is a minor correction to the oscillatory strain for small amplitudes, being responsible for the energy loss in our model. However, its contribution to the stored elastic energy is boosted by the pre-stress, see section G.6.2. Therefore, one is able to increase the stored energy with prestress without introducing energy loss at the same rate, in total the quality factor increases. This effect can be seen to be most prominent for large antinode-separation, as there the bending is less pronounced.

This finding shall be treated somewhat more precisely: the bending strain is linear in displacement whereas the elongation strain is quadratic. The latter is therefore very small and so is its contribution to energy loss; at very high amplitudes however, it may become noticeable, see section G.7.

Considering the elastic energy, the situation is different; the bending energy is quadratic in strain; however the elongation energy is linear in (solely elongation) strain. Both energies are therefore quadratic in displacement.

Figure 6.3(a) shows a calculation of the relevant energies (losses) versus different applied overall stress. Please note that in our model the energy loss is proportional to the bending energy, section G.6.1 and G.6.2. A relatively weak increase of energy loss with increasing stress is seen; this is caused by the changing mode profile.

For low stress the energy is dominated by bending; as for higher stress the total energy is increasingly dominated by elongation energy; the ratio of total energy and energy loss (bending energy) highlighted by the gray area directly shows the boost of quality factor with applied stress. It is noteworthy that increasing the stress also causes the linewidth to decrease, see section G.6.4.

Figure 6.3(b) shows the resulting parametric dependence of quality factor on resonance frequency, the almost linear relation is consistent with published results [19].

We consider now possible physical mechanisms that cause the energy loss in our system. As shown in the supplement (section G.6.5) damping caused by thermoelastic [18, 20], Akhiezer-relaxation [20, 21] and clamping losses [22, 23] are of minor importance. Therefore, energy loss related to defects is regarded as dominant; several arguments favor this concept. As shown in section G.6.6 a non-optimized dry etch step leads to quality factors that are uniformly reduced; yet the damping model is still valid using an increased loss modulus E_2 . The dry etch is expected to introduce

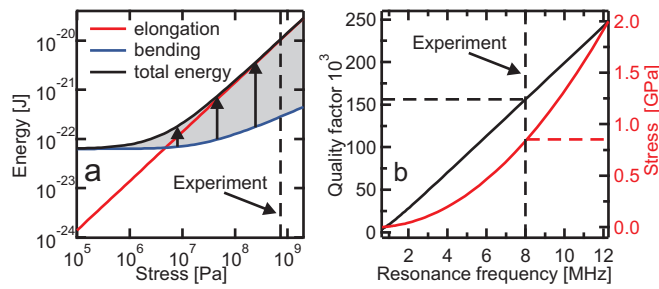


Figure 6.3: **Elastic Energy and Quality Factor** **a** The calculated elastic energies vs. prestress are shown for the fundamental mode of a $35\ \mu\text{m}$ beam. The bending energy is proportional to the energy loss; therefore the gray area represents the enhancement in quality factor with applied stress. **b** The quality factor vs. resonance frequency is parametrically shown for varying prestress for comparison with published results.

sterical and compositional defects, yet has no influence on the above cited damping mechanism. In addition, a model calculation shows that a defect ensemble having a broad range of relaxation times and energies leads to a frequency-independent loss modulus [24], the central assumption of our model. The quality factor of our strings if they were relaxed can be calculated to be approximately 4000. Silicon nitride resonators have been cooled to liquid helium temperature without exhibiting a drastic change in quality factor [15]. This magnitude is well in the "glassy range" exhibited by amorphous material, the damping there is described by two-level fluctuators [25].

However, these are considered to be uniformly distributed throughout resonator, whereas the above finding of increased damping points towards defects that are predominantly concentrated at or near the surface. Our model assumes a uniform distribution of defect states along the beam and cannot resolve any question, concerning the distribution of damping centers in the cross section, see also section G.6.7.

Given a multitude of experiments that point towards defects [6, 9, 10, 14, 26–30], it is highly likely that these mediate the energy loss. Our findings suggest that either ultra-pure systems [31] or systems in which the enhancement of quality factor with stress is most prominent [32, 33] in accordance with the cited publications.

References

- [1] T. D. Stowe, K. Yasumura, T. W. Kenny, D. Botkin, K. Wago, and D. Rugar, “Attonewton force detection using ultrathin silicon cantilevers” *Appl. Phys. Lett.* **71**, 288–290 (1997).
- [2] A. N. Cleland, “Thermomechanical noise limits on parametric sensing with nanomechanical resonators” *New J. Phys.* **7**, 235 (2005).
- [3] C. H. Metzger and K. Karrai, “Cavity cooling of a microlever” *Nature* **432**, 1002 (2004).
- [4] C. A. Regal, J. D. Teufel, and K. W. Lehnert, “Measuring nanomechanical motion with a microwave cavity interferometer” *Nat. Phys.* **4**, 555 (2008).
- [5] P. Rabl, P. Cappellaro, M. V. G. Dutt, L. Jiang, J. R. Maze, and M. D. Lukin, “Strong magnetic coupling between an electronic spin qubit and a mechanical resonator” *Phys. Rev. B* **79**, 041302 (2009).
- [6] K. Y. Yasumura, T. D. Stowe, E. M. Chow, T. Pfafman, T. W. Kenny, B. C. Stipe, and D. Rugar, “Quality factors in micron- and submicron-thick cantilevers” *J. Microelectromech. S.* **9**, 117–125 (2000).
- [7] L. Sekaric, J. M. Parpia, H. G. Craighead, T. Feygelson, B. H. Houston, and J. E. Butler, “Nanomechanical resonant structures in nanocrystalline diamond” *Appl. Phys. Lett.* **81**, 4455–4457 (2002).
- [8] X. L. Feng, R. He, P. Yang, and M. L. Roukes, “Very High Frequency Silicon Nanowire Electromechanical Resonators” *Nano Lett.* **7**, 1953–1959 (2007).
- [9] S. Schmid and C. Hierold, “Damping mechanisms of single-clamped and pre-stressed double-clamped resonant polymer microbeams” *J. Appl. Phys.* **104**, 093516 (2008).
- [10] S. Fukami, T. Arie, and S. Akita, “Temperature Dependence of Cantilevered Carbon Nanotube Oscillation” *Jpn. J. Appl. Phys.* **49**, 06GK02 (2010).
- [11] S. S. Verbridge, J. M. Parpia, R. B. Reichenbach, L. M. Bellan, and H. G. Craighead, “High quality factor resonance at room temperature with nanostings under high tensile stress” *J. Appl. Phys.* **99**, 124304 (2006).

- [12] H. Yamaguchi, K. Kato, Y. Nakai, K. Onomitsu, S. Warisawa, and S. Ishihara, “Improved resonance characteristics of GaAs beam resonators by epitaxially induced strain” *Appl. Phys. Lett.* **92**, 251 913 (2008).
- [13] S. Y. Kim and H. S. Park, “Utilizing Mechanical Strain to Mitigate the Intrinsic Loss Mechanisms in Oscillating Metal Nanowires” *Phys. Rev. Lett.* **101**, 215 502 (2008).
- [14] S. Y. Kim and H. S. Park, “The Importance of Edge Effects on the Intrinsic Loss Mechanisms of Graphene Nanoresonators” *Nano Lett.* **9**, 969–974 (2009).
- [15] D. R. Southworth, R. A. Barton, S. S. Verbridge, B. Ilic, A. D. Fefferman, H. G. Craighead, and J. M. Parpia, “Stress and Silicon Nitride: A Crack in the Universal Dissipation of Glasses” *Phys. Rev. Lett.* **102**, 225 503 (2009).
- [16] C. Zener, “Internal Friction in Solids II. General Theory of Thermoelastic Internal Friction” *Phys. Rev.* **53**, 90–99 (1938).
- [17] S. Kumar and M. Haque, “Reduction of thermo-elastic damping with a secondary elastic field” *J. Sound Vib.* **318**, 423–427 (2008).
- [18] R. Lifshitz and M. L. Roukes, “Thermoelastic damping in micro- and nanomechanical systems” *Phys. Rev. B* **61**, 5600–5609 (2000).
- [19] S. Verbridge, D. Shapiro, H. Craighead, and J. Parpia, “Macroscopic Tuning of Nanomechanics: Substrate Bending for Reversible Control of Frequency and Quality Factor of Nanostring Resonators” *Nano Lett.* **7**, 1728–1735 (2007).
- [20] A. A. Kiselev and G. J. Iafrate, “Phonon dynamics and phonon assisted losses in Euler-Bernoulli nanobeams” *Phys. Rev. B* **77**, 205 436 (2008).
- [21] A. Akhieser, “On the absorption of sound in solids” *J. Phys. - USSR* **1**, 277–287 (1939).
- [22] Z. Hao, A. Erbil, and F. Ayazi, “An analytical model for support loss in micro-machined beam resonators with in-plane flexural vibrations” *Sens. Actuators, A* **109**, 156–164 (2003).
- [23] I. Wilson-Rae, “Intrinsic dissipation in nanomechanical resonators due to phonon tunneling” *Phys. Rev. B* **77**, 245 418 (2008).
- [24] J. JACKLE, “Ultrasonic Attenuation In Glasses At Low-temperatures” *Z. Phys.* **257**, 212–223 (1972).
- [25] R. O. Pohl, X. Liu, and E. Thompson, “Low-temperature thermal conductivity and acoustic attenuation in amorphous solids” *Rev. Mod. Phys.* **74**, 991 (2002).
- [26] D. W. Carr, S. Evoy, L. Sekaric, H. G. Craighead, and J. M. Parpia, “Measurement of mechanical resonance and losses in nanometer scale silicon wires” *Appl. Phys. Lett.* **75**, 920–922 (1999).

-
- [27] J. Yang, T. Ono, and M. Esashi, “Surface effects and high quality factors in ultrathin single-crystal silicon cantilevers” *Appl. Phys. Lett.* **77**, 3860–3862 (2000).
- [28] J. L. Yang, T. Ono, and M. Esashi, “Energy dissipation in submicrometer thick single-crystal silicon cantilevers” *J. Microelectromech. S.* **11**, 775–783 (2002).
- [29] Y. Wang, J. Henry, A. Zehnder, and M. Hines, “Surface Chemical Control of Mechanical Energy Losses in Micromachined Silicon Structures” *J. Phys. Chem. B* **107**, 14 270–14 277 (2003).
- [30] G. Anetsberger, R. Riviere, A. Schliesser, O. Arcizet, and T. J. Kippenberg, “Ultralow-dissipation optomechanical resonators on a chip” *Nat. Photonics* **2**, 627–633 (2008).
- [31] A. K. Huettel, G. A. Steele, B. Witkamp, M. Poot, L. P. Kouwenhoven, and H. S. J. van der Zant, “Carbon Nanotubes as Ultrahigh Quality Factor Mechanical Resonators” *Nano Lett.* **9**, 2547–2552 (2009).
- [32] J. D. Thompson, B. M. Zwickl, A. M. Jayich, F. Marquardt, S. M. Girvin, and J. G. E. Harris, “Strong dispersive coupling of a high-finesse cavity to a micromechanical membrane” *Nature* **452**, 72–75 (2008).
- [33] D. J. Wilson, C. A. Regal, S. B. Papp, and H. J. Kimble, “Cavity Optomechanics with Stoichiometric SiN Films” *Phys. Rev. Lett.* **103**, 207 204 (2009).

References

Summary and Perspectives

In the framework of this thesis, the resonant motion of strained nanomechanical oscillators has been investigated at room temperature. Its essential results and ongoing and possible future projects shall be briefly discussed.

A central aspect of the work is the development of new transduction schemes, also suited for insulating resonators. Chapter 1 introduces such a new scheme that relies on the dielectric interaction: the polarizable mechanical element is placed in an inhomogeneous electric field. Consequently, it gets attracted towards higher field intensity; in turn a mechanical displacement leads to an electrical capacitance change. The main focus of the publication is to demonstrate simple actuation. However it is straightforward to extend the scheme to allow for sensitive detection by measuring the capacitance change. This can be accomplished by either measuring the creation of charge [1, 2], or transform it into a modulation of the resonance frequency of an LC circuit [3, 4] (see also the supplement, section G.2.2). Both approaches are currently pursued at the chair, yet not concluded.

The transduction mechanism presented in chapter 3 similarly utilizes gradient fields: the tail of an optical mode circulating in a micro-cavity dielectrically interacts with a nanomechanical resonator. The resulting phase shift of the optical path is enhanced by the optical cavity and allows to sensitively detect the displacement of the oscillator. To further increase sensitivity, at least two approaches are straightforward and have already been implemented [?]. Decreasing the wavelength increases the slope of the decay of the evanescent field and thereby the optomechanical coupling. Reducing the total optical mode-volume (the size of the micro-toroid) enhances the relative optical frequency shift with mechanical displacement, as it scales with the optical mode volume interacting with the mechanical resonator divided by the total mode volume. Whereas at room temperature this latter modification leads to an increased thermorefractive noise, it suggests that an imprecision of 10 dB below the standard quantum limit can be reached by (conventionally) cooling the optical resonator to 10 K.

In chapter 4 an integrable detection scheme is presented; the optical intensity modulation with beam displacement is converted into a photocurrent generated by a nearby Schottky-contact. There are again straightforward ideas to further increase the sensitivity (as pointed out in the paper): implementing an optical resonant structure [5, 6] can increase the detected signal strength as well as the modulation

depth with mechanical displacement.

The focus of chapter 2 is two-fold: by implementing a downconversion technique the limited bandwidth of the employed photodetector can be exceeded. The present implementation switches the employed laser completely on and off, resulting in optical noise; however, achieving a sine-like modulation with acousto-optic modulators should largely reduce the noise and enable the detection of yet higher frequencies. It is noteworthy that a stroboscopic technique also eliminates cross-talk; it therefore may be useful to combine it with the on-chip detection scheme discussed in section 4. The second topic of the paper was to yield additional insight into the (elastic) mechanics based on the nonlinear characteristics of the oscillation. Deducing that a long beam could be treated as string, allowed to separate bending from stretching effects and isolate the mechanical parameters. These parameters could then be utilized to convert the measured signal into mechanical displacement.

A further insight into the nonlinear mechanics is shown in chapter 5. There the response of the system subject to short, resonant RF-pulses is studied and their application to implement a nanomechanical memory element. A possible continuation is to apply stronger pulses to enable faster switching and eventually observe the break-down of the perturbative modeling. Another extension is to actuate the resonators to amplitudes that display effects of not only 3rd but also 5th order terms in displacement [7]. Presumably, a more complex topography and a tristable state can be observed.

Lastly, the damping of the nanomechanical structures has been investigated, chapter 6. The work demonstrates that a simple strain-based Zener model can be employed to quantitatively predict the quality factor of the mechanical resonators. Several arguments are given that clearly point towards local defects to cause the observed damping. Here, work can be performed to yield further insight: the presented data have been taken at room temperature. The damping exhibited by amorphous materials is mostly studied at low temperature and can be modeled assuming the defects to be two-level systems covering a broad range in energy and relaxation rate. In particular, it seems appealing to study the damping behavior subject to sudden changes in the equilibrium of the defects. This change could be implemented by applying a different stress (see also section G.1) or the electric field as these systems display a dipolar moment ^a.

There are more effects that can be investigated and may be related to defects: subject to DC-bias the resonators show a drift in eigenfrequency, see section G.2.3. The dipolar moment of the beams thereby changes with time, to clarify the physical origin more work is required possibly including different temperatures.

Applying the damping model in the highly excited regime (section G.7) shows that at large amplitudes, a deviation from linear damping may be observed as a geometric (not microscopic) consequence. The challenge here probably is to deal with the elastic nonlinearities.

^aS. Ludwig, private communication

References

- [1] P. A. Truitt, J. B. Hertzberg, C. C. Huang, K. L. Ekinici, and K. C. Schwab, “Efficient and Sensitive Capacitive Readout of Nanomechanical Resonator Arrays” *Nano Lett.* **7**, 120–126 (2007).
- [2] Q. P. Unterreithmeier, E. M. Weig, and J. P. Kotthaus, “Universal transduction scheme for nanomechanical systems based on dielectric forces” *Nature* **458**, 1001–1004 (2009).
- [3] C. A. Regal, J. D. Teufel, and K. W. Lehnert, “Measuring nanomechanical motion with a microwave cavity interferometer” *Nat. Phys.* **4**, 555 (2008).
- [4] J. D. Teufel, T. Donner, M. A. Castellanos-Beltran, J. W. Harlow, and K. W. Lehnert, “Nanomechanical motion measured with an imprecision below that at the standard quantum limit” *Nat. Nanotechnol.* **4**, 820–823 (2009).
- [5] M. Eichenfield, R. Camacho, J. Chan, K. J. Vahala, and O. Painter, “A picogram- and nanometre-scale photonic-crystal optomechanical cavity” *Nature* **459**, 550–556 (2009).
- [6] A. N. Grigorenko, N. W. Roberts, M. R. Dickinson, and Y. Zhang, “Nanometric optical tweezers based on nanostructured substrates” *Nat. Photonics.* **2**, 365–370 (2008).
- [7] N. Kacem and S. Hentz, “Bifurcation topology tuning of a mixed behavior in nonlinear micromechanical resonators” *Appl. Phys. Lett.* **95**, 183104–3 (2009).

References

Universal transduction scheme for nanomechanical systems based on dielectric forces

Quirin P. Unterreithmeier¹, Eva M. Weig¹ & Jörg P. Kotthaus¹

Any polarizable body placed in an inhomogeneous electric field experiences a dielectric force. This phenomenon is well known from the macroscopic world: a water jet is deflected when approached by a charged object. This fundamental mechanism is exploited in a variety of contexts—for example, trapping microscopic particles in an optical tweezer¹, where the trapping force is controlled via the intensity of a laser beam, or dielectrophoresis², where electric fields are used to manipulate particles in liquids. Here we extend the underlying concept to the rapidly evolving field of nanoelectromechanical systems^{3,4} (NEMS). A broad range of possible applications are anticipated for these systems^{5,6,7}, but drive and detection schemes for nanomechanical motion still need to be optimized^{8,9}. Our approach is based on the application of dielectric gradient forces for the controlled and local transduction of NEMS. Using a set of on-chip electrodes to create an electric field gradient, we polarize a dielectric resonator and subject it to an attractive force that can be modulated at high frequencies. This universal actuation scheme is efficient, broadband and scalable. It also separates the driving scheme from the driven mechanical element, allowing for arbitrary polarizable materials and thus potentially ultralow dissipation NEMS¹⁰. In addition, it enables simple voltage tuning of the mechanical resonance over a wide frequency range, because the dielectric force depends strongly on the resonator–electrode separation. We use the modulation of the resonance frequency to demonstrate parametric actuation^{11,12}. Moreover, we reverse the actuation principle to realize dielectric detection, thus allowing universal transduction of NEMS. We expect this combination to be useful both in the study of fundamental principles and in applications such as signal processing and sensing.

Common actuation mechanisms of nanomechanical resonators can be divided into local on-chip schemes and schemes relying on external excitation. The former are based on voltage-induced forces such as internal piezo-electrical^{9,12}, capacitive¹¹, magnetomotive¹³, electrothermal¹⁴ or static dipole-based dielectric¹⁵. Although highly integrable and efficient, these schemes impose constraints on material choice and geometry and thus mostly suffer from large dissipation¹⁶. The latter employ external actuation such as photothermal¹⁷ or inertia-based piezo-actuated schemes¹⁰, which is less restrictive on system choice and hence advantageous in terms of dissipation^{3,10}. However, attaining high-frequency actuation as well as integrability remains a challenge.

Here, we introduce a driving scheme that integrates external, yet local actuation for arbitrary resonators, directly based on electrical signals. It enables independent optimization of both the actuation and the resonant element. Our mechanism relies solely on dielectric interaction: A polarizable material experiences an attractive force in an inhomogeneous electric field directed towards the maximum field strength. In our case the polarizable element is a doubly clamped

silicon nitride beam, as depicted in Fig. 1a, which serves as a low-dissipation radio-frequency (r.f.) resonator¹⁰. The inhomogeneous field in the beam plane is created by two subjacent gold electrodes (see inset of Fig. 1b). A static voltage $V_{d.c.}$ (direct current, d.c.) applied to the electrodes induces a strong dipolar moment in the resonator that in turn experiences an attractive force directed towards the electrodes. Modulating $V_{d.c.}$ with an r.f. signal $V_{r.f.}$ gives rise to an oscillating force component that drives the resonator perpendicularly to the chip plane.

To obtain quantitative insight into the dielectric forces, we carried out finite element simulations for the given geometry (see Fig. 1). The black line in Fig. 1b depicts the dielectric force acting on the resonator as a function of its distance d from the substrate. The force exhibits a maximum at a distance that is comparable, though somewhat smaller than our resonator–substrate separation of $d \approx 300$ nm. In addition, the simulations can be used to extract information on the underlying circuitry. The mutual capacitance of the electrodes is $C_{mutual} \approx 1.5$ fF. Along with an impedance of $R \approx 50 \Omega$, this yields a cut-off frequency $f_c = 1/(2\pi RC_{mutual})$ in the terahertz regime, which goes well beyond attainable frequencies for driven nanomechanical systems⁴. A simple analytical model reproduces the simulated behaviour. As the electric field lines in the inset of Fig. 1b show, the overall dominant field component in the vicinity of the resonator is parallel to the surface

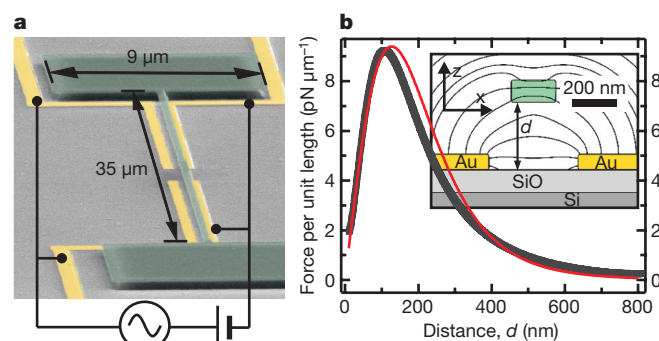


Figure 1 | Sample geometry and force acting on the nanomechanical resonator. **a**, Scanning electron micrograph of a representative device. The high-stress silicon nitride film (green) forms the suspended doubly clamped beam and its supports. The four nearby gold electrodes (yellow) are connected to both a d.c. and an r.f. voltage source used to polarize and resonantly excite the beam. **b**, Electrostatic force per unit length in the z direction, perpendicular to the sample plane, versus distance d from the electrodes for $V_{d.c.} = 2$ V simulated by a finite element calculation (black) and approximated by an analytical fit (red). In our experiments d is about 300 nm. The inset depicts a cross-section of the device and shows the electric field lines obtained by the simulation. We note that the field component E_z changes sign across the beam along the x direction, giving rise to a finite $\partial E_z / \partial x$, as in equation (1).

¹Fakultät für Physik and Center for NanoScience (CeNS), Ludwig-Maximilians-Universität, Geschwister-Scholl-Platz 1, 80539 München, Germany.

(x direction). Therefore, the induced charge distribution on the resonator can be approximated by a dipole oriented in the x direction proportional to the electric field component in this direction: $p_x = \chi E_x$, with susceptibility χ . The charging q_i of each electrode is described by a point charge. Neglecting the electrostatic contribution of the influenced charges, the z component of the resulting force F_z in this simple dipole approximation is proportional to the field gradient along the x direction:

$$F_z = p_x \frac{\partial E_z}{\partial x} \propto E_x E_z \quad (1)$$

$$\text{with } \mathbf{E}(\mathbf{r}) = \sum_{i=1,2} q_i \frac{\mathbf{r} - \mathbf{r}_i}{|\mathbf{r} - \mathbf{r}_i|^3}$$

Using the mutual distance of the electrodes $|\mathbf{r}_1 - \mathbf{r}_2|$ and the resonator susceptibility χ as fit parameters, the simulated results are well approximated (see red line in Fig. 1b). Neglecting small deformations of the resonant element by electrical forces, equation (1) predicts a quadratic dependence on electric field, just as in the case of capacitive actuation¹¹. Weakly modulating the applied bias voltage therefore gives rise to an oscillating force:

$$F[V_{d.c.} + V_{r.f.}] = c_1 (V_{d.c.} + V_{r.f.})^2 \approx c_1 V_{d.c.}^2 + 2c_1 V_{d.c.} V_{r.f.} \quad (2)$$

with c_1 a constant

Equation (2) shows that two independent parameters ensure optimized actuation: while $V_{r.f.}$ is employed to actuate the oscillatory motion of the resonator, the amplitude of $V_{d.c.}$ independently controls the strength of the polarization. This striking behaviour is a distinct feature of electrical realizations of dielectric force gradients. Optically generated gradient forces which have recently been reported as actuation for nanomechanical resonators¹⁸ do not incorporate this polarization tunability because both polarization and actuating force result from the same laser field. Unlike for the related concept of laser tweezers employing polarizing quasi-static electrical fields¹, the polarizing d.c. voltage allows efficient operation even in the case of a reduced susceptibility $\chi(\omega)$ in the frequency regime of resonator eigenmodes.

Our experiments are performed at room temperature in a vacuum of $P < 3 \times 10^{-3}$ mbar to exclude gas damping. Resonators with typical dimensions of $(30\text{--}40) \times 0.2 \times 0.1 \mu\text{m}^3$ (length \times width \times height) are fabricated from high-stress silicon nitride¹⁰ using standard lithographic methods. The drive electrodes are defined by lithographic post-processing on fully released beams, enabled by the strong tensile stress of 1.4 GPa of the silicon nitride film. Several resonators processed on different sample chips were investigated. The results shown in this work are representative and have been taken from three distinct resonators.

Using a standard fibre-based optical interferometer¹⁹, we detect the out-of-plane displacement of the resonator sensitively enough to resolve the Brownian motion of the resonator, as shown in Fig. 2a. The fundamental resonance is described by a harmonic differential equation, with effective mass m , spring constant k_0 , eigenfrequency $f_0 = \sqrt{k_0/m}/2\pi$, mechanical quality factor Q and external force F . For the investigated resonators, f_0 lies between 5 and 9 MHz, while Q ranges from 100,000 to 150,000, comparable to values reported elsewhere¹⁰. The frequency spectrum of the thermally driven system is Lorentzian. Its calculated amplitude²⁰ is used as a calibration to convert the measured optical signal into displacement. Figure 2b displays the driven resonator amplitude versus frequency along with a Lorentzian fit. The measured resonance amplitude (all indicated amplitudes are half-peak-to-peak amplitudes) for an actuation with $V_{d.c.} + V_{r.f.} = 1 \text{ V} \pm 0.2 \text{ mV}$ is about $\pm 0.8 \text{ nm}$. A simple model based on the simulated forces yields $\pm 0.3 \text{ nm}$ when assuming a dielectric constant of silicon nitride of 7 (the literature²¹ reports values between 6 and 9), which is in fair agreement. From the experimental data we estimate that a minimal actuation voltage $V_{r.f.} = \pm 5 \mu\text{V}$ is sufficient to drive more strongly than the Brownian motion for a bandwidth of 50 Hz. With the simulated value of $C_{\text{mutual}} \approx 1.5 \text{ fF}$ this translates into resonantly charging the electrodes by just 0.05 electrons, which

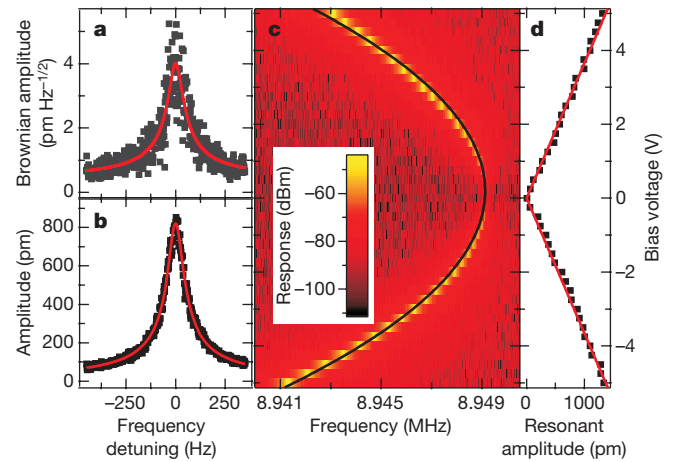


Figure 2 | Response of the dielectrically driven nanomechanical resonator.

a, Brownian motion at room temperature for $V_{d.c.} = 1 \text{ V}$ without r.f. excitation. **b**, Dielectrically driven oscillation with $V_{d.c.} + V_{r.f.} = 1 \text{ V} \pm 0.2 \text{ mV}$, corresponding to an r.f. power of -70 dBm . The data in **a** and **b** (dots) are well fitted by Lorentzians (red lines). The magnitude of the Brownian motion is used to convert the measured signal into the amplitude of the resonator displacement. **c** and **d**, Response of the resonator as a function of frequency and d.c. bias voltage at r.f. drive $V_{r.f.} = \pm 0.06 \text{ mV}$. In **c**, the power response is logarithmically colour-coded. The resonance frequency decreases quadratically with $V_{d.c.}$ (fit shown by the black line). The resonant amplitude of **c** is displayed as a function of the d.c. bias in **d**, reflecting the linear dependence of the resonator polarization on d.c. bias voltage (fit shown by the red line).

is below recently reported results⁹. In Fig. 2c individual power response traces are plotted as a function of frequency on a colour scale for a series of $V_{d.c.}$ and $V_{r.f.} = \pm 63 \mu\text{V}$. The corresponding resonant amplitude is depicted in Fig. 2d. It clearly scales linearly with the applied d.c. bias voltage, as expected from equation (2). The resonance frequency decreases quadratically with bias voltage (see fit indicated by solid black line in Fig. 2c). This can be readily understood from the force dependence on the distance d (see Fig. 1b). Expanding this dependence around the equilibrium position d_0 yields:

$$F[d_0 + \delta d] = F_0 + \frac{\partial F}{\partial d} \delta d + O(\delta d)^2 \quad (3)$$

The constant term F_0 leads to a new equilibrium position and can be ignored. However, the term linear in displacement (at the same time quadratic in applied voltage) acts as an additional spring constant on the resonator. It follows from Fig. 1b that this contribution is negative for the given $d \approx 300 \text{ nm}$. The resulting eigenfrequency f_0 therefore shifts in leading order with the observed quadratic voltage dependence:

$$\tilde{f}_0 = \frac{1}{2\pi} \sqrt{\frac{k_0 - c_2 V_{d.c.}^2}{m}} \approx f_0 \left(1 - \frac{c_2 V_{d.c.}^2}{2k_0} \right) \quad (4)$$

with c_2 a constant

Figure 3a exhibits a frequency tuning range of more than 100 kHz, corresponding to approximately 1,000 full width at half maximum (FWHM $\approx 100 \text{ Hz}$).

Subject to strong actuation, the resonator response enters the non-linear regime. This can be achieved for relatively small actuation powers, which do not give rise to a significant thermal heating of the sample (see Supplementary Information). Higher-order terms in displacement display similar tuning effects²², which will be presented elsewhere. The voltage tuning enables parametric excitation: a modulation of the resonance frequency at about $2f_0$ can give rise to instability and self-oscillation of the system even without the applied resonant force $F^{23,24}$. Figure 3b depicts the power response versus detection frequency f near f_0 and r.f. frequency modulation power leading to the modulation amplitude δf (see Fig. 3a). The characteristic Arnold

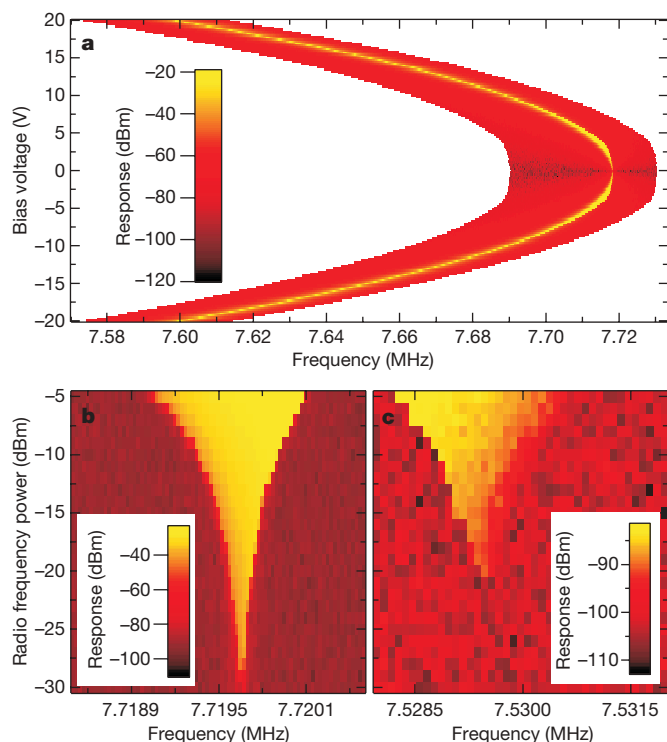


Figure 3 | Tuning and parametric transduction of the nanoelectromechanical resonator. **a**, Power response of the resonator at $V_{r.f.} = \pm 2$ mV sampled around the resonance. To minimize long-term drifts, traces are taken with increasing absolute value of d.c. bias reversing sign between consecutive traces (see Supplementary Information). **b** and **c**, Interferometric versus dielectric detection. **b**, Interferometrically measured power response subject to parametric actuation around $2\tilde{f}_0$ at $V_{d.c.} = 3$ V. The resonance frequency is modulated at $2f$ with the r.f. power plotted on the y axis, while the detection frequency f is plotted along the x axis. **c**, Power response of a parametrically excited resonator using dielectric detection at $V_{d.c.} = 20$ V. As in **b**, the resonator was driven by a frequency modulation at twice the detection frequency as a function of modulation power and detection frequency. The response reproduces the interferometrically measured data from **b**, even though a sample with a different electrical environment was used.

tongue⁷ indicates the region of instability and self-oscillation as experimental evidence of parametric actuation. In particular, when the resonance frequency \tilde{f}_0 is modulated at exactly twice its value with $\delta f(t) = \delta f \times \cos(2(2\pi\tilde{f}_0)t)$, theory predicts the transition to occur when $\delta f > \tilde{f}_0/Q$. For the case shown in Fig. 3a, the transition is expected for a driving power of -25 dBm, which is in good agreement with the data. However, we note that there is some ambiguity in defining the onset of spontaneous oscillation¹¹.

Reversing the actuation principle, we can also electrically detect the motion of the resonator locally. Therefore, on a different sample, a second pair of biased electrodes is introduced, which had previously been shunted with the driving electrodes (see Fig. 1a). The oscillating motion of the polarized resonator modulates the mutual capacitance of these electrodes, thereby creating an electrical signal. To avoid crosstalk from a resonant drive signal, the beam was parametrically excited around $2\tilde{f}_0$, as discussed above. The dielectric detection scheme uses an impedance converter near the sample and is demonstrated in Fig. 3c. To estimate the achieved sensitivity, the response amplitudes of Fig. 3b and c are compared when the resonator is driven 10 dB beyond the onset of spontaneous oscillation. An amplitude of ± 10 nm results in an electrical signal power of approximately -80 dBm. As the noise level is about -100 dBm when measuring at 50 Hz bandwidth, the sensitivity is approximately 20 pm $\text{Hz}^{-1/2}$ for the unoptimized device. An estimate of the limits of this detection scheme using a more advanced set-up can be found in the Supplementary Information.

Although other electrical displacement sensors have obtained higher sensitivities^{13,25,26}, the integration with a highly efficient, material-independent drive makes our dielectric scheme an interesting candidate for nanomechanical transduction.

In conclusion, by taking advantage of dielectric gradient forces, we realize and quantitatively validate a new and widely applicable actuation and readout scheme for nanoelectromechanical systems. It is on-chip and scalable to large arrays, broadband potentially beyond the gigahertz regime, and imposes no restrictions on the choice of resonator material. It thus enables the optimization of mechanical quality factors of the resonator without being bound by specific material requirements. The sensitivity of mechanical sensors scales with the quality factor³, so we anticipate the scheme to be of interest in the fast-developing field of sensing^{5,6}. Capable of locally addressing individual resonators, it is particularly relevant for bio-sensing, where large arrays of individually addressable resonators are desirable to analyse multiple constituents. Because the driven mechanical element can be fabricated separately from the actuating capacitor, it will also permit bottom-up fabrication²⁷. Using this actuation scheme we demonstrate strong electrical field-effect tuning of both the resonance amplitude and frequency. This facilitates parametric excitation of the resonator at $2f$, thus allowing decoupled detection of its oscillation at f . The large frequency tuning range can, for example, be used for in-situ tuning of several mechanical elements into resonance²⁸ or coupling to external elements²⁹. Moreover, the combination of parametric excitation and (even weak) signal extraction enables digital signal processing based on mechanical elements, as has recently been demonstrated for microelectromechanical resonators¹². With additional tuning, an almost ideal electromechanical bandpass filter has been suggested⁷. Whereas we already achieve highly efficient actuation, as reflected by the low driving voltages in the micro-volt regime, the sensitivity of our detection scheme can be significantly enhanced by, for example, using a microwave tank circuit²⁶. This also opens a pathway to cooling the mechanical eigenmodes^{26,30}.

Received 31 October 2008; accepted 23 February 2009.

- Ashkin, A. Optical trapping and manipulation of neutral particles using lasers. *Proc. Natl Acad. Sci. USA* **94**, 4853–4860 (1997).
- Jones, T. B. *Electromechanics of Particles* (Cambridge Univ. Press, 1995).
- Ekinci, K. L. & Roukes, M. L. Nanoelectromechanical systems. *Rev. Sci. Instrum.* **76**, 061101 (2005).
- Huang, X. M., Zorman, C. A., Mehregany, M. & Roukes, M. L. Nanoelectromechanical systems: Nanodevice motion at microwave frequencies. *Nature* **421**, 496 (2003).
- Li, M., Tang, H. X. & Roukes, M. L. Ultra-sensitive NEMS-based cantilevers for sensing, scanned probe and very high-frequency applications. *Nature Nanotechnol.* **2**, 114–120 (2007).
- Jensen, K., Kim, K. & Zettl, A. An atomic-resolution nanomechanical mass sensor. *Nature Nanotechnol.* **3**, 533–537 (2008).
- Rhoads, J. F., Shaw, S. W., Turner, K. L. & Baskaran, R. Tunable microelectromechanical filters that exploit parametric resonance. *J. Vib. Acoust.* **120**, 423–430 (2005).
- Ekinci, K. L. Electromechanical transducers at the nanoscale: actuation and sensing of motion in nanoelectromechanical systems (NEMS). *Small* **1**, 786–797 (2005).
- Masmanidis, S. C. *et al.* Multifunctional nanomechanical systems via tunably coupled piezoelectric actuation. *Science* **317**, 780–783 (2007).
- Verbridge, S. S., Parpia, J. M., Reichenbach, R. B., Bellan, L. M. & Craighead, H. G. High quality factor resonance at room temperature with nanostrings under high tensile stress. *J. Appl. Phys.* **99**, 124304 (2006).
- Rugar, D. & Gruetter, P. Mechanical parametric amplification and thermomechanical noise squeezing. *Phys. Rev. Lett.* **67**, 699–702 (1991).
- Mahboob, I. & Yamaguchi, H. Bit storage and bit flip operations in an electromechanical oscillator. *Nature Nanotechnol.* **3**, 275–279 (2008).
- Knobel, R. G. & Cleland, A. N. Nanometre-scale displacement sensing using a single electron transistor. *Nature* **424**, 291–293 (2003).
- Bargatin, I., Kozinsky, I. & Roukes, M. L. Efficient electrothermal actuation of multiple modes of high-frequency nanoelectromechanical resonators. *Appl. Phys. Lett.* **90**, 093116 (2007).
- Tang, H. X., Huang, X. M. H., Roukes, M. L., Bichler, M. & Wegscheider, W. Two-dimensional electron-gas actuation and transduction for GaAs nanoelectromechanical systems. *Appl. Phys. Lett.* **81**, 3879–3881 (2002).
- Sekaric, L., Carr, D. W., Evoy, S., Parpia, J. M. & Craighead, H. G. Nanomechanical resonant structures in silicon nitride: fabrication, operation and dissipation issues. *Sens. Actuat. A* **101**, 215–219 (2002).

17. Sampathkumar, A., Murray, T. W. & Ekinci, K. L. Photothermal operation of high frequency nanoelectromechanical systems. *Appl. Phys. Lett.* **88**, 223104 (2006).
18. Li, M. *et al.* Harnessing optical forces in integrated photonic circuits. *Nature* **456**, 480–484 (2008).
19. Azak, N. O. *et al.* Nanomechanical displacement detection using fiber-optic interferometry. *Appl. Phys. Lett.* **91**, 093112 (2007).
20. Gillespie, D. T. The mathematics of Brownian motion and Johnson noise. *Am. J. Phys.* **64**, 225–240 (1996).
21. Gad-el-Hak, M. *The MEMS Handbook* 15–157 (CRC Press, 2001).
22. Zhang, W., Baskaran, R. & Turner, K. Tuning the dynamic behavior of parametric resonance in a micromechanical oscillator. *Appl. Phys. Lett.* **82**, 130–132 (2003).
23. Nayfeh, A. H. & Mook, D. T. *Nonlinear Oscillations* Ch. 5 (Wiley, 1995).
24. Lifshitz, R. & Cross, M. C. Response of parametrically driven nonlinear coupled oscillators with application to micromechanical and nanomechanical resonator arrays. *Phys. Rev. B* **67**, 134302 (2003).
25. LaHaye, M. D., Buu, O., Camarota, B. & Schwab, K. C. Approaching the quantum limit of a nanomechanical resonator. *Science* **304**, 74–77 (2004).
26. Regal, C. A., Teufel, J. D. & Lehnert, K. W. Measuring nanomechanical motion with a microwave cavity interferometer. *Nature Phys.* **4**, 555–560 (2008).
27. Li, M. *et al.* Bottom-up assembly of large-area nanowire resonator arrays. *Nature Nanotechnol.* **3**, 88–92 (2008).
28. Spletzer, M., Raman, A., Wu, A. Q., Xu, X. & Reifenberger, R. Ultrasensitive mass sensing using mode localization in coupled microcantilevers. *Appl. Phys. Lett.* **88**, 254102 (2006).
29. Cleland, A. N. & Geller, M. R. Superconducting qubit storage and entanglement with nanomechanical resonators. *Phys. Rev. Lett.* **93**, 070501 (2004).
30. Brown, K. R. *et al.* Passive cooling of a micromechanical oscillator with a resonant electric circuit. *Phys. Rev. Lett.* **99**, 137205 (2007).

Supplementary Information is linked to the online version of the paper at www.nature.com/nature.

Acknowledgements Financial support by the Deutsche Forschungsgemeinschaft via project Ko 416/18, the German Excellence Initiative via the Nanosystems Initiative Munich (NIM) and LMUexcellent as well as LMUinnovativ is gratefully acknowledged.

Author Contributions The experiment was performed and analysed by Q.P.U.; the results were discussed and the manuscript was written by all authors.

Author Information Reprints and permissions information is available at www.nature.com/reprints. The authors declare competing financial interests: details accompany the full-text HTML version of the paper at www.nature.com/nature. Correspondence and requests for materials should be addressed to J.P.K. (kotthaus@lmu.de).

Coherent detection of nonlinear nanomechanical motion using a stroboscopic downconversion technique

Quirin P. Unterreithmeier,^{a)} Stephan Manus, and Jörg P. Kotthaus
*Fakultät für Physik and Center for NanoScience (CeNS), Ludwig-Maximilians-Universität,
 Geschwister-Scholl-Platz 1, München 80539, Germany*

(Received 23 January 2009; accepted 26 May 2009; published online 30 June 2009)

A method is presented that overcomes bandwidth limitations arising in a fiber-optic setup transducing mechanical motion. The reflected light from a sample incorporating a nanomechanical resonator is analyzed. Modulating the incoming laser intensity at a suitably chosen frequency, the mechanically induced oscillation of the reflected light is coherently downconverted to a frequency within the detection bandwidth. Additionally, based on the mechanical nonlinear response, the optical signal can be quantitatively converted into displacement, yielding a sensitivity of $7 \text{ pm}/\sqrt{\text{Hz}}$ at optical power levels of $20 \text{ }\mu\text{W}$. We detect and image mechanical modes up to the seventh harmonic of the fundamental mode at 7.7 MHz. © 2009 American Institute of Physics.
 [DOI: 10.1063/1.3155164]

The resonant motion of micro- and nanoelectromechanical systems is increasingly investigated. Their small masses, high quality (Q) factors, and high integrability make them equally interesting for fundamental research as well as applications in sensing and signal processing.^{1,2} Optical setups are among the most sensitive ones for the detection of the mechanical motion. With decreasing dimensions and increasing resonance frequencies of the mechanical systems the detection of the motion requires increasingly complex setups.³ In particular, sensitive optomechanical transduction typically employs reference beams³ and/or optical cavities.⁴ These approaches equally require very stable lasers and optical paths. We employ a simpler fiber-optical setup, as sketched in Fig. 1 and described, e. g., in Ref. 5.

In this setup the sample is illuminated with light coming out of a bare close-by glass fiber and the scattered light is collected with the same fiber without additional optical components. Our investigated nanomechanical system consists of a stretched SiN wire⁶ of dimensions $35 \text{ }\mu\text{m} \times 250 \text{ nm} \times 100 \text{ nm}$, length, width, and height, respectively. The mechanical actuation is induced by dielectric forces caused by an essentially spatially inhomogeneous electrical field generated by suitably biased electrodes close to the resonator as discussed elsewhere.⁷ Since the motion of the resonator only weakly modulates the reflected laser intensity, significant amplification of the detected signal oscillating at radio frequency of the mechanical resonances is required. Typically, amplifiers exhibit a trade-off concerning bandwidth, amplification factor, and amplifier noise. The photodiode with an integrated preamplifier (Thorlabs PDA55) used for this work has variable gain and bandwidth (maximum of 10 MHz). The datasheet shows that these quantities are approximately inversely proportional whereas the amplifier noise is rather constant with varying bandwidth. In order to exceed the amplifier constraints, we introduce a modulation of our laser intensity at frequency f_{RF} , as sketched in Fig. 1. Here, a square-wave modulation of the laser intensity is implemented with a homemade switching circuit. We actuate the mechanical resonator with frequency $f_{\text{RF}} - f_{\text{LO}}$. This driving

signal is coherently generated by mixing the signal that modulates the laser with the signal of a local oscillator, operating at fixed frequency $f_{\text{LO}} = 0.9 \text{ MHz}$ employing a homemade single sideband modulator. Consequently, the light reflected from the driven mechanical resonator contains frequency components at the sum ($2f_{\text{RF}} - f_{\text{LO}}$) and difference (f_{LO}) frequency. The sum frequency typically exceeds the bandwidth of our detector and is suppressed. However, the difference frequency is coherently detected using a network analyzer. Sweeping f_{RF} while retaining $f_{\text{LO}} = 0.9 \text{ MHz}$ yields the frequency-dependent response of the mechanical resonator at $f_{\text{RF}} - f_{\text{LO}}$. In the following all experiments are performed at room temperature and a pressure below $5 \times 10^{-4} \text{ mbar}$.

A typical response curve can be seen in Fig. 2(a); fitting a Lorentzian line shape yields the mechanical resonance frequency and quality (Q) factor. With the stroboscopic detection scheme, we are able to investigate also harmonic modes

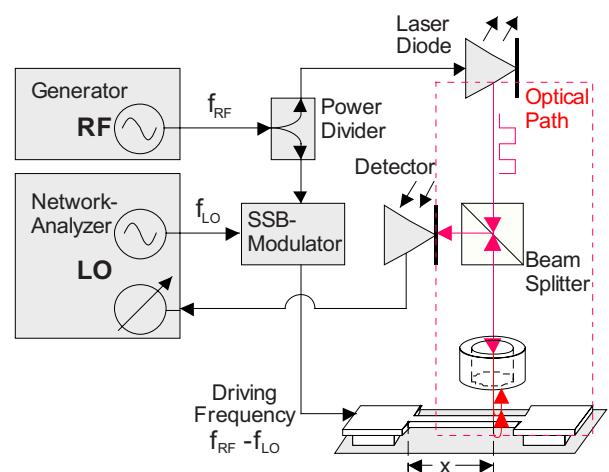


FIG. 1. (Color online) Schematic transduction setup; the electronic path is plotted in black; the area surrounded by the dashed rectangle depicts the optical path; arrows indicate the direction of signal propagation. The sample containing a string as nanomechanical resonator is mounted in vacuum just below the end of the optical fiber as indicated. As the sample is actuated at $f_{\text{RF}} - f_{\text{LO}}$ and the illuminating laser intensity is modulated at f_{RF} a coherent, low-frequency beat at f_{LO} is created on the photodetector.

^{a)}Electronic mail: quirin.unterreithmeier@physik.uni-muenchen.de.

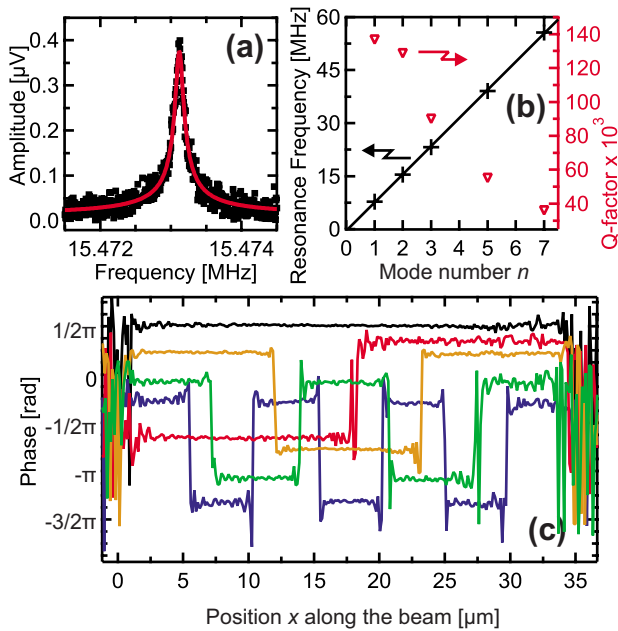


FIG. 2. (Color online) (a) Mechanical response and Lorentzian fit of a nanomechanical stretched SiN wire with dimensions $35 \mu\text{m} \times 250 \text{ nm} \times 100 \text{ nm}$ length, width, and height, respectively, driven around the second harmonic mode. (b) Resonance frequencies and quality factors of the fundamental mode and all observed harmonics are plotted vs mode number n , reflecting the number of antinodes along the length of the wire. To emphasize the scaling behavior of the frequencies a linear fit is shown. (c) Spatial distribution of the phase of the observed mechanical modes as measured with the detection fiber moved by position x along the wire (see Fig. 1). For clarity the curves are offset in phase with respect to each other.

of our mechanical resonator at frequencies beyond the bandwidth of our photodetector. The ability to record several modes has been demonstrated to be advantageous for sensing.⁸ In Fig. 2(b), resonance frequencies and quality factors are displayed versus the respective mode number n corresponding to the number of antinodes along the length of the resonator. In contrast to a doubly clamped beam,⁹ the frequencies can be clearly seen to scale linearly with mode number. As the implementation of the employed actuation scheme is spatially symmetric, we are not able to excite all antisymmetric, even n , modes. From the resulting spectrum, one can deduce that the model of a string can be safely employed to describe the resonant motion. The relatively large Q values are found to decrease with increasing frequency, a phenomenon generally observed⁶ but still not quantitatively understood. In Fig. 2(c), we scan the detection fiber along the wire and plot the locally obtained phase of the oscillation; a method for convincingly identifying a given mode. It is noteworthy that techniques relying on modulation of the driving amplitude are not able to retrieve this information, see for example Ref. 10. Using a direct detection scheme of the mechanical resonance under cw illumination, we obtain a somewhat higher displacement resolution (yet bandwidth limited) and are able to measure the Brownian motion of the fundamental mode at 300 K. This enables us to quantitatively convert the measured signal into displacement.¹¹

In the following, we describe how the nonlinear behavior of the resonator can be employed to transfer this displacement calibration to the higher harmonics. Related experiments have been reported in Ref. 12. At large driving amplitudes, the restoring force $F(z)$ exhibits nonlinear terms

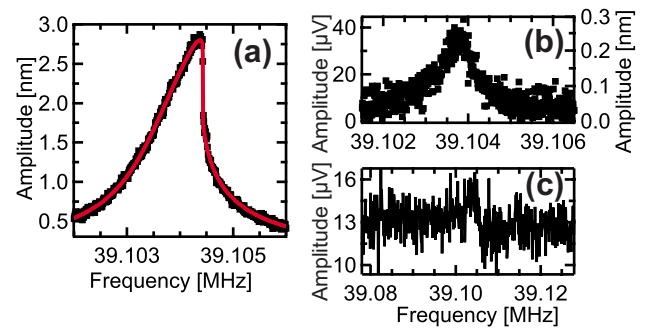


FIG. 3. (Color online) (a) Nonlinear response of the fifth harmonic mode; experimental data (black) and theoretical fit (red). The fit is employed to convert the detected signal into mechanical displacement. [(b) and (c)] Comparison of signal transduction using stroboscope (a) and (b) and cw illumination (c) measuring with 50 Hz bandwidth. Note that the driving amplitude in (a) and (c) are identical; therefore the noise floor in (c) can be estimated to be about 2 nm and is substantially larger than the one of about 50 pm (b) achieved in the stroboscopic detection scheme.

in displacement z . For convenience we write $F(z) = k \cdot z + m_{\text{eff}} \alpha_3 \cdot z^3$. Here m_{eff} , $k = m_{\text{eff}} (2\pi f)^2$, and $m_{\text{eff}} \alpha_3$ denote the effective mass, linear spring constant, and cubic contribution, respectively, of the mechanical mode considered. For the case of a string, the spatial modes are described by a cosine, thereby a simple calculation yields the restoring force up to cubic order. We define L as half the wavelength of the resonant mode, which for the fundamental mode equals the length of the string l and for the higher modes $L = l/n$ with $n = 2, 3, \dots$. With E , σ , and ρ being Young's modulus, tensile stress, and density of the resonator material, we obtain

$$\frac{F(z)}{m_{\text{eff}}} = \frac{\pi^2 \sigma}{L^2 \rho} z + \frac{(E + 3/2\sigma) \pi^4}{4L^4 \rho} z^3. \quad (1)$$

We note that this result reflects the well-known fact that a string doubles its resonance frequency when halving its length. Assuming a density of $\rho = 3000 \text{ kg/m}^3$,¹³ the measured frequency of the fundamental mode translates into a tensile stress of $\sigma = 830 \text{ MPa}$, significantly less than the given specifications of the unprocessed SiN films (1400 MPa). For the amplitude conversion we note that the nonlinear term scales with the length as $\alpha_3 \sim L^{-4}$. The differential equation employing the nonlinear restoring force, the so-called Duffing equation, can be solved in the case of a steady-state oscillation, yielding a frequency-dependent amplitude $|z| = |z|(f)$. The explicit calculations are not presented here and can be found for example in Ref. 14. With increasing actuation amplitude, the initial Lorentzian line shape begins to bend over to one side and eventually becomes bistable, a nonlinear phenomenon often seen in nanomechanics.¹⁵ We fit the measured resonance curves near the onset of bistability with the solution of the Duffing equation. For the fundamental mode we thereby derive an absolute value for α_3 . With the given geometry this translates into a Young's Modulus of $E = 100 \text{ GPa}$, reduced with respect to the literature value of spatially homogeneous SiN films around 300 GPa.¹³ Applying the obtained values, continuum mechanics predicts a flexural contribution to the restoring force less than 2%.⁶ To extend the calibration to the case of the harmonics, the values for α_3 are rescaled to obey $1/L^4$ scaling with respect to the fundamental mode [see Eq. (1)]. Thus a scaling factor is obtained to convert the measured detector signal into displacement. Figure 3(a) shows such

rescaled measurement and the corresponding nonlinear fit. The fitting procedure proves to be surprisingly stable, even in the case that none of the fitting parameters, such as f_0 , Q are held fixed. In contrast, if we directly employed literature values for E , appropriate for our wafer material, the conversion would yield amplitudes that are approximately half as large.

Using above calibration, we are able to determine the sensitivity of our setup. Figure 3(b) shows a weakly driven resonance detected in the stroboscopic mode, from which one can deduce a noise floor of about 50 pm measured at a bandwidth of 50 Hz. This corresponds to a sensitivity of $7 \text{ pm}/\sqrt{\text{Hz}}$ at an average incoming laser power of $20 \text{ } \mu\text{W}$. The values obtained for the other modes deviate slightly from this value; we attribute this to the modulation amplitude of our laser that is measured to be not completely constant over the whole range of modulation frequencies (data not shown). Normalized to the laser intensity, these sensitivity values are comparable to those reported in Ref. 5 based on cw illumination. To quantify the signal-enhancement caused by the stroboscopic downconversion technique, Fig. 3(c) shows the same resonance as Fig. 3(a) employing cw illumination. The obtained maximum in the spectrum therefore corresponds to an amplitude of 3 nm, whereas the noise floor translates into an amplitude of at least 2 nm rms, about a factor of 50 worse than in Fig. 3(b).

Assuming that the modulation of the illuminating laser at higher frequencies does not increase the noise of the optical signal detected at frequency f_{LO} , the detected signal decreases only in proportion to the mechanical displacement of the string and the sensitivity is expected to be independent of frequency.

Other stroboscopic techniques have been reported that do not require additional optical components: Ref. 16 employs short light pulses freezing the mechanical motion that produce phase-shifted spatial images and typically achieves displacement resolutions not exceeding nanometer. Another recently reported time-domain technique,¹⁷ employing local interferometric effects, is equally based on short probing and excitation pulses. There, displacement resolutions in the picometer regime are observed up to resonator frequencies in the GHz regime. However, as pulsed excitation is applied, this technique imposes challenges when studying steady-state phenomena.

In conclusion we demonstrate a simple stroboscopic technique to coherently detect nanomechanical motion, separating the detection frequency f_{LO} from the frequency of mechanical motion $f_{RF}-f_{LO}$. This allows to far exceed bandwidth limitations imposed by sensitive detection electronics. Based on this approach sensitivities of the mechanical displacement down to $7 \text{ pm}/\sqrt{\text{Hz}}$ are demonstrated at an average incoming laser power of only $20 \text{ } \mu\text{W}$ and resonant motion between 7 and 55 MHz. It is expected that this technique facilitates detection ranging in the GHz regime. Nonlinear characteristics of the mechanical resonator are employed to quantitatively convert the measured signal into displacement.

Financial support by the Deutsche Forschungsgemeinschaft via Project Ko 416/18-1 as well as the German Excellence Initiative via the Nanosystems Initiative Munich (NIM) and LMUexcellent is gratefully acknowledged.

¹H. G. Craighead, *Science* **290**, 1532 (2000).

²K. L. Ekinci and M. L. Roukes, *Rev. Sci. Instrum.* **76**, 061101 (2005).

³H. Martinussen, A. Aksnes, and H. E. Engan, *Opt. Express* **15**, 11370 (2007).

⁴Y. Hadjar, P. F. Cohadon, C. G. Aminoff, M. Pinard, and A. Heidmann, *Europhys. Lett.* **47**, 545 (1999).

⁵N. O. Azak, M. Y. Shagam, D. M. Karabacak, K. L. Ekinci, D. H. Kim, and D. Y. Jang, *Appl. Phys. Lett.* **91**, 093112 (2007).

⁶S. S. Verbridge, J. M. Parpia, R. B. Reichenbach, L. M. Bellan, and H. G. Craighead, *J. Appl. Phys.* **99**, 124304 (2006).

⁷Q. P. Unterreithmeier, E. M. Weig, and J. P. Kotthaus, *Nature (London)* **458**, 1001 (2009).

⁸S. Dohn, W. Svendsen, A. Boisen, and O. Hansen, *Rev. Sci. Instrum.* **78**, 103303 (2007).

⁹I. Kozinsky, H. W. Ch. Postma, I. Bargatin, and M. L. Roukes, *Appl. Phys. Lett.* **88**, 253101 (2006).

¹⁰A. San Paulo, J. P. Black, R. M. White, and J. Bokor, *Appl. Phys. Lett.* **91**, 053116 (2007).

¹¹D. T. Gillespie, *Am. J. Phys.* **64**, 225 (1996).

¹²D. W. Carr, S. Evoy, L. Sekaric, H. G. Craighead, and J. M. Parpia, *Appl. Phys. Lett.* **75**, 920 (1999).

¹³M. Gad-el-Hak, *The MEMS Handbook* (CRC, New York, 2001).

¹⁴A. H. Nayfeh and D. T. Mook, *Nonlinear Oscillations* (Wiley, New York, 1995).

¹⁵I. Kozinsky, H. W. Ch. Postma, O. Kogan, A. Husain, and M. L. Roukes, *Phys. Rev. Lett.* **99**, 207201 (2007).

¹⁶D. Hessman, M. Lexholm, K. A. Dick, S. Ghatnekar-Nilsson, and L. Samuelson, *Small* **3**, 1699 (2007).

¹⁷N. Liu, F. Giesen, M. Belov, J. Losby, J. Moroz, A. E. Fraser, G. McKinnon, T. J. Clement, V. Sauer, W. K. Hiebert, and M. R. Freeman, *Nat. Nanotechnol.* **3**, 715 (2008).

Near-field cavity optomechanics with nanomechanical oscillators

G. Anetsberger¹, O. Arcizet¹, Q. P. Unterreithmeier², R. Rivière¹, A. Schliesser¹, E. M. Weig², J. P. Kotthaus² and T. J. Kippenberg^{1,3*}

Cavity-enhanced radiation-pressure coupling between optical and mechanical degrees of freedom allows quantum-limited position measurements and gives rise to dynamical backaction, enabling amplification and cooling of mechanical motion. Here, we demonstrate purely dispersive coupling of high-Q nanomechanical oscillators to an ultrahigh-finesse optical microresonator via its evanescent field, extending cavity optomechanics to nanomechanical oscillators. Dynamical backaction mediated by the optical dipole force is observed, leading to laser-like coherent nanomechanical oscillations solely due to radiation pressure. Moreover, sub-fm Hz^{-1/2} displacement sensitivity is achieved, with a measurement imprecision equal to the standard quantum limit (SQL), which coincides with the nanomechanical oscillator's zero-point fluctuations. The achievement of an imprecision at the SQL and radiation-pressure dynamical backaction for nanomechanical oscillators may have implications not only for detecting quantum phenomena in mechanical systems, but also for a variety of other precision experiments. Owing to the flexibility of the near-field coupling platform, it can be readily extended to a diverse set of nanomechanical oscillators. In addition, the approach provides a route to experiments where radiation-pressure quantum backaction dominates at room temperature, enabling ponderomotive squeezing or quantum non-demolition measurements.

Nanomechanical oscillators^{1,2} possess wide-ranging applications in both fundamental and applied sciences. Owing to their small mass, they are ideal candidates for probing quantum limits of mechanical motion in an experimental setting. Moreover, they are the basis of various precision measurements^{3–5}. Significant attention has been devoted to developing sensitive read-out techniques for nanomechanical motion over the past decade. A natural scale for comparing the performance achieved with systems of different size and mass is given by the variance of the mechanical oscillators' zero-point motion $\langle x(t)^2 \rangle_{zp} = \hbar/(2m\Omega_m)$ (\hbar : reduced Planck constant; m , $\Omega_m/2\pi$, Q : mass, resonance frequency, quality factor of the oscillator). In Fourier space, the zero-point motion can be described by a corresponding single-sided spectral density $S_{xx}[\Omega]$, which at the mechanical oscillator's resonance is given by $S_{xx}[\Omega_m] = 2\hbar Q/m\Omega_m^2$ and coincides with the SQL of continuous position measurement^{6–9}. So far, the most sensitive transducers for nanomechanical motion have been based on electron flow using a single-electron transistor¹⁰ or atomic point contact¹¹ coupled to a nanomechanical string in a cryogenic environment and have achieved a position imprecision of order 10^{-15} m Hz^{-1/2}. An imprecision at the level of the SQL, however, has not yet been achieved. In contrast, parametric motion transducers based on photons in a cavity—which are the basis for laser gravitational wave interferometers—provide quantum-limited measurement imprecision exceeding 10^{-18} m Hz^{-1/2} (refs 12, 13) being at or even below¹⁴ the zero-point fluctuations of the respective mechanical oscillator but are typically orders of magnitude less sensitive when applied to less massive, nanomechanical oscillators owing to the optical diffraction limit¹⁵. Moreover, cavity-optomechanical coupling of mechanical oscillators allows the exploitation of radiation-pressure dynamical backaction^{16,17} that is associated with the momentum

transfer from the photons involved in the measurement to the probed object and provides a mechanism for cooling^{18–20} or coherent amplification²¹ of mechanical motion. As such, an ideal platform would combine the quantum-limited detection and control afforded by cavity-optomechanical coupling with nanoscale mechanical oscillators which, owing to their small masses, provide large zero-point motion and high force sensitivity. Such an approach may therefore have promising implications for probing quantum phenomena of mechanical systems²² and equally in precision experiments, such as mass spectroscopy³, charge sensing⁴ and single-spin detection⁵ that are based on ultra-sensitive nanomechanical oscillators.

Efficient optomechanical interaction with nanomechanical oscillators requires avoiding introducing losses to the high-finesse optical cavity by the nanomechanical object, while maintaining large optomechanical coupling and mitigating thermal effects. Here, we demonstrate this combination, by evanescently coupling high-Q nanomechanical oscillators to the tightly confined optical field of an ultrahigh-finesse toroidal silica microresonator. Purely dispersive radiation-pressure coupling to the nanomechanical strings is observed and allows sub-fm Hz^{-1/2} displacement imprecision (at room temperature), equal to the SQL, which previously has not been possible^{10,11,23–25}. In contrast to the recently developed optomechanical zipper cavities²⁵, which also operate at the nanoscale, the reported near-field approach moreover decouples optical and mechanical degrees of freedom and thus provides a versatile platform to which diverse nanoscale oscillators, such as nanowires²⁶, graphene sheets²⁷ or carbon nanotubes, can be tunably coupled, extending cavity optomechanics¹⁷ into the realm of nanomechanical oscillators. In particular, it enables simultaneously high mechanical and optical Q, giving access to the

¹Max-Planck-Institut für Quantenoptik, Hans-Kopfermann-Str. 1, 85748 Garching, Germany, ²Fakultät für Physik and Center for NanoScience (CeNS), Ludwig-Maximilians-Universität (LMU), Geschwister-Scholl-Platz 1, 80539 München, Germany, ³Ecole Polytechnique Fédérale de Lausanne, EPFL, 1015 Lausanne, Switzerland. *e-mail: tobias.kippenberg@epfl.ch.

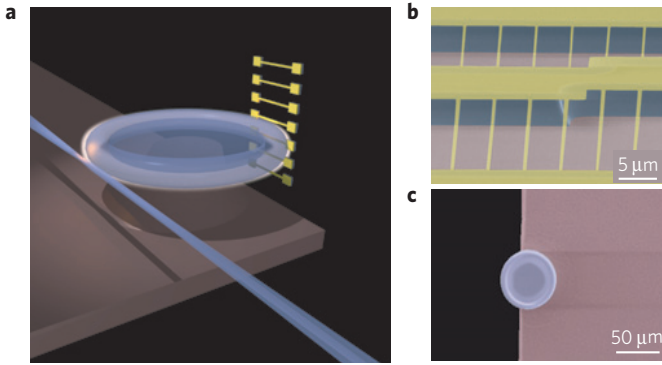


Figure 1 | Evanescent coupling of nanomechanical oscillators to an optical microresonator. **a**, Schematic of the experiment, showing a tapered-fibre-interfaced optical microresonator dispersively coupled to an array of nanomechanical oscillators. **b**, Scanning electron micrograph (false colour) of an array of doubly clamped SiN nanostring oscillators with dimensions $110 \text{ nm} \times (300\text{--}500) \text{ nm} \times (15\text{--}40) \mu\text{m}$. **c**, Scanning electron micrograph (false colour) of a toroid silica microcavity acting as an optomechanical near-field sensor.

resolved-sideband regime^{14,28,29}. By detuned excitation, dynamical backaction mediated by the optical dipole force is demonstrated, which leads to radiation-pressure-induced coherent oscillations of the nanomechanical oscillator, whereas thermal effects are negligible. Equally important, the combination of picogram and high-quality-factor nanostrings³⁰ with an ultrahigh-optical-finesse microresonator provides a route to the remarkable regime where radiation-pressure quantum backaction is the dominant force noise on the mechanical oscillator even at room temperature and might thus allow quantum optomechanical experiments such as ponderomotive squeezing³¹, quantum non-demolition (QND) measurements of photons^{32,33} or optomechanical entanglement³⁴ at ambient temperature.

Figure 1a shows a schematic of the experimental setup. We use an array of nanomechanical oscillators in the form of high-Q, tensile stressed and doubly clamped SiN strings^{15,30} such as shown in Fig. 1b. The strings have typical dimensions of $110 \text{ nm} \times (300\text{--}800) \text{ nm} \times (15\text{--}40) \mu\text{m}$, effective masses of $m_{\text{eff}} = 0.9\text{--}5 \text{ pg}$ and fundamental resonance frequencies $\Omega_{\text{m}}/2\pi = 6.5\text{--}16 \text{ MHz}$ with mechanical quality factors of $Q = 10^4\text{--}10^5$ (see Supplementary Information). Following a special fabrication process (see Supplementary Information) indeed allows using the tightly confined optical modes of toroid silica microcavities as near-field probes (see Fig. 1c) that interact with the nanomechanical oscillator through their evanescent field decaying on a length scale of $\alpha^{-1} \approx (\lambda/2\pi)/\sqrt{n^2 - 1}$ (that is, approximately 238 nm for the refractive index of silica $n = 1.44$ and a vacuum wavelength of $\lambda \approx 1,550 \text{ nm}$ used throughout this work).

Optomechanical coupling rate

First, we study the strength of the optomechanical coupling of the nanomechanical oscillators to the optical mode of a $58\text{-}\mu\text{m}$ -diameter microcavity (showing an unloaded optical linewidth of 4.9 MHz , that is, a finesse of $\mathcal{F} = 230,000$). The presence of a dielectric oscillator in the evanescent cavity field, at a distance x_0 to the microresonator surface, can in principle give rise to both a reactive and dispersive contribution to the optical-cavity response³⁵. The former would be characterized by increased cavity losses owing to scattering or absorption, given by a position-dependent cavity linewidth $\kappa(x_0)/2\pi$. The latter can be described by an optical-frequency shift $\Delta\omega_0(x_0)/2\pi = (\omega_0(x_0) - \omega_0)/2\pi$ caused by the increased effective refractive index sampled by the evanescent fraction of the mode (ω_0 denotes the unperturbed cavity frequency

with the nanomechanical oscillator being removed). Using energy considerations the (small) shift can be approximated by:

$$\Delta\omega_0(x_0) = -\frac{\omega_0}{2} \frac{V_{\text{nano}}}{V_{\text{cav}}} (n_{\text{nano}}^2 - 1) \xi^2 e^{-2\alpha x_0} \quad (1)$$

where V_{nano} is the volume of the nanomechanical oscillator (refractive index n_{nano}) sampled by the microcavity with mode volume V_{cav} . The magnitude of the cavity field at the toroid/vacuum interface divided by the maximum electric field inside the cavity is denoted by ξ (see Supplementary Information for a more detailed analysis). To probe this static interaction, we position the nanomechanical strings tangentially to the optical whispering-gallery mode trajectory and vary their distance (see Fig. 2a, inset) to the cavity using piezoelectric positioners. Note that all experiments are carried out in this horizontal configuration of the nanostrings as well as in vacuum with a pressure $< 10^{-4}$ mbar unless otherwise specified. As shown in Fig. 2a, the interaction with a nanomechanical string ($110 \text{ nm} \times 800 \text{ nm} \times 25 \mu\text{m}$) induces the expected optical frequency shift that exponentially increases as the distance x_0 is decreased and reaches the gigahertz range. The measured decay length of 110 nm is in good quantitative agreement with the value $1/(2\alpha)$ expected from equation (1). Importantly, we do not measure any degradation of the optical linewidth (see Fig. 2a) even for the strongest coupling. Our measurement accuracy of changes in the cavity linewidth $\Delta\kappa/2\pi < 0.5 \text{ MHz}$ allows an upper bound of 0.5 ppm equivalent optical loss induced by the SiN nanomechanical oscillator to be inferred. Thus, the optomechanical coupling is purely dispersive and can therefore formally be described by the dispersive Hamiltonian $\hat{H}_0 = \hbar\omega_0(x_0)\hat{a}^\dagger\hat{a}$, where $\hat{a}^\dagger\hat{a}$ denotes the intracavity photon number. Linearized for small fluctuations $x \ll \alpha^{-1}$ around x_0 , for example, the Brownian motion of the string placed at x_0 , the interaction Hamiltonian reads: $\hat{H}_{\text{int}} = \hat{H}_0 + \hbar g(x_0)\hat{x}\hat{a}^\dagger\hat{a}$ with the optomechanical coupling rate $g(x_0) = d\omega_0(x_0)/dx_0$.

Experimentally, the position-dependent optomechanical coupling rates of the nanomechanical string to the microcavity can be obtained by taking the derivative of the measured static frequency shifts, that is, $g(x_0) = d\omega_0(x)/dx|_{x=x_0}$. These statically determined coupling rates reach values up to $g/2\pi = 10 \text{ MHz nm}^{-1}$ (see Fig. 2a). For comparison, also data obtained with a two-dimensional (2D) nanomechanical oscillator in the form of a $30 \text{ nm} \times 40 \mu\text{m} \times 50 \mu\text{m}$ sheet of Si_3N_4 are shown, which also show purely dispersive coupling (see Fig. 2b) of up to $g/2\pi = 20 \text{ MHz nm}^{-1}$. This sizeable coupling is due to the small mode volume V_{cav} of toroid microcavities because the optomechanical coupling scales as $g \propto (V_{\text{nano}}/V_{\text{cav}}) \cdot \omega_0/l$, where l is the characteristic length scale, which in our case is given by the field intensity decay length, that is, $l = 1/(2\alpha) \approx 110 \text{ nm}$ (see Supplementary Information for analytical expressions of g). Yet higher optomechanical coupling rates can be attained in our system by reducing the size of the microcavity and the wavelength of the used light. An integrated photonic-crystal device with a larger ratio $V_{\text{nano}}/V_{\text{cav}}$, recently allowed remarkably large coupling rates of about 100 GHz nm^{-1} to be obtained²⁵. It however also entailed the difficulty of obtaining sufficiently high optical Q in photonic-crystal cavities such that the resolved-sideband regime where the optical linewidth is comparable to or smaller than the mechanical oscillation frequency could not be achieved in ref. 25. The approach presented here, in contrast, separates optical and mechanical degrees of freedom. As the nanomechanical oscillators do not induce any measurable losses to the ultrahigh-finesse microresonators, it thus particularly allows combination of the toroids' high optical Q ($> 10^8$) with high mechanical Q and falls naturally into the resolved-sideband regime, which enables ground-state cooling^{28,29} or backaction-evading measurements⁶.

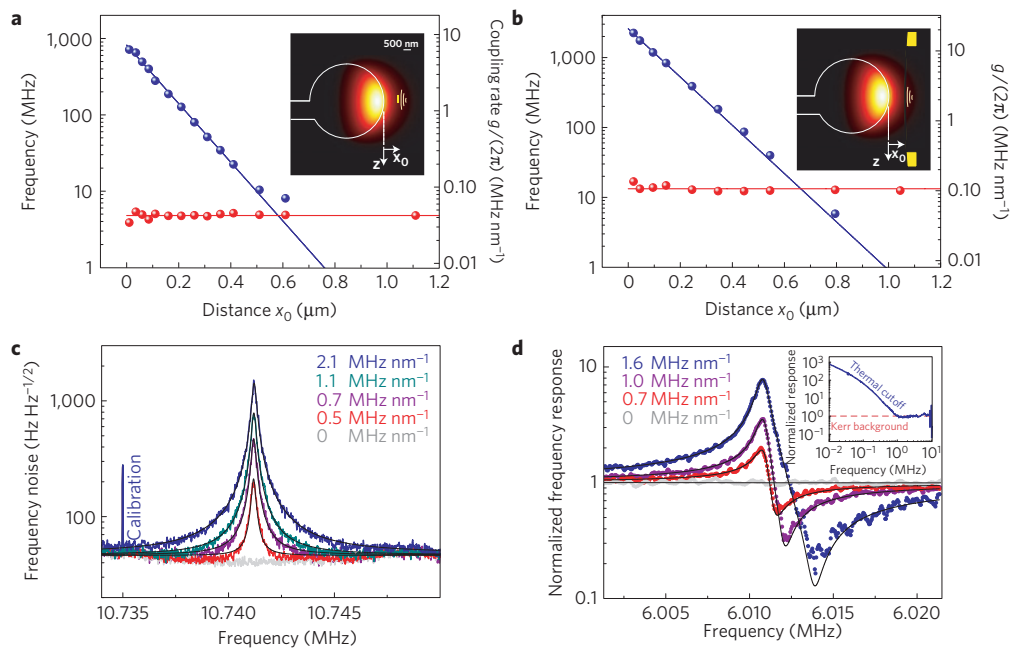


Figure 2 | Characterization of the optomechanical coupling. **a, b**, The dependence of a 58- μm -diameter optical microcavity's linewidth (red) and negative optical frequency shift (blue) as a function of the distance x_0 to nanomechanical oscillators in the form of a doubly clamped SiN string ($110\text{ nm} \times 800\text{ nm} \times 25\text{ }\mu\text{m}$ (**a**)) and a 2D Si_3N_4 sheet ($30\text{ nm} \times 40\text{ }\mu\text{m} \times 50\text{ }\mu\text{m}$ (**b**)). The data reveal in both cases purely dispersive coupling without introducing a measurable degradation of the microcavities' optical decay rate. The right axes show the static optomechanical coupling rates $g(x_0) = d\omega_0(x_0)/dx_0$, as given by the negative derivative of the fitted frequency shift data (blue alone). Coupling rates $g/2\pi$ of order 10 MHz nm^{-1} are achieved. **c**, The Brownian noise associated with the nanomechanical oscillator of **a** transduced by the optical cavity for different oscillator positions. The respective dynamical coupling rates $g/2\pi$ are derived from the calibrated frequency noise spectra $S_{\omega\omega}[\Omega]$ as explained in the text. **d**, The interference of the nanomechanical oscillator's force and the microcavity's Kerr response to a modulated laser field, confirming the attractive nature of the dipole force. This measurement represents a third, independent method to determine the optomechanical coupling rates (see text and Supplementary Information). Inset: Broadband response of the nanomechanical oscillator–microcavity system, showing thermal cutoff and Kerr background as well as the first low- Q mechanical modes of the microcavity. It is noted that the presence/absence of the nanomechanical oscillator does not alter this broadband, off-resonant response.

Transduction of nanomechanical motion

The optomechanical coupling rate transduces the motion of the nanomechanical oscillator's eigenmodes (characterized by the displacement spectral density $S_{xx}[\Omega]$) into frequency noise $S_{\omega\omega}[\Omega]$ of the optical cavity mode. Figure 2c shows the Brownian motion of a nanostring at room temperature ($110\text{ nm} \times 800\text{ nm} \times 25\text{ }\mu\text{m}$, $\Omega_m/2\pi = 10.74\text{ MHz}$, $Q = 53,000$, $m_{\text{eff}} = 3.6\text{ pg}$, $x_{\text{rms}} = 16\text{ pm}$) imprinted into cavity frequency noise, probed by a laser locked to cavity resonance and calibrated using a known external frequency modulation^{13,14}. The nanostring's room-temperature Brownian noise $S_{xx}[\Omega]$ can thus be used to directly determine the optomechanical coupling $g = \sqrt{S_{\omega\omega}/S_{xx}}$ in a second, independent way. We refer to this as a dynamic measurement. Both for the SiN nanostring and the 2D Si_3N_4 nanosheet, the values obtained for the dynamically measured coupling rates are in good agreement with the statically determined values (see Supplementary Information). It is important to note that this identity of static and dynamic coupling rates is in agreement with the expectation for optical dipolar interaction, which should give rise to frequency-independent optomechanical coupling rates g . The non-measurably small optical losses ($<0.5\text{ ppm}$) induced by the nanostrings also indicate that dissipative coupling mediated by thermal effects caused by light absorption has an insignificant role. Indeed, differentiating radiation pressure from thermal effects is a challenge that has eluded researchers for centuries. A prominent example is the light mill that can be driven by thermal heating, rather than by radiation pressure. More recently, thermal effects have been shown to have a significant role in micro- and nanomechanical systems^{25,36,37}. It is, however, only the conservative

Hamiltonian of radiation pressure that allows phenomena such as ponderomotive squeezing³¹ or QND measurements of photons³². Therefore, it is central to clearly identify the origin of the optomechanical interaction.

Demonstration of radiation-pressure interaction

The optomechanical coupling not only gives rise to a differential cavity-frequency shift that transduces the nanostring's mechanical motion but also conveys the per-photon force $-\hbar g(x_0)$ inevitably acting on the mechanical degree of freedom, as expected for any linear continuous position measurement. As proof that the optical dipole force mediates the optomechanical coupling—rather than thermal effects^{36,37}—we carry out a pump–probe measurement that probes the force response of the nanomechanical oscillator. A resonant, intensity-modulated pump laser provides the modulated force $\delta F[\Omega] = -\hbar g \delta N[\Omega]$ (where N is the intracavity photon number) acting on the nanomechanical oscillator while a second, weak probe laser measures the response of the cavity resonance frequency. The measured data (see Fig. 2d) consist of the nanomechanical oscillator's force response, interfering with the constant background due to the Kerr nonlinearity of silica (that is, its intensity-dependent refractive index, see Fig. 2d and ref. 20). Note that the data for different optomechanical coupling rates are scaled to the constant Kerr background, which allows an accurate determination of the magnitude of the nanomechanical oscillator's response. Two important conclusions can be drawn from this measurement. First, the shape of the interference in Fig. 2d implies that the force experienced by the nanomechanical oscillator is attractive (that is, pointing towards higher intensity) as expected for an optical-gradient force. Below its

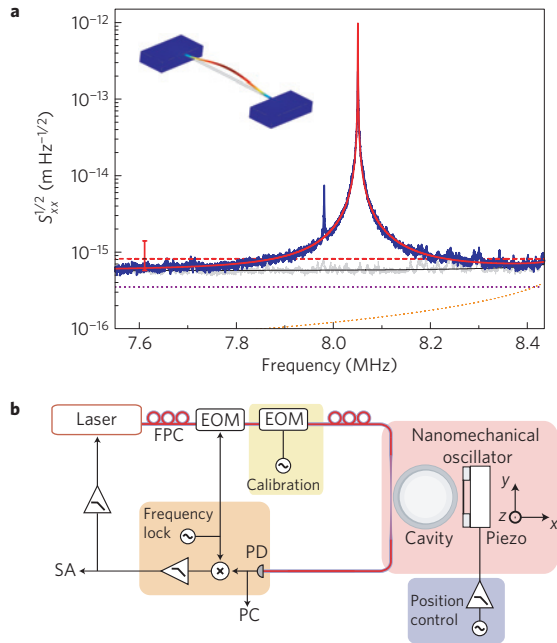


Figure 3 | Displacement measurement of a nanomechanical oscillator with an imprecision at the SQL. **a**, Room-temperature Brownian noise of a nanomechanical string with a fundamental resonance frequency of 8 MHz and dimensions $110 \text{ nm} \times 800 \text{ nm} \times 35 \text{ }\mu\text{m}$ ($m_{\text{eff}} = 4.9 \text{ pg}$, $Q = 40,000$). For an input power of $65 \text{ }\mu\text{W}$, the displacement imprecision reaches a value of $570 \text{ am Hz}^{-1/2}$ (grey line), 0.7 times the SQL, that is, the oscillator's expected zero-point fluctuations of $820 \text{ am Hz}^{-1/2}$ (red dashed line). The large dynamic range across the wide frequency window gives rise to a 1.5 dB error bar for this value (shown in red). The background is due to laser shot-noise (purple dotted line) with smaller contributions from thermal noise of the cavity (orange dotted line), thermorefractive and detector noise (not shown). The second, 20 dB smaller peak is attributed to a second resonator in the toroid's field of view. Inset: Finite-element simulation of the string's fundamental mode. **b**, A schematic of the measurement set-up used to attain an imprecision at the SQL using a low-noise fibre laser emitting at $1,548 \text{ nm}$ and locked to cavity resonance ($\kappa/2\pi = 50 \text{ MHz}$ for the measurement shown in **a**). PD: photodiode, PC: personal computer, SA: spectrum analyser, EOM: electro-optic modulator, FPC: fibre-coupled polarization controller.

resonance frequency, where the mechanical oscillator responds in phase with a modulated force, it is pulled towards the optical mode, which leads to an increased redshift, adding to the in-phase redshift due to the Kerr contribution. Above its resonance frequency where the nanomechanical oscillator responds with a phase lag of 180° , the attractive force leads to destructive interference with the in-phase Kerr response. Second, the ratio of the mechanical to the Kerr nonlinearity response constitutes a relative measure²⁰ and allows derivation of the per-photon force acting on the nanomechanical oscillator independent of the optical parameters (cavity linewidth, coupling conditions, input power). The coupling rates g independently measured in this per-photon-force measurement match the values determined by both methods presented earlier (see Supplementary Information for more details). This measurement thus unambiguously demonstrates that the interaction of the nanomechanical oscillator and the optical cavity is mediated by the dispersive, ponderomotive radiation-pressure interaction, that is, the optical dipole force. No thermal forces are observable.

Measurement imprecision at the SQL

Having established its ponderomotive origin, we use the optomechanical coupling to obtain a high-sensitivity readout of

nanomechanical motion with an imprecision at the SQL. To this end, we use a low-noise fibre laser that is quantum-limited in both amplitude and phase at the Fourier frequency of the mechanical oscillators ($>6 \text{ MHz}$), resonantly locked using a Pound–Drever–Hall technique¹². The experimental set-up is shown in Fig. 3b. Remarkably, using a $\kappa/2\pi = 50 \text{ MHz}$ optical mode, more than 60 dB signal to background ratio can be obtained when measuring the Brownian motion $S_{xx}[\Omega_m]$ of nanomechanical strings at room temperature. In an ideal measurement, the background of the measurement is given only by laser shot-noise, which limits the single-sided displacement sensitivity attainable for an input power P_{in} and an impedance matched cavity to¹²:

$$\sqrt{S_{xx}[\Omega]} = \sqrt{\frac{\hbar\omega_0}{P_{\text{in}}} \frac{\kappa/2}{\sqrt{2}g}} \sqrt{1 + 4\frac{\Omega^2}{\kappa^2}} \quad (2)$$

The best single-sided displacement sensitivity (as determined from the background of the measurement) that was achieved amounts to $S_{xx}^{1/2} = 570 \text{ am Hz}^{-1/2}$, as shown in Fig. 3a, using an 8 MHz doubly clamped nanomechanical SiN string ($110 \text{ nm} \times 800 \text{ nm} \times 35 \text{ }\mu\text{m}$, $m_{\text{eff}} = 4.9 \text{ pg}$, $Q = 40,000$), $65 \text{ }\mu\text{W}$ input power and a coupling rate of $g/2\pi = 3.8 \text{ MHz nm}^{-1}$.

To allow a comparison of the attained imprecision with values obtained using other nanomechanical motion transducers, we scale it to the nanomechanical oscillator's zero-point fluctuations, which for the nanoring of Fig. 3 amount to $820 \text{ am Hz}^{-1/2}$ (single-sided). Thus, our measurement imprecision amounts to only 0.7 times the oscillator's zero-point fluctuations, that is, 0.7 times the SQL. Interestingly, the condition for a measurement with an imprecision better than the zero-point fluctuations can (for both single- and double-sided spectra) be recast into the condition of a signal-to-background ratio greater than $\sqrt{2k_B T/\hbar\Omega_m} \cong \sqrt{2\bar{n}}$, where $\bar{n} \cong k_B T/\hbar\Omega_m$ denotes the average phonon occupation number of the mechanical mode (T : temperature, k_B : Boltzmann constant). Such an imprecision had so far never been achieved, neither with the best transducers of nanomechanical motion based on electronic current flow using single-electron transistor¹⁰, atomic point contact¹¹ and superconducting quantum interference device²³ sensors operating in a cryogenic environment, nor with integrated photonic-crystal systems²⁵. Thus, although higher absolute sensitivity has recently been obtained for an oscillator that is ten times heavier²⁵, our approach for the first time allows the measurement of nanomechanical motion with an imprecision at the SQL.

Although the current measurement allows inferring an upper bound of $380 \text{ am Hz}^{-1/2}$ for the shot-noise limit (in agreement with equation (2), see Supplementary Information), our measurement is at present also partially limited by detector noise, which can be eliminated by means of straightforward technical amendments. Moreover, further improvements are readily feasible. Using smaller microcavities and a shorter optical wavelength may allow an increase of g by up to one order of magnitude. Thus, displacement sensitivities at the level of $10^{-17} \text{ m Hz}^{-1/2}$ may be attainable, which would allow measurements with an imprecision far below the SQL. Ultimately, the background afforded by mechanical modes of the cavity^{13,38} (see Fig. 3a) and thermorefractive noise^{13,39} of the cavity will limit the sensitivity. These noise sources can, however, in principle be suppressed by cryogenic operation, which toroid microcavities have been shown to be compatible with⁴⁰.

Radiation-pressure dynamical backaction

A second important ramification of the reported cavity–optomechanical system stems from the fact that the nanomechanical oscillators show oscillation frequencies that equal or even exceed the photon decay rate of the optical resonator, enabling access to the regime of dynamical backaction both in the Doppler^{18–20} and

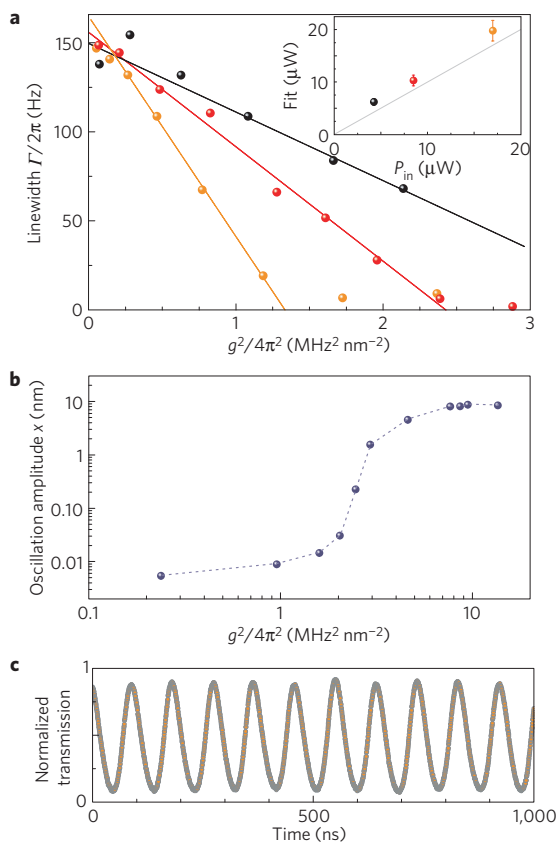


Figure 4 | Observation of radiation-pressure-induced dynamical backaction and coherent oscillations of a nanomechanical oscillator. **a**, Mechanical linewidth of a SiN nanostring (110 nm × 800 nm × 25 μm with a Q of 70,000 at 10.8 MHz and $m_{\text{eff}} = 3.6$ pg) as a function of the optomechanical coupling rate for three different launched powers but fixed blue-detuning $\Delta = +\kappa/2$ ($\kappa/2\pi = 12$ MHz). The lines are fits to the dipolar force contribution using the input power as the only fit parameter, which is in good agreement with the actual input power used (inset). Regions where the linewidth drops to a value close to zero coincide with the onset of regenerative mechanical oscillations. **b**, The oscillation amplitude of the nanomechanical string (derived from a 30-Hz-bandwidth power measurement) as a function of the optomechanical coupling showing threshold and saturation at typical values of 10 nm. **c**, The transmitted power past the cavity (normalized by the off-resonant transmission) for a nanomechanical string in the regime of the parametric oscillation instability. The coherent mechanical oscillation of the 3.6 pg string at 10.8 MHz causes a close to unity modulation depth of the optical field transmitted by the cavity.

resolved-sideband^{14,28,29} limits. To observe dynamical backaction, the optical microcavity is excited with a positive laser detuning $\Delta = \omega - \omega_0(x_0)$, which can lead to maser/laser-like amplification⁴¹ of mechanical motion. Thereby, the mechanical oscillator resumes the role of the photon field in the laser and the cavity, in turn, has the role of the (phonon) gain medium. As in the case of a laser, the canonical signs of this phenomenon are linewidth narrowing, threshold behaviour and eventual saturation of the oscillation. All of these features are observed with the nanomechanical strings as shown in Fig. 4. For fixed detuning, the backaction gain rate $\Gamma_{\text{ba}} \propto -g^2 P_{\text{in}}/m_{\text{eff}}$ (see Supplementary Information) grows linearly with increased g^2 . In the experiment, the optomechanical coupling g is varied (for fixed detuning $\Delta = \kappa/2$, $\kappa/2\pi = 12$ MHz), giving rise to a narrowing of the total mechanical linewidth $\Gamma = \Gamma_m + \Gamma_{\text{ba}}$, as shown in Fig. 4a ($\Gamma_m/2\pi$ denotes the intrinsic mechanical damping rate). The experimentally observed slopes

$\partial\Gamma/\partial(g^2)$ are in good quantitative agreement with the theoretical expectation for the dipolar force (see inset Fig. 4a). When the backaction rate eventually equals the mechanical damping rate, the nanomechanical oscillator experiences net gain, which leads to the onset of coherent mechanical oscillations. A clear threshold of the mechanical oscillation amplitude as shown in Fig. 4b is observable, followed by a saturation of the mechanical motion once the frequency shift caused by the mechanical oscillator exceeds the cavity linewidth, leading to gain saturation. Indeed, the large coherent oscillations of several nanometres in amplitude can lead, remarkably and despite the nanoscale nature of the strings, to near-unity modulation depth of the optical-cavity transmission, as shown in Fig. 4c, when the oscillation amplitude is close to $(\kappa/2)/g$. The resulting radiofrequency signal may serve as a photonic clock⁴² and is expected to show a linewidth limited only by thermal noise, as in the case of a maser⁴¹. The observation of dynamical backaction amplification (and coherent oscillations) constitutes the first report of dynamical backaction onto a nanomechanical oscillator using radiation pressure (in contrast to thermal effects^{25,36}), and in particular using optical gradient or dipole forces. So far, in the field of nanomechanics, dynamical backaction cooling or amplification has been achieved only using microwave fields⁴³, which owing to the about $\times 10^4$ longer wavelength show lower coupling rates and do not allow access to quantum-limited displacement sensing yet (albeit significant progress is being made⁴⁴).

Outlook

The extension of quantum-limited sensitivity with an imprecision at the SQL and dynamical backaction to nanomechanical systems manifests a promising realm for future studies explaining the quantum nature of optomechanical interaction. Remarkably, we note that combined with state-of-the-art nanomechanical strings³⁰, the ratio of radiation-pressure quantum backaction (the force noise provided by photon shot-noise) and thermal force spectral density can reach unity at room temperature owing to the very small (picogram) mass and ultrahigh finesse ($>400,000$) of the optomechanical system (see Supplementary Information). This brings the long sought-after^{6,7} regime of quantum backaction into reach even at room temperature, which would allow ponderomotive squeezing³¹ or QND measurements of the intracavity field^{32,33}. A further distinguishing feature of the presented approach is that by coupling the nanostrings transversely to the direction of the whispering-gallery mode field, quadratic coupling to the position coordinate of the nanomechanical oscillators enabling QND measurements of mechanical motion^{45,46} can be implemented by exploiting the standing-wave mode patterns that microresonators can show (see Supplementary Information).

Pertaining to the wider implications, the presented approach allows coupling to virtually any dielectric nanomechanical oscillator. The ability to combine nanoscale mechanical oscillators—which are at the heart of proximity (Casimir) force sensors and a variety of other high-resolution measurement techniques^{3–5}—with quantum-limited displacement sensitivity at the sub-fm Hz^{-1/2} level conceivably offers opportunities for improved performance in these research fields. Particularly interesting may also be the study of graphene sheets²⁷. The possibility to couple several mechanical oscillators to a single optical mode may moreover provide a straightforward way to achieve optically mediated coupling between different mechanical oscillators. Finally, the used microtoroidal platform has already been demonstrated as an interface for atomic cavity quantum electrodynamics⁴⁷, enabling potentially the interaction of phonons, photons and atoms or qubits, as recently proposed^{48,49}.

Note added in proof. After submission of this work, a measurement of nanomechanical motion using microwaves with an imprecision at the SQL was reported⁵⁰.

Received 13 May 2009; accepted 4 September 2009;
published online 11 October 2009

References

- Craighead, H. G. Nanoelectromechanical systems. *Science* **290**, 1532–2537 (2000).
- Ekinci, K. L. & Roukes, M. L. Nanoelectromechanical systems. *Rev. Sci. Instrum.* **76**, 061101 (2005).
- Jensen, K., Kwanpyo, K. & Zettl, A. An atomic-resolution nanomechanical mass sensor. *Nature Nanotech.* **3**, 533–537 (2008).
- Cleland, A. & Roukes, M. A nanometre-scale mechanical electrometer. *Nature* **392**, 160–162 (1998).
- Rugar, D., Budakian, R., Mamin, H. & Chui, B. Single spin detection by magnetic resonance force microscopy. *Nature* **430**, 329–332 (2004).
- Braginsky, V. B. & Khalili, F. Y. *Quantum Measurement* (Cambridge Univ. Press, 1992).
- Tittonen, I. *et al.* Interferometric measurements of the position of a macroscopic body: Towards observation of quantum limits. *Phys. Rev. A* **59**, 1038–1044 (1999).
- Caves, C. M. Quantum-mechanical noise in an interferometer. *Phys. Rev. D* **23**, 1693–1708 (1981).
- Clerk, A. A., Devoret, M. H., Girvin, S. M., Marquardt, F. & Schoelkopf, R. J. Introduction to quantum noise, measurement and amplification. Preprint at <http://arxiv.org/abs/0810.4729v1> (2008).
- LaHaye, M. D., Buu, O., Camarota, B. & Schwab, K. C. Approaching the quantum limit of a nanomechanical resonator. *Science* **304**, 74–77 (2004).
- Flowers-Jacobs, N. E., Schmidt, D. R. & Lehnert, K. W. Intrinsic noise properties of atomic point contact displacement detectors. *Phys. Rev. Lett.* **98**, 096804 (2007).
- Arcizet, O. *et al.* High-sensitivity optical monitoring of a micromechanical resonator with a quantum-limited optomechanical sensor. *Phys. Rev. Lett.* **97**, 133601 (2006).
- Schliesser, A., Anetsberger, G., Riviere, R., Arcizet, O. & Kippenberg, T. J. High-sensitivity monitoring of micromechanical vibration using optical whispering gallery mode resonators. *New J. Phys.* **10**, 095015 (2008).
- Schliesser, A., Riviere, R., Anetsberger, G., Arcizet, O. & Kippenberg, T. J. Resolved-sideband cooling of a micromechanical oscillator. *Nature Phys.* **4**, 415–419 (2008).
- Unterreitmeier, Q. P., Weig, E. M. & Kotthaus, J. P. Universal transduction scheme for nanomechanical systems based on dielectric forces. *Nature* **458**, 1001–1004 (2009).
- Braginsky, V. & Manukin, A. *Measurement of Weak Forces in Physics Experiments* (Univ. Chicago Press, 1977).
- Kippenberg, T. J. & Vahala, K. J. Cavity optomechanics: Back-action at the mesoscale. *Science* **321**, 1172–1176 (2008).
- Arcizet, O., Cohadon, P.-F., Briant, T., Pinard, M. & Heidman, A. Radiation-pressure cooling and optomechanical instability of a micromirror. *Nature* **444**, 71–74 (2006).
- Gigan, S. *et al.* Self-cooling of a micromirror by radiation pressure. *Nature* **444**, 67–70 (2006).
- Schliesser, A., Del'Haye, P., Nooshi, N., Vahala, K. J. & Kippenberg, T. J. Radiation pressure cooling of a micromechanical oscillator using dynamical backaction. *Phys. Rev. Lett.* **97**, 243905 (2006).
- Kippenberg, T. J., Rokhsari, H., Carmon, T., Scherer, A. & Vahala, K. Analysis of radiation-pressure induced mechanical oscillation of an optical microcavity. *Phys. Rev. Lett.* **95**, 033901 (2005).
- Schwab, K. C. & Roukes, M. L. Putting mechanics into quantum mechanics. *Phys. Today* **58**, 36–42 (2005).
- Etaki, S. *et al.* Motion detection of a micromechanical resonator embedded in a d.c. SQUID. *Nature Phys.* **4**, 785–788 (2008).
- Poggio, M. *et al.* An off-board quantum point contact as a sensitive detector of cantilever motion. *Nature Phys.* **4**, 635–638 (2008).
- Eichenfield, M., Camacho, R., Chan, J., Vahala, K. & Painter, O. A picogram- and nanometre scale photonic-crystal optomechanical cavity. *Nature* **459**, 550–555 (2009).
- Cui, Y., Wei, Q., Park, H. & Lieber, C. M. Nanowire nanosensors for highly sensitive and selective detection of biological and chemical species. *Science* **293**, 1289–1292 (2001).
- Bunch, J. S. *et al.* Electromechanical resonators from graphene sheets. *Science* **315**, 490–493 (2007).
- Wilson-Rae, I., Nooshi, N., Zwerger, W. & Kippenberg, T. J. Theory of ground state cooling of a mechanical oscillator using dynamical backaction. *Phys. Rev. Lett.* **99**, 093901 (2007).
- Marquardt, F., Chen, J. P., Clerk, A. A. & Girvin, S. M. Quantum theory of cavity-assisted sideband cooling of mechanical motion. *Phys. Rev. Lett.* **99**, 093902 (2007).
- Verbridge, S. S., Craighead, H. G. & Parpia, J. M. A megahertz nanomechanical resonator with room temperature quality factor over a million. *Appl. Phys. Lett.* **92**, 013112 (2008).
- Fabre, C. *et al.* Quantum-noise reduction using a cavity with a movable mirror. *Phys. Rev. A* **49**, 1337–1343 (1994).
- Heidmann, A., Hadjar, Y. & Pinard, M. Quantum nondemolition measurement by optomechanical coupling. *Appl. Phys. B: Laser Optics* **64**, 173–180 (1997).
- Verlot, P., Tavernarakis, A., Briant, T., Cohadon, P.-F. & Heidmann, A. Scheme to probe optomechanical correlations between two optical beams down to the quantum level. *Phys. Rev. Lett.* **102**, 103601 (2009).
- Vitali, D. *et al.* Optomechanical entanglement between a movable mirror and a cavity field. *Phys. Rev. Lett.* **98**, 030405 (2007).
- Favero, I. & Karrai, K. Cavity cooling of a nanomechanical resonator by light scattering. *New J. Phys.* **10**, 095006 (2008).
- Zalalutdinov, M. *et al.* Autoparametric optical drive for micromechanical oscillators. *Appl. Phys. Lett.* **79**, 695–697 (2001).
- Höhberger Metzger, C. & Karrai, K. Cavity cooling of a microlever. *Nature* **432**, 1002–1005 (2004).
- Anetsberger, G., Riviere, R., Schliesser, A., Arcizet, O. & Kippenberg, T. Ultralow-dissipation optomechanical resonators on a chip. *Nature Photon.* **2**, 627–633 (2008).
- Gorodetsky, M. L. & Grudinin, I. S. Fundamental thermal fluctuations in microspheres. *J. Opt. Soc. Am. B* **21**, 697–705 (2004).
- Arcizet, O., Riviere, R., Schliesser, A., Anetsberger, G. & Kippenberg, T. J. Cryogenic properties of optomechanical silica microcavities. *Phys. Rev. A* **80**, 021803 (2009).
- Schawlow, A. L. & Townes, C. H. Infrared and optical masers. *Phys. Rev.* **112**, 1940–1949 (1958).
- Hosseini-Zadeh, M., Rokhsari, H., Hajimiri, A. & Vahala, K. J. Characterization of a radiation-pressure-driven micromechanical oscillator. *Phys. Rev. A* **74**, 023813 (2006).
- Teufel, J. D., Harlow, J. W., Regal, C. A. & Lehnert, K. W. Dynamical backaction of microwave fields on a nanomechanical oscillator. *Phys. Rev. Lett.* **101**, 197203 (2008).
- Castellanos-Beltran, M., Irwin, K., Hilton, G., Vale, L. & Lehnert, K. Amplification and squeezing of quantum noise with a tunable Josephson metamaterial. *Nature Phys.* **4**, 929–931 (2008).
- Thompson, J. D. *et al.* Strong dispersive coupling of a high-finesse cavity to a micromechanical membrane. *Nature* **452**, 72–75 (2008).
- Miao, H., Danilishin, S., Corbitt, T. & Chen, Y. Standard quantum limit for probing mechanical energy quantization. *Phys. Rev. Lett.* **103**, 100402 (2009).
- Aoki, T. *et al.* Observation of strong coupling between one atom and a monolithic microresonator. *Nature* **443**, 671–674 (2006).
- Hammerer, K., Aspelmeyer, M., Polzik, E. S. & Zoller, P. Establishing Einstein–Poldosky–Rosen channels between nanomechanics and atomic ensembles. *Phys. Rev. Lett.* **102**, 020501 (2009).
- Rabl, P. *et al.* Strong magnetic coupling between an electronic spin qubit and a mechanical resonator. *Phys. Rev. B* **79**, 041302 (2009).
- Teufel, J. D., Donner, T., Castellanos-Beltran, M. A., Harlow, J. W. & Lehnert, K. W. Nanomechanical motion measured with precision beyond the standard quantum limit. Preprint at <http://arxiv.org/abs/0906.1212v1> (2009).

Acknowledgements

T.J.K. acknowledges financial support by an Independent Max Planck Junior Research Group of the Max Planck Society, an ERC Starting Grant (SIMP), MINOS and a Marie Curie Excellence Grant as well as the Nanosystems Initiative Munich (NIM). J.P.K. acknowledges financial support by the Deutsche Forschungsgemeinschaft through project Ko 416/18, the German Excellence Initiative through the Nanosystems Initiative Munich (NIM) and LMUexcellent as well as LMUinnovativ. O.A. acknowledges financial support from a Marie Curie Intra European Fellowship within FP7 (project QUOM). T.J.K. thanks P. Gruss and the MPQ for continued Max-Planck support. The authors thank M.L. Gorodetsky for valuable discussions.

Author contributions

J.P.K. initiated the study and jointly devised the concept with T.J.K. G.A. and O.A. planned, carried out and analysed the experiments supervised by T.J.K. Q.P.U. and E.M.W. designed and developed suitable nanomechanical resonators. All authors discussed the results and contributed to the manuscript. R.R. contributed to the development of the experimental apparatus and A.S. assisted with the response measurements.

Additional information

Supplementary information accompanies this paper on www.nature.com/naturephysics. Reprints and permissions information is available online at <http://npg.nature.com/reprintsandpermissions>. Correspondence and requests for materials should be addressed to T.J.K.

On-Chip Interferometric Detection of Nanomechanical Motion

Quirin P. Unterreithmeier, Thomas Faust, Stephan Manus, and Jörg P. Kotthaus*

Fakultät für Physik and Center for NanoScience (CeNS), Ludwig-Maximilians-Universität, Geschwister-Scholl-Platz 1, München 80539, Germany

ABSTRACT An integrable on-chip displacement transduction of nanomechanical motion is developed that senses the modulation of the optical near-field of an illuminated vibrating string with a nearby Schottky photodiode. This scheme poses no restrictions on resonator material and avoids additional damping. The achieved sensitivity of $1 \text{ pm/Hz}^{1/2}$ enables the detection of Brownian motion of our mechanical resonators at room temperature. Implementing a feedback scheme of the detected signal into the electrical actuation, we demonstrate self-oscillation.

KEYWORDS Nanomechanics, photodetection, motion detection, near-field interferometry, self-oscillation

The study of nanoelectromechanical systems (NEMS) is a rapidly evolving field of science, with implications ranging from fundamental science^{1–5} to applications such as ultrasensitive systems detecting, e.g., mass,⁶ temperature,⁷ charge⁸ or nuclear spins,⁹ and signal generation¹⁰ or processing.¹¹ Displacement detection schemes for such systems may be divided into two classes. One being optical interference techniques^{1,3,12–14} which have the advantage of being material independent, yet usually require external components. The other utilizing on-chip components that transduce mechanical motion into modulated electrical signals,^{2,15–20} with the inherent benefit of being integrable. The drawback of these techniques is their restriction to either low temperatures^{2,15} and/or specific materials.^{16–20} Here, we present a detection scheme that combines the local generation of the measurement signal and material independence. Our scheme is derived from the interferometric setup; there the mechanical resonator (and its surroundings) is illuminated and the reflected²¹ or diffracted²² beam is re-collected. Mechanical displacement is converted into a modulation of the measured light intensity. Complementary to these schemes, we directly study the intensity modulation in the near-field of the resonator with a local photodiode, thereby creating an on-chip signal.

Figure 1a shows our setup: we study the displacement of a doubly clamped silicon nitride resonator of dimensions $35 \mu\text{m} \times 100 \text{ nm} \times 200 \text{ nm}$ (length, height, width, respectively). The utilized wafer consists of a typical sandwich structure: the substrate is n-doped ($\approx 10 \Omega\text{cm}$) silicon that is partly oxidized, forming a 400 nm thick sacrificial layer. The device layer on top is composed of prestressed silicon nitride, leading to high mechanical quality factors²³ of, in this case, 10^5 . The fabrication implements standard e-beam

lithographic methods and subsequent reactive ion- and wet-etches to release the resonator. The wet-etch partly removes the silicon oxide with a remaining thickness of about 50 nm.

We electrically actuate our resonator via a pair of suitably biased electrodes processed on the postreleased structure nearby the resonator leading to an attractive dielectric force.^{12,24} The high mechanical quality factor facilitates considerable displacements at low driving powers. A second pair of electrodes is processed with a small area in direct contact to the silicon substrate. This is accomplished by locally removing the SiO_2 employing another e-beam and wet etch step, leaving clearly visible depressions in the SiO_2 ,

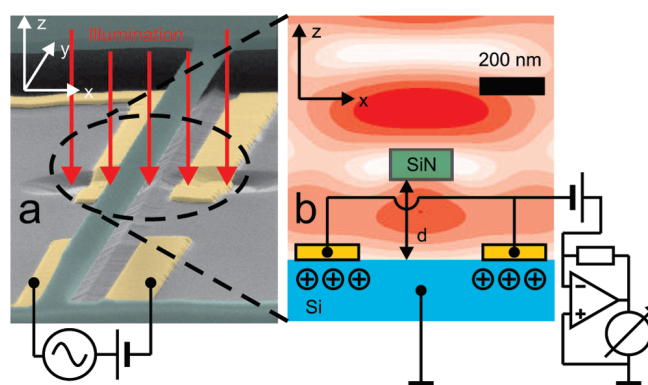


FIGURE 1. Setup and detection principle: (a) SEM picture (false color) of the sample; highlighted in green is the silicon nitride device layer forming the mechanical resonator and its supports. Two pairs of electrodes are marked in yellow; one pair serves as dielectric actuator, being suitably biased by dc and rf voltages. Small parts of the second electrode pairs are in direct contact with the silicon substrate, thereby forming a Schottky contact, as seen in the encircled area and in (b). Schematic cross section of the detection configuration; illumination (and suitably chosen bias) gives rise to a photocurrent that is detected using a current–voltage converter placed close to the sample. Interference and scattering lead to a nonuniform distribution of the resulting optical intensity in the near-field of the resonator; this intensity distribution is modulated by the displacement of the mechanical resonator, resulting in an rf part of the photocurrent.

* To whom correspondence should be addressed, kotthaus@lmu.de.

Received for review: 10/23/2009

Published on Web: 00/00/0000

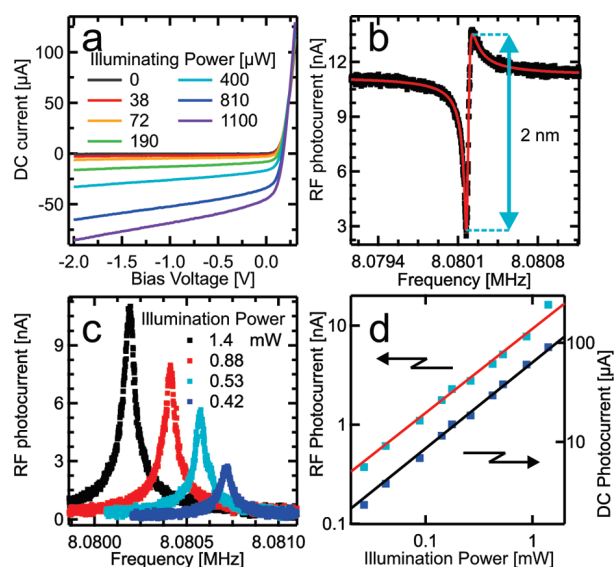


FIGURE 2. dc and rf photocurrent (diode laser illumination): (a) dc current traces vs applied voltage are displayed for different illumination powers, clearly exhibiting diode-like behavior. (b) Subject to actuation of the mechanical resonator, the rf part of the photocurrent is shown (black points). The resulting resonance can be excellently fitted using a Lorentzian superimposed by frequency-independent cross talk (red line). (c) Four rf resonances with mathematically subtracted cross talk are displayed, measured with different illumination powers. The resonance frequency is shifted by optical gradient forces. (d) The on-resonance rf photocurrent amplitude (light blue dots) and the dc photocurrent (dark blue dots) are depicted for illumination powers ranging over 2 decades. Both measurements can be seen to be proportional to the illumination power and with respect to each other, highlighted by the respective fits (red and black line).

as seen in Figure 1a. See Supporting Information for more geometric details. The thus formed Schottky contact causes depletion of the underlying silicon substrate, as indicated in Figure 1b. Illumination of a Schottky contact leads to the generation of mobile charges thus giving rise to a photocurrent. The illumination (coming from the top) forms a standing wave pattern, as sketched in Figure 1b, with the resulting optical near-field depending on the position of the mechanical resonator. As a consequence, the photocurrent is modulated with resonator displacement yielding the resonant signal. We employ the light of either a diode laser (DL, 670 nm) or a superluminescent diode (SLED, its wavelength is centered around 750 nm), coming out of the cleaved end of a bare glass fiber positioned above the resonator.¹⁴ All our measurements are carried out under vacuum $<10^{-4}$ mbar at room temperature.

We now investigate the effect of (different) illumination; in our experiments an illumination power of 1 mW corresponds to an on-chip intensity of 6.4 W/mm^2 . Figure 2a shows the typical dc current–voltage characteristics of the Schottky diode: with no illumination present the current is largely suppressed in reverse bias, i.e., at negative gate voltage; illumination leads to an enhanced (photo)current. We now actuate our mechanical resonator while sweeping the actuation frequency. The resulting rf part of the mea-

sured photocurrent is shown in Figure 2b. The sharp resonance corresponds to the mechanically induced rf photocurrent and is superposed by a frequency-independent background (cross talk). The latter we attribute to capacitive coupling of our actuation signal modulating the depletion region of the Schottky diode. The measured signal can be excellently fitted using a superposition of a Lorentzian line shape centered around the mechanical resonance frequency $f_0 \approx 8 \text{ MHz}$ and a flat background. The indicated displacement amplitude (in nanometers) is obtained as explained below. Please note that all amplitudes in this work are given as half-peak-to-peak values.

Figure 2c shows several such traces for different illumination powers; we mathematically subtract the cross talk resulting in the familiar Lorentzian lineshapes. Two effects arising from different illumination powers are clearly visible. Both the signal strength and the mechanical resonance frequency vary with the intensity. While the former is expected, the latter can be explained as a result of the illumination leading to an optical intensity pattern. As in the case of optical tweezers, see, e.g., ref 25, the resonator is attracted toward the region of larger light intensity. The influence on the mechanical resonance frequency results from the fact that this force is not uniform and hence its gradient counteracts in our geometry the intrinsic mechanical spring constant. This optical effect is in complete analogy to its dc dielectric counterpart employed in our actuation scheme.¹² To exclude heating effects, a model calculation can be found in the Supporting Information.

In order to compare the dc and rf part of the photocurrent, the intensity of the illumination is varied over almost 2 orders of magnitude. The rf amplitude on resonance and the dc part of the photocurrent are logarithmically plotted in Figure 2d. Both results are fitted with a power law ax^b , where x designates the light intensity and a and b are fit parameters. The slope of the curves yields the exponent b . Here the fit gives $b = 0.84$ and 0.86 for the rf and dc part, respectively, showing that both follow the same law. The slight deviation from linear behavior is assumed to reflect the reduction of the depletion zone with higher light intensities. The measurements of Figure 2 were performed using the DL, as it is experimentally easier to attenuate its intensity. Employing the SLED leads to virtually the same results with an additional advantage over the DL apart from setup complexity: in contrast to the output of our SLED, the DL is not externally intensity stabilized. As intensity fluctuations translate into fluctuations of the mechanical frequency, using the DL gives rise to undesirable additional fluctuations of the resonant displacement signal.

The high sensitivity of the setup allows us to directly measure the Brownian motion of our resonators. In Figure 3a we show the spectrum of the photocurrent without any rf actuation (measured with a bandwidth of 50 Hz). The thermally induced mean square displacement is predicted by theory $\langle x^2 \rangle = k_B T / (m_{\text{eff}} (2\pi f_0)^2)$ ($k_B T$ and m_{eff} are thermal

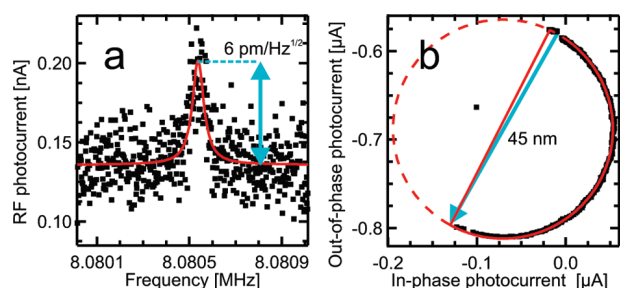


FIGURE 3. Sensitivity and linearity: (a) With no driving present, we measure (black dots) the rf photocurrent showing the Brownian motion of our mechanical resonator (measurement bandwidth, 50 Hz; DL illumination power, 0.8 mW; Schottky bias, 0 V). From theory (red line fit) we thereby obtain a factor to convert the measured signal into displacement. (b) Measurement (black dots) of a strongly actuated mechanical resonance, well within the nonlinear regime (SLED illumination power 1 mW and Schottky bias -2 V). The resulting rf photocurrent is plotted, divided into in- and out-of-phase components. As in the linear case, the measured points follow a circle, as shown by a fit (solid red line) and its continuation to a full circle (dashed red line). Thereby we can deduce that our detection scheme transduces displacements linearly up to amplitudes of 45 nm.

energy and effective mass of the oscillatory mode, respectively); its frequency spectrum is fitted to the experimental data and enables us to convert the measured photocurrent into mechanical displacement²⁶ (also utilized in Figure 2b). Measuring with a 1 Hz bandwidth reduces the whole spectrum uniformly by a factor of $50^{1/2}$, then the maximum would correspond to an amplitude close to $1 \text{ pm/Hz}^{1/2}$, thus representing our estimate of sensitivity. As the noise floor is independent of applied bias across the Schottky diode and illumination power, we deduce that it is generated in the current–voltage converter.

Our measurement scheme avoids additional damping, i.e., preserves the unloaded quality factor. This is in contrast to “passive” schemes such as capacitive²⁰ or magneto-motive^{4,5,10,11,16} detection. There the detection of Brownian motion at room temperature of a resonator with frequency $f_0 = 10 \text{ MHz}$ and an unloaded quality factor $Q = 1 \times 10^5$ degrades the quality factor by 10% when the signal power P exceeds $P = \Delta E f_0 = 0.1 k_B T / Q f_0 \approx 40 \text{ zW}$ (ΔE designates the energy loss per oscillation). The resulting signal corresponding to -164 dBm would be rather difficult to detect.

To check the linearity of the detection scheme, we measure the mechanical displacement subject to strong rf excitation. Figure 3b shows the in- and out-of-phase (quadrature) components of the rf photocurrent while sweeping the frequency. For a harmonic resonator this response is expected to move on a circle when sweeping over a resonance. Here, the measured response is statically shifted with respect to the origin because of the capacitive cross talk. Entering the nonlinear regime of this oscillator, this circular line is only followed in part until a sudden jump to lower amplitude values occurs.²⁷ However, the circular line is clearly followed (no distortion is seen), demonstrating the linearity of the detection scheme up to amplitudes of 45 nm.

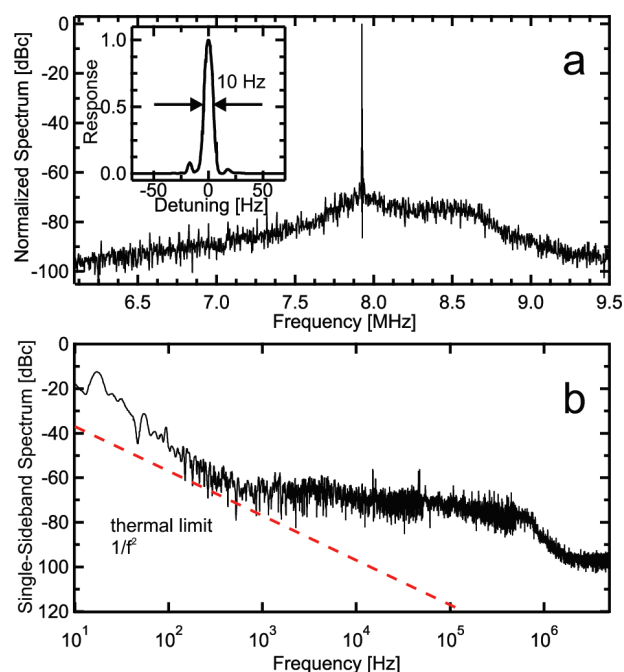


FIGURE 4. Suitably feeding back the displacement signal into the actuating electrodes, we obtain spontaneous oscillation of the resonator (SLED illumination power 1 mW, -2 V Schottky bias). (a) Measured power spectrum of the oscillator. The inset shows a zoom into the sharp resonance linearly plotted vs frequency. We attribute the shoulder visible in the spectrum to our not perfectly suppressed cross talk. (b) The single-sideband phase noise is shown (black line) in comparison to the theoretically predicted minimum (dashed red). For a discussion of the excess noise please see the main text.

Having characterized our detection scheme, we now demonstrate its applicability to implement a feedback-induced nanomechanical (self) oscillator,¹⁰ here operating at room temperature. To obtain such self-oscillation, the detected displacement signal has to be suitably phase shifted, amplified, and fed back into the actuation. In order to suppress unwanted oscillations arising from the on-chip cross talk, a compensation line is introduced to minimize cross talk close to the mechanical resonance frequency. In addition, a bandpass filter is employed to eliminate off-resonant cross talk. Figure 4a shows the resulting power spectrum of the oscillator, biased only by a dc voltage. In the region around the resonance frequency, a prominent maximum dominates the nearly flat background signal. Its narrow line width of only about 10 Hz as visible in the inset is a characteristic of spontaneous feedback-stabilized oscillation. Compared to the case of the directly driven resonator, this represents a narrowing by a factor 8. In Figure 4b the power spectrum is plotted vs the frequency difference, often referred to as phase noise. On the basis of a simple model, see, e.g., ref 28, the theoretical minimum has been shown to have a slope of $-20 \text{ dB per decade}$. In the range of approximately 10–500 Hz the observed slope appears to be steeper, possibly resulting from up-converted flicker noise.¹⁰ We attribute the shoulder visible in the spectrum ranging approximately from 1 to 500 kHz to the not com-

pletely suppressed cross talk, because its frequency range and shape (visible also in Figure 4a) match the frequency response of the employed bandpass filter intended to suppress the cross talk.

In conclusion, we established a new near-field detection scheme employing an on-chip Schottky photodiode and globally illuminated by light with low spatial coherence.¹³ We are thereby able to reduce the external components necessary for the detection of the mechanical displacement of our nanoresonator to a mere illumination, making the scheme widely applicable. Superior to other utilized local detection schemes the near-field approach avoids appreciable loading the Q of the nanomechanical resonator. In addition, the detection scheme does not introduce any restrictions on resonator material such as conductivity.^{4,5,10,11,16,20} We are able to measure the Brownian motion of our resonator at room temperature, achieving a sensitivity exceeding $1 \text{ pm/Hz}^{1/2}$. In addition, we demonstrate its versatility inducing self-oscillation providing a suitable feedback. It is noteworthy that this measurement scheme does not utilize down-conversion¹⁹ or rf-reflection techniques,²⁹ both of which would make it less suitable as clock generator. Beyond the demonstrated performance, there is still plenty of room for improvements. The surrounding area of the mechanical resonator and the Schottky contact have not yet been optimized to yield a maximum phot signal with resonator displacement. Implementing a photonic cavity³ or an optical near-field enhancement²⁵ seems straightforward. In addition, to realize an on-chip stand-alone clock, one would have to integrate the light source on-chip, a task that can be solved by either changing the substrate material or applying wafer bonding techniques.³⁰ One might even speculate that the signal generated in an optimized implementation of such a scheme would be strong enough to sustain self-oscillation without any additional amplification, thereby driven solely by the light source. Our detection scheme could also translate optically induced self-oscillation³¹ into an on-chip electrical signal. Given recent demonstrations of operating nanomechanical resonators under ambient conditions,³² the implementation of all these improvements could yield a completely integrable NEMS clock source. However, it remains to be shown whether the higher integrability and lower power consumption will outperform existing clock sources based on hybrid micromechanical systems.

Acknowledgment. Financial support by the Deutsche Forschungsgemeinschaft via project Ko 416/18 as well as the German Excellence Initiative via the Nanosystems Initiative Munich (NIM) and LMUexcellent is gratefully acknowledged.

Supporting Information Available. Additional information regarding device dimensions and heating of the beam.

This material is available free of charge via the Internet at <http://pubs.acs.org>.

REFERENCES AND NOTES

- (1) Anetsberger, G.; Arcizet, O.; Unterreithmeier, Q. P.; Riviere, R.; Schliesser, A.; Weig, E. M.; Kotthaus, J. P.; Kippenberg, T. J. *Nat. Phys.* **2009**, *5*, 909–914.
- (2) LaHaye, M. D.; Buu, O.; Camarota, B.; Schwab, K. C. *Science* **2004**, *304*, 74–77.
- (3) Eichenfield, M.; Camacho, R.; Chan, J.; Vahala, K. J.; Painter, O. *Nature* **2009**, *459*, 550–556.
- (4) Kozinsky, I.; Postma, H. W. C.; Kogan, O.; Husain, A.; Roukes, M. L. *Phys. Rev. Lett.* **2007**, *99*, 207201.
- (5) Aldridge, J. S.; Cleland, A. N. *Phys. Rev. Lett.* **2005**, *94*, 156403.
- (6) Naik, A. K.; Hanay, M. S.; K. H. W.; Feng, X. L.; Roukes, M. L. *Nat. Nanotechnol.* **2009**, *4*, 445–450.
- (7) Fon, W. C.; Schwab, K. C.; Worlock, J. M.; Roukes, M. L. *Nano Lett.* **2005**, *5*, 1968–1971.
- (8) Cleland, A. N.; Roukes, M. L. *Nature* **1998**, *392*, 160.
- (9) Mamin, H. J.; Poggio, M.; Degen, C. L.; Rugar, D. *Nat. Nanotechnol.* **2007**, *2*, 301–306.
- (10) Feng, X. L.; White, C. J.; Hajimiri, A.; Roukes, M. L. *Nat. Nanotechnol.* **2008**, *3*, 342–346.
- (11) Erbe, A.; Krommer, H.; Kraus, A.; Blick, R. H.; Corso, G.; Richter, K. *Appl. Phys. Lett.* **2000**, *77*, 3102–3104.
- (12) Unterreithmeier, Q. P.; Weig, E. M.; Kotthaus, J. P. *Nature* **2009**, *458*, 1001–1004.
- (13) Li, M.; Pernice, W. H. P.; Tang, H. X. *Nat. Nanotechnol.* **2009**, *4*, 377–382.
- (14) Unterreithmeier, Q. P.; Manus, S.; Kotthaus, J. P. *Appl. Phys. Lett.* **2009**, *94*, 263104–3.
- (15) Poggio, M.; Jura, M. P.; Degen, C. L.; Topinka, M. A.; Mamin, H. J.; Goldhaber-Gordon, D.; Rugar, D. *Nat. Phys.* **2008**, *4*, 635.
- (16) Ekinci, K. L.; Yang, Y. T.; Huang, X. M. H.; Roukes, M. L. *Appl. Phys. Lett.* **2002**, *81*, 2253–2255.
- (17) Bargatin, I.; Kozinsky, I.; Roukes, M. L. *Appl. Phys. Lett.* **2007**, *90*, No. 093116.
- (18) Hüttel, A. K.; Steele, G. A.; Witkamp, B.; Poot, M.; Kouwenhoven, L. P.; van der Zant, H. S. J. *Nano Lett.* **2009**, *9*, 2547–2552.
- (19) He, R.; Feng, X. L.; Roukes, M. L.; Yang, P. *Nano Lett.* **2008**, *8*, 1756–1761.
- (20) Truitt, P. A.; Hertzberg, J. B.; Huang, C. C.; Ekinci, K. L.; Schwab, K. C. *Nano Lett.* **2007**, *7*, 120–126.
- (21) Kough, T.; Karabacak, D.; Kim, D. H.; Ekinci, K. L. *Appl. Phys. Lett.* **2005**, *86*, No. 013106.
- (22) Thundat, T.; Finot, E.; Hu, Z.; Ritchie, R. H.; Wu, G.; Majumdar, A. *Appl. Phys. Lett.* **2000**, *77*, 4061–4063.
- (23) Verbridge, S. S.; Parpia, J. M.; Reichenbach, R. B.; Bellan, L. M.; Craighead, H. G. *J. Appl. Phys.* **2006**, *99*, 124304.
- (24) Schmid, S.; Wendlandt, M.; Junker, D.; Hierold, C. *Appl. Phys. Lett.* **2006**, *89*, 163506.
- (25) Grigorenko, A. N.; Roberts, N. W.; Dickinson, M. R.; Zhang, Y. *Nat. Photonics* **2008**, *2*, 365–370.
- (26) Gillespie, D. T. *Am. J. Phys.* **1996**, *64*, 225–240.
- (27) Yurke, B.; Greywall, D. S.; Pargellis, A. N.; Busch, P. A. *Phys. Rev. A* **1995**, *51*, 4211–4229.
- (28) Gonzales, G. *Foundations of Oscillator Circuit Design*; Artech House: Boston, MA, 2007.
- (29) Regal, C. A.; Teufel, J. D.; Lehnert, K. W. *Nat. Phys.* **2008**, *4*, 555.
- (30) Funato, M.; Fujita, S.; Fujita, S. *Appl. Phys. Lett.* **2000**, *77*, 3959–3961.
- (31) Zalalutdinov, M.; Zehnder, A.; Olkhovets, A.; Turner, S.; Sekaric, L.; Ilic, B.; Czaplowski, D.; Parpia, J. M.; Craighead, H. G. *Appl. Phys. Lett.* **2001**, *79*, 695–697.
- (32) Verbridge, S. S.; Bellan, L. M.; Parpia, J. M.; Craighead, H. G. *Nano Lett.* **2006**, *6*, 2109–2114.

Nonlinear switching dynamics in a nanomechanical resonator

Quirin P. Unterreithmeier,^{*} Thomas Faust, and Jörg P. Kotthaus

Fakultät für Physik and Center for NanoScience (CeNS), Ludwig-Maximilians-Universität, Geschwister-Scholl-Platz 1, D-80539 München, Germany

(Received 26 April 2010; published 7 June 2010)

We report studies on the nonadiabatic time evolution of a nonlinear resonator subject to short and intense resonant RF actuation. We are able to quantitatively model the experimental data using a Duffing oscillator. Applying suitably chosen RF pulses, we demonstrate active switching between the two stable states of a Duffing oscillator on short time scales, well below the relaxation time.

DOI: [10.1103/PhysRevB.81.241405](https://doi.org/10.1103/PhysRevB.81.241405)

PACS number(s): 85.85.+j, 05.45.-a, 62.25.-g

The oscillatory response of nonlinear systems exhibits characteristic phenomena such as multistability,¹ discontinuous jumps,^{2,3} and hysteresis.³ These can be utilized in applications leading, e.g., to precise frequency measurement,⁴ mixing,⁵ memory elements,^{6,7} reduced noise characteristics in an oscillator,⁸ or signal amplification.⁹⁻¹² Approaching the quantum regime,¹³ concepts have been proposed that enable low backaction measurement techniques¹¹ or facilitate the visualization of quantum mechanical effects.¹⁴

Nanoelectromechanical systems (NEMS) have been established as excellent devices to explore nonlinear dynamical behavior, as they exhibit high mechanical quality (Q) factors,^{15,16} fast response times,¹⁷ and fairly low drift,¹ and can be easily excited into the nonlinear regime.¹ Here we study the time-dependent response of NEMS resonators in the nonlinear regime aiming at a more detailed understanding of the dynamics. Complementary to previous investigations that concentrated on phenomena arising near the onset of bistability,^{1,4,9} we present experiments that yield insight into the time evolution of the mechanical system. As we apply strong pulses, the system moves away from a stationary state and we study its response to this nonadiabatic actuation. The system is thereby highly excited into the nonlinear regime up to ten times the critical amplitude. Please note that the influence of the actuation on the lattice temperature of the beam is negligible.⁴ We employ our extended knowledge to perform fast switchings between the stable states no longer bound by relaxation times.

The employed resonator consists of a doubly clamped silicon nitride string of dimensions $35\ \mu\text{m} \times 250\ \text{nm} \times 100\ \text{nm}$ (length, width, and height, respectively) under high tensile stress, leading to high mechanical Q factors.¹⁸ In vacuum and at room temperature, we electrically excite the resonator at RF frequencies employing dielectric gradient forces provided by suitably located and biased electrodes.^{18,19} Illuminating the resonator with a light emitting diode, we detect the resonant motion by a small on-chip Schottky diode fabricated close to the resonator and serving as a photodetector for the oscillating component of the optical near field as discussed in detail elsewhere.²⁰ As this scheme enables the detection of the resonator's Brownian motion at room temperature we are able to convert the measured signal into absolute displacement. The nonlinear resonator is continuously actuated by the RF output of a network analyzer as depicted in Fig. 1(a).

Applying sufficiently strong excitation amplitudes, the

mechanical response around resonance tends to bend toward higher frequencies as depicted in Fig. 1(b), corresponding to string hardening. This behavior can be quantitatively modeled by solving the so-called Duffing equation,²¹ an extension of the simple harmonic oscillator by a nonlinear term of third order.

$$\ddot{x}(t) + \frac{2\pi f_0}{Q}\dot{x}(t) + (2\pi f_0)^2 x(t) + \alpha_3 x(t)^3 = k \cos[2\pi(f_0 + \sigma)t]. \quad (1)$$

Here, $x(t)$ designates resonator displacement, $f_0=8$ MHz, $Q=1.2 \times 10^5$ its resonance frequency and quality factor; and α_3 is the cubic correction to the linear restoring force. The excitation amplitude is k and its frequency detuning from the mechanical resonance is $\sigma=f-f_0$. We apply a perturbation calculation using the ansatz $x(t)=a(t)\cos[2\pi(f_0+\sigma)t+\gamma(t)]$, with time-dependent displacement amplitude $a(t)$ and phase $\gamma(t)$. This leads to the two coupled equations²¹

$$\begin{aligned} \dot{a}(t) &= -\frac{2\pi f_0 a(t)}{2Q} + \frac{k \sin[\gamma(t)]}{4\pi f_0}, \\ \dot{\gamma}(t) &= 2\pi\sigma - \frac{3\alpha_3 a(t)^2}{16\pi f_0} + \frac{k \cos[\gamma(t)]}{4\pi f_0 a(t)}. \end{aligned} \quad (2)$$

By setting $\dot{a}(t)=0$, $\dot{\gamma}(t)=0$, one arrives at the quasistatic solution $a=a(f)$. This curve can be excellently fitted to the measured data [see Fig. 1(b)], thereby obtaining $\alpha_3=9 \times 10^{26}$ (ms)⁻² as the only additional numerically adjusted parameter. The onset of bistability, at which the first and second derivative of the amplitude with respect to f diverge [$\partial a/\partial f=\infty$, $\partial^2 a/(\partial f)^2=\infty$] is called critical displacement. Throughout this work, all displacements $a(t)$ are given in units normalized to this critical displacement, it applies $a_c=4\sqrt{2\pi f_0}/(3^{3/4}\sqrt{\alpha_3 Q})=6$ nm (half peak-to-peak), the corresponding critical actuation amplitude is $k_c=150$ ms⁻².

Figure 1(c) shows the calculated displacement response of the resonator when actuated with an excitation amplitude that is ten times larger than the critical actuation leading to the critical displacement a_c . In the following, we always continuously excite our system $\sigma=1$ kHz above resonance, well in the bistable regime. The two stable oscillatory amplitudes are marked as blue dots in Fig. 1(c).

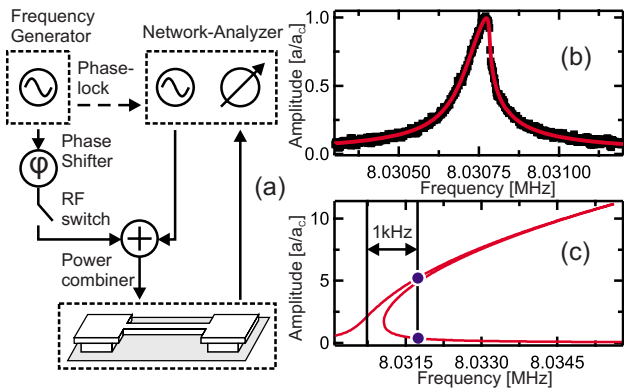


FIG. 1. (Color online) *Setup and quasistatic response*: (a) schematic setup, a nanomechanical resonator is continuously actuated in the nonlinear regime using the RF output of a network analyzer; additional RF pulses of the same frequency are provided by a frequency generator that is phase-locked to the network analyzer; the output of the frequency generator can be adjusted to any phase φ with respect to the continuous actuation; an RF switch defines short RF pulses. The resonator's oscillatory state, given by its displacement amplitude a and phase γ , is recorded by a nearby photodiode and the network analyzer. (b) Quasistatic response to continuous actuation near the onset of bistability, measurement (black) and fit (red/gray) using a solution of the Duffing equation; the displacement amplitude a is given in units of the critical displacement a_c , marking the onset of bistability. (c) Calculated response when actuating ten times the critical driving amplitude. At an actuation frequency f 1 kHz above resonance f_0 , two stable oscillation amplitudes exist, marked with blue/dark gray dots; this actuation is used for all following measurements.

To gain insight into the dynamical behavior of our system, we measure the relaxation toward one of these stable points of the continuously driven string after additional pulsed excitation. The pulsed excitation is provided by the output of a frequency generator that is phase-locked to the network analyzer and operates at the same frequency f as the continuous drive. The phase of the frequency generator's signal can be adjusted to any phase φ with respect to the continuous drive as sketched in Fig. 1(a). To avoid confusion, we always specify the two phases with their respective symbol γ or φ in the ongoing text. An RF switch serves to define RF pulses of adjustable duration.

Any nonstationary resonator state [defined by its displacement amplitude a and phase γ referred to the continuous drive; or equivalently by its in-phase $[a \cos(\gamma)]$ and out-of-phase $[a \sin(\gamma)]$ amplitude component] will converge toward either of the two stable states. This convergence divides the resonator's phase space into two basins of attraction,^{1,21} as depicted in Fig. 2(a) as black and white regions, obtained by numerically integrating Eqs. (2). To test this simulated behavior experimentally, we apply the described short and intense RF pulse that excites the oscillator away from the stable state. Immediately after switching off this pulse, we start recording the resonator state with a sampling rate of 100 kHz. Depending on amplitude, duration, and phase φ of the pulsed excitation, the resonator's dynamic state starts in either the white or black region of phase space directly after excitation and relaxes in a spiraling motion toward either of

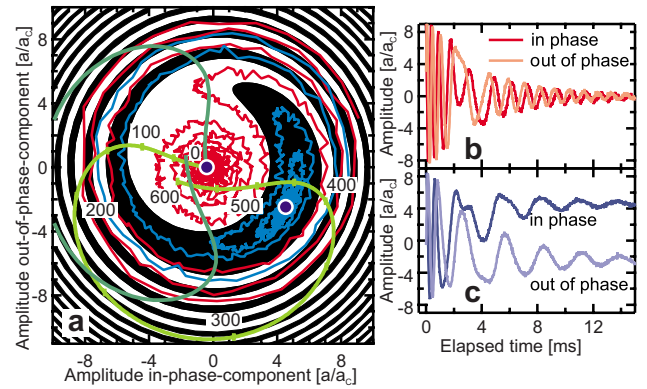


FIG. 2. (Color online) *Time evolution of the resonator state*: (a) the resonator's phase space is shown parametrized by the in $[a \cos(\gamma)]$ and out-of-phase $[a \sin(\gamma)]$ components of the oscillatory displacement. Because of the nonlinear actuation, two stable points exist (blue/dark gray dots), each having its (calculated) basin of attraction (black/white: high/low displacement amplitude). The displayed traces (red/gray and blue/dark gray lines) show the measured relaxation of an oscillatory state after being excited to an amplitude $a \approx 8a_c$ for two different excitation phase φ settings. (b) and (c) display the same relaxation process versus time, the trace color corresponds to (a). The smooth green curves in (a) show the calculated time evolution during the application of an RF pulse of phases $\varphi=262^\circ$, 172° (light and dark curve, respectively) and an amplitude 18-fold larger than the continuous actuation starting from the lower stable state; the displayed time values are given in μs .

the stable states staying within the respective region of phase space as theoretically predicted. In Fig. 2(a) two measured traces of such a relaxation differing in the phase φ of the previously applied RF pulse are plotted in phase space and show excellent agreement with theory. Figures 2(b) and 2(c) display the evolution with time, showing fast dynamics for high amplitudes. Eventually, the state oscillates around either of the stable points with constant frequency.

We intend to utilize the pulses to controllably switch between the stable points, therefore we apply an indirect measurement scheme to explore the nonadiabatic time evolution during strong pulse excitation. Such an indirect scheme is needed because electric crosstalk prevents a direct measurement of the resonator's state during the strong RF pulses. To predict the action of the RF pulse excitation in addition to the continuous drive, the green curves shown in Fig. 2(a) display the calculated mechanical response to a pulse excitation amplitude of $k_{\text{Pulse}} \approx 27 \times 10^3 \text{ ms}^{-2}$ corresponding to 18 times the continuous drive. Both curves start in the lower stable state, they differ in the phase φ of the applied pulse and are obtained by numerically time integrating Eqs. (2). As can be inferred from Fig. 2(a), we consecutively cross the two basins of attraction. Thereby, any resonator state with an amplitude lower than $\approx 10a_c$ can be addressed by suitably choosing the pulse phase and duration with the given pulse amplitude.

In the experiment, the oscillator is prepared in its lower stable state by subsequently switching off and on the continuous actuation. We then apply a short RF pulse with the same excitation amplitude as in the above calculation. After

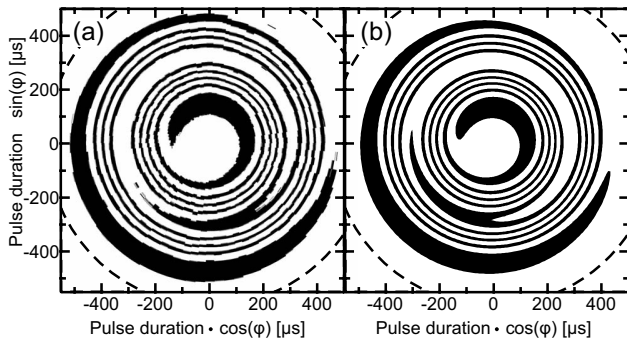


FIG. 3. Time evolution during the application of an RF pulse: (a) measured final state (black/white: high/low displacement amplitude) after the application of RF pulses causing a nonadiabatic response as shown in Fig. 2, systematically varied in duration and phase φ and plotted in polar coordinates. (b) Simulation of the measurement employing no fit parameters.

waiting several relaxation times given by $Q/(2\pi f_0)$, the attained stable state is recorded in displacement amplitude a and phase γ . We repeat this sequence, restore the lower stable state and systematically vary the length of the RF pulse and its phase φ ; the excitation amplitude is always the same. Thereby we implicitly map the end point of the green traces as shown in Fig. 2(a) and obtain the spirals in Fig. 3(a). This measured result is in excellent agreement with the calculation shown in Fig. 3(b), employing no fit parameters. The range of achieved displacement amplitudes extends those of previous measurements¹ to values of ten times the critical amplitude a_c . We can deduce that the perturbation solution describing the time evolution Eqs. (2) remains accurate at least up to displacements that correspond to ten times the critical amplitude a_c . This demonstrates that the dynamics of a strongly driven nanomechanical resonator can still be accurately described by a perturbation solution of the Duffing equation, therefore serving as model system to study nonlinear dynamics^{22,23} well in the nonadiabatic regime.

Our quantitative understanding of the experiment enables us to numerically calculate the parameters needed in order to access any desired resonator state. In particular we are able to switch directly between the two stable states. We thus extend previous concepts^{6,7} of switching limited by the relaxation time scale $Q/(2\pi f_0)$ to active switching via RF pulses suitably chosen in amplitude, phase, and length. Figure 4(a) shows two consecutive switching events; during the 80- μ s-long RF pulses electric crosstalk produces overshoots partially exceeding the displayed range of displacement amplitudes. The nearly constant amplitude values highlighted by gray areas reflect the respective stable state of the bistable system. Note that the approach toward these constant amplitudes occurs on a time scale of less than 1 ms and only reflects the limited dynamics of the electronic measurement setup in contrast to the mechanical relaxation behavior studied in Figs. 2(b) and 2(c).

Since we can pulse toward either of the targeted stable states with high precision in phase space, we can switch between the stable states with a high repetition rate. Any systematic deviation would add up, eventually preventing controllable switching. Figure 4(b) shows ten consecutive

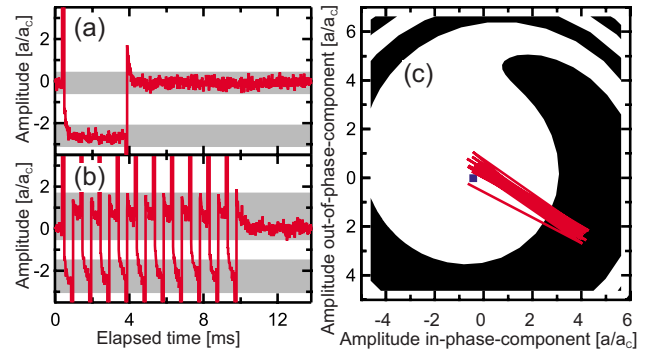


FIG. 4. (Color online) Switching between the stable points: (a) Out-of-phase component of the measured resonator displacement $a \sin(\gamma)$; the part of nearly constant amplitude (highlighted by the gray background) corresponds to the stable points; the spikes are a result of electric crosstalk when applying short RF pulses suitably chosen to directly switch between these states and do not correspond to displacement amplitudes. (b) Consecutive switching; ten pairs of switching events are shown; the duration of one pulse is approximately 80 μ s, the repetition rate of the pairs is 1 kHz. Because of the finite measurement bandwidth and electric crosstalk there is a systematic deviation compared to (a). (c) The same measurement displayed in phase space.

switching events within ten milliseconds each going back and forth between the two stable states. This corresponds to a demonstrated operating speed of 2 kHz. The applied pulse duration of 80 μ s of a single pulse allows operation speeds of approximately 11 kHz. In Fig. 4(c), we plot the same switching sequence in phase space. The image shows some systematic deviation of the measured traces with respect to the predicted stable states occurring immediately after the application of an RF pulse. This deviation is a result of the electric crosstalk and the finite bandwidth of the measurement setup. The experimentally chosen pulse durations deviate by less than 4% from the ones that were predicted theoretically.

The duration of the switching pulses corresponds here to approximately 1000 cycles of oscillation. This is significantly less than the number of oscillations required for the relaxation from an excited to a stable state corresponding to several times the quality factor of here $Q=1.2 \times 10^5$. Although being advantageous in terms of power consumption, a high-quality factor prevents fast switching in passive schemes, such as a sudden parameter change⁷ or the introduction of a weak external perturbation.⁶ Our scheme overcomes this limitation and achieves a four orders of magnitude improvement in speed when compared to these previous results.

It remains to be shown whether any logic or memory based on nanomechanical elements will play a significant role in the future. To achieve an operating speed of 100 MHz, another improvement of switching duration of 10^4 is required. As resonators with GHz resonance frequencies¹⁷ and high-quality factors¹⁶ have been demonstrated, this goal is not principally out of reach.

In conclusion, we quantitatively study the dynamical oscillatory response of a nonlinear nanomechanical resonator

in bistable configuration. The application of short RF pulses allows us to modify the resonator state at will. We utilize these pulses to highly excite the resonator. The measured results can be excellently modeled using a combination of perturbation calculation and numerical integration. We thereby directly confirm the accuracy of this model calculation to describe nonlinear dynamics.^{14,23} Our quantitative understanding allows us to predict and generate RF pulse

parameters that directly switch between the two stable states repeatedly.

Financial support by the Deutsche Forschungsgemeinschaft under Project No. Ko 416/18 as well as the German Excellence Initiative via the Nanosystems Initiative Munich (NIM) and LMUexcellent is gratefully acknowledged. We thank E. M. Weig for critically reading the manuscript.

*quirin.unterreithmeier@physik.uni-muenchen.de

- ¹I. Kozinsky, H. W. C. Postma, O. Kogan, A. Husain, and M. L. Roukes, *Phys. Rev. Lett.* **99**, 207201 (2007).
- ²W. J. Venstra and H. S. J. van der Zant, *Appl. Phys. Lett.* **93**, 234106 (2008).
- ³G. Gabrielse, H. Dehmelt, and W. Kells, *Phys. Rev. Lett.* **54**, 537 (1985).
- ⁴J. S. Aldridge and A. N. Cleland, *Phys. Rev. Lett.* **94**, 156403 (2005).
- ⁵A. Erbe, H. Krommer, A. Kraus, R. H. Blick, G. Corso, and K. Richter, *Appl. Phys. Lett.* **77**, 3102 (2000).
- ⁶I. Mahboob and H. Yamaguchi, *Nat. Nanotechnol.* **3**, 275 (2008).
- ⁷D. N. Guerra, M. Imboden, and P. Mohanty, *Appl. Phys. Lett.* **93**, 033515 (2008).
- ⁸D. S. Greywall, B. Yurke, P. A. Busch, A. N. Pargellis, and R. L. Willett, *Phys. Rev. Lett.* **72**, 2992 (1994).
- ⁹R. Almog, S. Zaitsev, O. Shtempluck, and E. Buks, *Appl. Phys. Lett.* **90**, 013508 (2007).
- ¹⁰R. L. Badzey and P. Mohanty, *Nature (London)* **437**, 995 (2005).
- ¹¹I. Siddiqi, R. Vijay, F. Pierre, C. M. Wilson, M. Metcalfe, C. Rigetti, L. Frunzio, and M. H. Devoret, *Phys. Rev. Lett.* **93**, 207002 (2004).
- ¹²R. Almog, S. Zaitsev, O. Shtempluck, and E. Buks, *Phys. Rev. Lett.* **98**, 078103 (2007).
- ¹³G. Anetsberger, O. Arcizet, Q. P. Unterreithmeier, R. Riviere, A. Schliesser, E. M. Weig, J. P. Kotthaus, and T. J. Kippenberg, *Nat. Phys.* **5**, 909 (2009).
- ¹⁴I. Katz, A. Retzker, R. Straub, and R. Lifshitz, *Phys. Rev. Lett.* **99**, 040404 (2007).
- ¹⁵S. S. Verbridge, H. G. Craighead, and J. M. Parpia, *Appl. Phys. Lett.* **92**, 013112 (2008).
- ¹⁶A. K. Hüttel, G. A. Steele, B. Witkamp, M. Poot, L. P. Kouwenhoven, and H. S. J. van der Zant, *Nano Lett.* **9**, 2547 (2009).
- ¹⁷X. M. Henry Huang, C. A. Zorman, M. Mehregany, and M. L. Roukes, *Nature (London)* **421**, 496 (2003).
- ¹⁸Q. P. Unterreithmeier, E. M. Weig, and J. P. Kotthaus, *Nature (London)* **458**, 1001 (2009).
- ¹⁹S. Schmid, M. Wendlandt, D. Junker, and C. Hierold, *Appl. Phys. Lett.* **89**, 163506 (2006).
- ²⁰Q. P. Unterreithmeier, T. Faust, S. Manus, and J. P. Kotthaus, *Nano Lett.* **10**, 887 (2010).
- ²¹A. H. Nayfeh and D. T. Mook, *Nonlinear Oscillations* (Wiley, New York, 1995).
- ²²B. Ritchie and C. M. Bowden, *Phys. Rev. A* **32**, 2293 (1985).
- ²³F. Brennecke, S. Ritter, T. Donner, and T. Esslinger, *Science* **322**, 235 (2008).

Damping of Nanomechanical Resonators

Quirin P. Unterreithmeier,* Thomas Faust, and Jörg P. Kotthaus

*Fakultät für Physik and Center for NanoScience (CeNS), Ludwig-Maximilians-Universität,
Geschwister-Scholl-Platz 1, D-80539 München, Germany*

(Received 9 March 2010; published 9 July 2010)

We study the transverse oscillatory modes of nanomechanical silicon nitride strings under high tensile stress as a function of geometry and mode index $m \leq 9$. Reproducing all observed resonance frequencies with classical elastic theory we extract the relevant elastic constants. Based on the oscillatory local strain we successfully predict the observed mode-dependent damping with a single frequency-independent fit parameter. Our model clarifies the role of tensile stress on damping and hints at the underlying microscopic mechanisms.

DOI: 10.1103/PhysRevLett.105.027205

PACS numbers: 85.85.+j, 46.40.Ff, 62.40.+i

The resonant motion of nanoelectromechanical systems has received a lot of recent attention. Their large frequencies, low damping, i.e., high mechanical quality factors, and small masses make them equally important as sensors [1–4] and for fundamental studies [3–9]. In either case, low damping of the resonant motion is very desirable. Despite significant experimental progress [10,11], a satisfactory understanding of the microscopic causes of damping has not yet been achieved. Here we present a systematic study of the damping of doubly-clamped resonators fabricated out of prestressed silicon nitride leading to high mechanical quality factors [10]. Reproducing the observed mode frequencies applying continuum mechanics, we are able to quantitatively model their quality factors by assuming that damping is caused by the local strain induced by the resonator's displacement. We thereby deduce that the high quality factors of strained nanosystems can be attributed to the increase in stored elastic energy rather than a decrease in energy loss. Considering various microscopic mechanisms, we conclude that the observed damping is most likely dominated by dissipation via localized defects uniformly distributed along the resonator.

We study the oscillatory response of nanomechanical beams fabricated from high stress silicon nitride (SiN). A released doubly-clamped beam of such a material is therefore under high tensile stress, which leads to high mechanical stability [12] and high mechanical quality factors [10]. Such resonators therefore have been widely used in recent experiments [6,9]. Our sample material consists of a silicon substrate covered with 400 nm thick silicon dioxide serving as sacrificial layer and a $h = 100$ nm thick SiN device layer. Using standard electron beam lithography and a sequence of reactive ion etch and wet-etch steps, we fabricate a series of resonators having lengths of $35/n \mu\text{m}$, $n = \{1, \dots, 7\}$ and a cross section of $100 \times 200 \text{ nm}^2$ as displayed in Figs. 1(a) and 1(b). Since the respective resonance frequency is dominated by the large tensile stress [10,13], this configuration leads to resonances of the fundamental modes that are approximately equally

spaced in frequency. Suitably biased gold electrodes processed beneath the released SiN strings actuate the resonators via dielectric gradient forces to perform out-of-plane oscillations, as explained in greater detail elsewhere [12]. The length and location of the gold electrodes is properly chosen to be able to also excite several higher order modes of the beams. The experiment is carried out at room temperature in a vacuum below 10^{-3} mbar to avoid gas friction.

The displacement is measured using an interferometric setup that records the oscillatory component of the reflected light intensity with a photodetector and network analyzer [12,14]. The measured mechanical response around each resonance can be fitted using a Lorentzian line shape as exemplarily seen in the inset of Fig. 2. The thereby obtained values for the resonance frequency f and

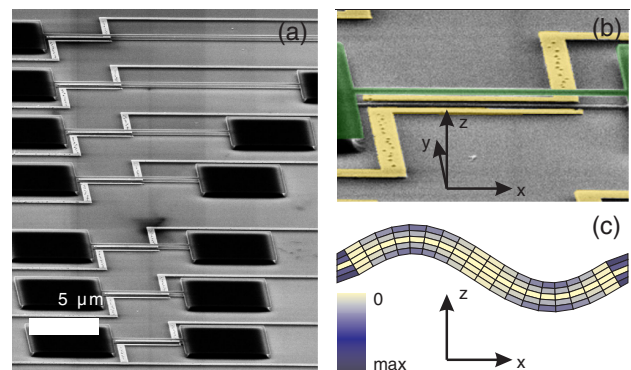


FIG. 1 (color online). *Setup and geometry.* (a) Scanning electron microscope picture of our sample; the lengths of the investigated nanomechanical silicon nitride strings are $35/n \mu\text{m}$, $n = \{1, \dots, 7\}$; their widths and heights are 200 nm and 100 nm, respectively. (b) Zoom-in of (a) the resonator (highlighted in green [dark gray]) is dielectrically actuated by the nearby gold electrodes (yellow [light gray]); its displacement is recorded with an interferometric setup. (c) Schematic mode profile and absolute value of the resulting strain distribution (color coded) of the second harmonic.

quality factor Q for all studied resonators and observed modes are displayed in Fig. 2 (filled circles). In order to reproduce the measured frequency spectrum, we apply standard beam theory (see, e.g., [15]). Without damping, the differential equation describing the spatial dependence of the displacement for a specific mode m of beam n $u_{n,m}[x]$ at frequency $f_{n,m}$ writes (with $\rho = 2800 \text{ kg/m}^3$ being the material density [16]; E_1, σ_0 are the (unknown) real Young's modulus and built-in stress, respectively):

$$\frac{1}{12}E_1h^2\frac{\partial^4}{\partial x^4}u_{n,m}[x] - \sigma_0\frac{\partial^2}{\partial x^2}u_{n,m}[x] - \rho(2\pi f_{n,m})^2u_{n,m}[x] = 0 \quad (1)$$

Solutions of this equation have to satisfy the boundary conditions of a doubly-clamped beam (displacement and its slope vanish at the supports ($u_{n,m}[\pm l/(2n)] = (\partial/\partial x)u_{n,m}[\pm l/(2n)] = 0$, l/n : beam length)). These conditions lead to a transcendental equation that is numerically solved to obtain the frequencies $f_{n,m}$ of the different modes.

The results are fitted to excellently reproduce the measured frequencies, as seen in Fig. 2 (hollow squares). One thereby obtains as fit parameters the elastic constants of the microprocessed material $E_1 = 160 \text{ GPa}$, $\sigma_0 = 830 \text{ MPa}$, in good agreement with previously published measurements [13].

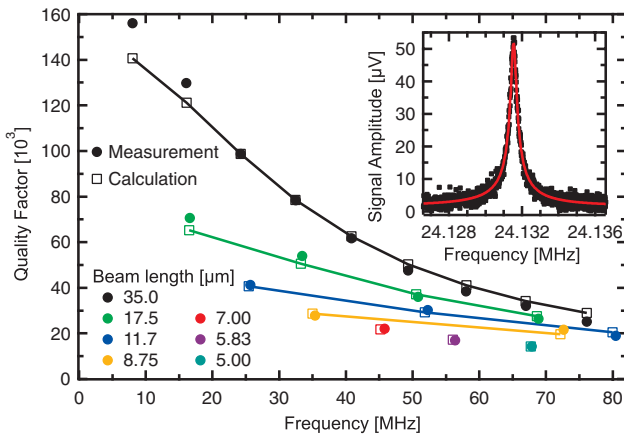


FIG. 2 (color online). *Resonance frequency and mechanical quality factor.* The harmonics of the nanomechanical resonator show a Lorentzian response (exemplary in the inset). Fitting yields the respective frequency and mechanical quality factor. The main figure displays these values for several harmonics (same color) of different beams as indicated by the color. To reproduce the resonance frequencies, we fit a continuum model to the measured frequencies. We thereby retrieve the elastic constants of our (processed) material, namely, the built-in stress $\sigma_0 = 830 \text{ MPa}$ and Young's modulus $E_1 = 160 \text{ GPa}$. From the displacement-induced, mode-dependent strain distribution, we calculate (except for an overall scaling) the mechanical quality factors. Calculated frequencies and quality factors are shown as hollow squares, the responses of the different harmonics of the same string are connected.

For each harmonic, we now are able to calculate the strain distribution within the resonator induced by the displacement $u[x]$ and exemplarily shown in Fig. 1(c). The measured dissipation is closely connected to this induced strain $\epsilon[x, z, t] = \epsilon[x, z]\exp[i2\pi ft]$. As in the model originally discussed by Zener [17] we now assume also for our case of a statically prestressed beam that the displacement-induced strain and the accompanying oscillating stress $\sigma[x, z, t] = \sigma[x, z]\exp[i2\pi ft]$ are not perfectly in phase; this can be expressed by a Young's modulus $E = E_1 + iE_2$ having an imaginary part. The relation reads again $\sigma[x, z] = (E_1 + iE_2)\epsilon[x, z]$. During one cycle of oscillation $T = 1/f$, a small volume δV of length s and cross section A thereby dissipates the energy $\Delta U_{\delta V} = As\pi E_2 \epsilon^2$. The total loss is obtained by integrating over the volume of the resonator.

$$\Delta U_{n,m} = \int_V dV \Delta U_{\delta V} = \pi E_2 \int_V dV \epsilon_{n,m}[x, z]^2 \quad (2)$$

The strain variation and its accompanying energy loss can be separated into contributions arising from overall elongation of the beam and its local bending. It turns out that here the former is negligible, despite the fact that the elastic energy is dominated by the elongation of the string, as discussed below. To very high accuracy we obtain for the dissipated energy $\Delta U_{n,m} \approx \pi/12E_2wh^3 \int_1 dx (\partial^2/(\partial x)^2 u_{n,m})^2$. A more rigorous derivation can be found in the supplementary information [18]. The total energy depends on the spatial mode [through $\epsilon_{n,m}$, see exemplary Fig. 1(c)] and therefore strongly differs for the various resonances. To obtain the quality factor, one has to calculate the stored energy, e. g., by integrating the kinetic energy $U_{n,m} = \int_1 dx A\rho(2\pi f_{n,m})^2 u_{n,m}[x]^2$. The overall mechanical quality factor is $Q = 2\pi U_{n,m}/\Delta U_{n,m}$. A more detailed derivation can be found in [18].

Assuming that the unknown value of the imaginary part E_2 of the elastic modulus is independent of resonator length and harmonic mode, we are left with one fit parameter E_2 to reproduce all measured quality factors and find excellent agreement (Fig. 2, hollow squares). We therefore successfully model the damping of our nano-resonators by postulating a frequency-independent mechanism caused by local strain variation. We wish to point out that the quality factor of, e.g., the second harmonic of a particular beam is significantly higher if compared to the fundamental one of a shorter beam with the same frequency. This can be understood by the fact that the maximum strain and thus local dissipation occurs near the clamping points and a higher harmonic has less clamping points per antinode [see Fig. 1(c)].

Allowing E_2 to depend on frequency, the accordance gets even better, as discussed in detail in [18].

We now discuss the possible implications of our findings, considering at first the cause of the high quality factors in overall prestressed resonators and then the compatibility of our model with different microscopic damping

mechanisms. In a relaxed beam, the elastic energy is stored in the flexural deformation and becomes for a small test volume $U_{\delta V} = 1/2AsE_1\epsilon^2$. In the framework of a Zener model, as employed here, this result is proportional to the energy loss [see Eq. (2)] and thus yields a frequency-independent quality factor $Q = E_1/E_2$ for the unstressed beam. In accordance with this finding, Ref. [10] reports a much weaker dependence of quality factor on resonance frequency, in strong contrast with the behavior of their stressed beams.

Similar as in the damping model, the total stored elastic energy in a beam can be very accurately separated into a part connected to the bending and a part coming from the overall elongation. The latter is proportional to the prestress σ_0 and vanishes for relaxed beams, refer to [18] for details. Assuming a constant $E = E_1 + iE_2$, Fig. 3 displays the calculation of the elastic energy and the quality factor for the fundamental mode of our longest ($l = 35 \mu\text{m}$) beam as a function of overall built-in stress σ_0 . The total elastic energy is increasingly dominated by the displacement-induced elongation $U_{\text{elong}} = 1/2\sigma_0wh \int_1 dx(\partial/(\partial x)u[x])^2$. In contrast the bending energy $U_{\text{bend}} = 1/24E_1wh^3 \int_1 dx(\partial^2/(\partial x)^2u[x])^2$, which in our model is proportional to the energy loss, is found to increase much slower with σ_0 . Thus one expects Q to increase with σ_0 , a finding already discussed by Schmid and Hierold for micromechanical beams [19]. However, their model assumes the simplified mode profile of a stretched string and can not explain the larger quality factors of higher harmonics when compared to a fundamental resonance of the same frequency. Including beam stiffness, our model can fully explain the dependence of frequency and damping on length and mode index, as reflected in Fig. 2. It also explains the initially surprising finding [20] that amorphous silicon nitride resonators exhibit high quality factors when stretched whereas having Q

factors in the relaxed state that reflect the typical magnitude of internal friction found to be rather universal in glassy materials [21]. More generally we conclude that the increase in mechanical quality factors with increasing tensile stress is not bound to any specific material.

Since the resonance frequency is typically easier to access in an experiment, we plot the quality factor vs corresponding resonance frequency in Fig. 3(b), with both numbers being a function of stress. The resulting relation of quality factor on resonance frequency is (except for very low stress) almost linear; experimental results by another group can be seen to agree well with this finding [22]. In addition, we show in [18] that although the energy loss per oscillation increases with applied stress, the line-width of the mechanical resonance decreases.

We will now consider the physical mechanisms that could possibly contribute to the observed damping. As explained in greater detail in [18], we can safely neglect dampings that are intrinsic to any (bulk) system, namely, clamping losses [23,24], thermoelastic damping [25,26] and Akhiezer damping [26,27], since the corresponding model calculations all predict damping constants significantly smaller than the ones observed.

Therefore, we would like to discuss the influence of localized (defect) states. Mechanisms with discrete relaxation rates will exhibit damping maxima whenever the oscillation frequency matches the relaxation rate [25,26,28]. As our model however is based on a frequency-independent loss mechanism, we therefore conclude that a broad range of states is responsible for the observed damping. This assumption is consistent with a model calculation dealing with the influence of two-level systems on acoustic waves [29] at high temperatures. There, the strain modulates the energy separation of the two states and thereby excites the system out of thermal equilibrium; the subsequent relaxation causes the energy loss. In addition, published quality factors of relaxed silicon nitride nanoresonators [20] cooled down to liquid helium temperature display quality factors that are well within the typical range of amorphous bulk materials [21], therefore the observed damping mechanism can be assumed to reduce to the concept of two-level systems at low temperatures. Moreover, on a different sample chip we measured a set of resonators showing quality factors that are uniformly decreased by a factor of approximately 1.4 compared to the data presented in Fig. 2; the corresponding data are presented in [18]. Their response can still be quantitatively modeled resulting in an increased imaginary part of Young's modulus E_2 . We attribute this reduction in quality factor to a nonoptimized RIE-etch step, that leads to an increased density of defect states in the near-surface region of the resonator. In contrast, the above mentioned intrinsic mechanisms are not expected to be influenced by such processing.

We wish to point out some limitations of our simple model description. One is that the above stated simplification to local two-level systems cannot be rigorously ap-

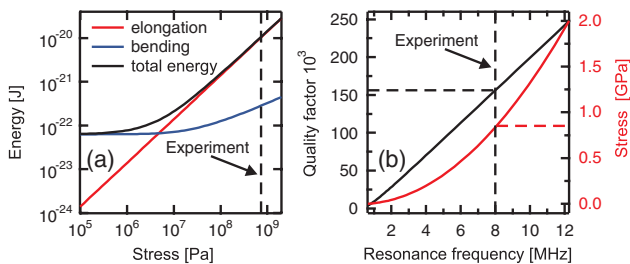


FIG. 3 (color online). *Elastic energy and mechanical quality factor of the beam in dependence of stress.* (a) The elastic energies of the fundamental mode of the beam with $l = 35 \mu\text{m}$ are displayed vs applied overall stress separated into the contributions resulting from the overall elongation and the local bending. The dashed line marks the strain of the experimentally studied resonator $\sigma_0 \approx 830 \text{ MPa}$, there the elongation term dominates noticeably. (b) Quality factor and frequency are calculated for varying stress σ_0 . In order to compare the calculation with other published results, quality factor and stress are displayed vs resulting frequency.

plied at elevated temperatures as the concept of two-level systems should be replaced by local excitable systems. The other is that our assumption of a damping mechanism via localized defects distributed uniformly along the resonator cannot differentiate between surface and volume losses (see [18]). In fact, measurements performed on beams with larger width exhibit slightly higher quality factors pointing toward a contribution of surface defects as does the effect of sample processing discussed above, a well-known observation in micro- or nanoresonators, see e.g. [30,31]. At present we cannot conclude on the microscopic nature of the defect states implicitly assumed in our model. These could reflect the amorphous nature of the SiN resonator but also be influenced by near-surface modification.

In conclusion, we systematically studied the transverse mode frequencies and quality factors of prestressed SiN nanoscale beams. Implementing continuum theory, we reproduce the measured frequencies varying with beam length and mode index over an order of magnitude. Assuming that damping is caused by local strain variations induced by the oscillation, independent of frequency, enables us to calculate the observed quality factors with a single interaction strength as free parameter. We thus identify the unusually high quality factors of prestressed beams as being primarily caused by the increased elastic energy rather than a decrease in damping rate. Several possible damping mechanisms are discussed; because of the observed nearly frequency independent damping parameter E_2 , we attribute the mechanism to interaction of the strain with local defects of not yet identified origin. One therefore expects that defect-free resonators exhibit even larger quality factors, as recently demonstrated for ultraclean carbon nanotubes [11].

Financial support by the Deutsche Forschungsgemeinschaft via Project No. Ko 416/18, the German Excellence Initiative via the Nanosystems Initiative Munich (NIM) and LMUexcellent as well as the Future and Emerging Technologies programme of the European Commission, under the FET-Open project QNEMS (233992) is gratefully acknowledged. We would like to thank Florian Marquardt and Ignacio Wilson-Rae for stimulating discussions.

*unterreithmeier@physik.uni-muenchen.de

- [1] K. Jensen, K. Kim, and A. Zettl, *Nature Nanotech.* **3**, 533 (2008).
- [2] B. Lassagne, D. Garcia-Sanchez, A. Aguasca, and A. Bachtold, *Nano Lett.* **8**, 3735 (2008).
- [3] M. D. LaHaye, J. Suh, P. M. Echternach, K. C. Schwab, and M. L. Roukes, *Nature (London)* **459**, 960 (2009).
- [4] J. D. Teufel, T. Donner, M. A. Castellanos-Beltran, J. W. Harlow, and K. W. Lehnert, *Nature Nanotech.* **4**, 820 (2009).
- [5] J. S. Aldridge and A. N. Cleland, *Phys. Rev. Lett.* **94**, 156403 (2005).
- [6] T. Rocheleau, T. Ndukum, C. Macklin, J. B. Hertzberg, A. A. Clerk, and K. C. Schwab, *Nature (London)* **463**, 72 (2010).
- [7] M. Li, W. H. P. Pernice, C. Xiong, T. Baehr-Jones, M. Hochberg, and H. X. Tang, *Nature (London)* **456**, 480 (2008).
- [8] S. Etaki, M. Poot, I. Mahboob, K. Onomitsu, H. Yamaguchi, and H. S. J. van der Zant, *Nature Phys.* **4**, 785 (2008).
- [9] M. Eichenfield, R. Camacho, J. Chan, K. J. Vahala, and O. Painter, *Nature (London)* **459**, 550 (2009).
- [10] S. S. Verbridge, J. M. Parpia, R. B. Reichenbach, L. M. Bellan, and H. G. Craighead, *J. Appl. Phys.* **99**, 124304 (2006).
- [11] A. K. Huettel, G. A. Steele, B. Witkamp, M. Poot, L. P. Kouwenhoven, and H. S. J. van der Zant, *Nano Lett.* **9**, 2547 (2009).
- [12] Q. P. Unterreithmeier, E. M. Weig, and J. P. Kotthaus, *Nature (London)* **458**, 1001 (2009).
- [13] Q. P. Unterreithmeier, S. Manus, and J. P. Kotthaus, *Appl. Phys. Lett.* **94**, 263104 (2009).
- [14] N. O. Azak, M. Y. Shagam, D. M. Karabacak, K. L. Ekinici, D. H. Kim, and D. Y. Jang, *Appl. Phys. Lett.* **91**, 093112 (2007).
- [15] W. Weaver, S. P. Timoshenko, and D. H. Young, *Vibration Problems in Engineering* (Wiley, New York, 1990).
- [16] M. G. el Hak, *The MEMS Handbook* (CRC Press, Boca Raton, 2001).
- [17] C. Zener, *Phys. Rev.* **53**, 90 (1938).
- [18] See supplementary material at <http://link.aps.org/supplemental/10.1103/PhysRevLett.105.027205>.
- [19] S. Schmid and C. Hierold, *J. Appl. Phys.* **104**, 093516 (2008).
- [20] D. R. Southworth, R. A. Barton, S. S. Verbridge, B. Ilic, A. D. Fefferman, H. G. Craighead, and J. M. Parpia, *Phys. Rev. Lett.* **102**, 225503 (2009).
- [21] R. O. Pohl, X. Liu, and E. Thompson, *Rev. Mod. Phys.* **74**, 991 (2002).
- [22] S. Verbridge, D. Shapiro, H. Craighead, and J. Parpia, *Nano Lett.* **7**, 1728 (2007).
- [23] Z. Hao, A. Erbil, and F. Ayazi, *Sens. Actuators. A, Phys.* **109**, 156 (2003).
- [24] I. Wilson-Rae, *Phys. Rev. B* **77**, 245418 (2008).
- [25] R. Lifshitz and M. L. Roukes, *Phys. Rev. B* **61**, 5600 (2000).
- [26] A. A. Kiselev and G. J. Iafrate, *Phys. Rev. B* **77**, 205436 (2008).
- [27] A. Akhiezer, *J. Phys. (Moscow)* **1**, 277 (1939).
- [28] A. N. Cleland, *Foundations of Nanomechanics* (Springer, New York, 2003).
- [29] J. Jackle, *Z. Phys.* **257**, 212 (1972).
- [30] J. L. Yang, T. Ono, and M. Esashi, *J. Microelectromech. Syst.* **11**, 775 (2002).
- [31] D. W. Carr, S. Evoy, L. Sekaric, H. G. Craighead, and J. M. Parpia, *Appl. Phys. Lett.* **75**, 920 (1999).

Appendix G

Supporting Information

G.1 Frequency of a pulled string

In this section the upshift in resonance frequency of a string-like oscillator under tensile stress is calculated caused by a uniform loading of the string.

We regard a string-like resonator of length l subject to a tensile force F_σ and a perpendicular and uniform force per length F_L . The displacement is designated $u[x]$; the string is subdivided in rigid segments of length δx , see Fig. G.1.

Regarding small amplitudes, the z -component of the tensile force at the interconnection is $F_z = F_\sigma \sin \alpha \approx F_\sigma u'[x]$. In equilibrium, the sum of the two forces has to equal the external force $F_L \delta x$ (again assuming small amplitudes). It therefore applies:

$$\delta x F_L = F_\sigma (u'[x + \delta x] - u'[x]) \text{ or } u''[x] = u'' = \frac{F_L}{F_\sigma} \quad (\text{G.1})$$

The total elongation of the string can now be calculated by integration:

$$\Delta l = \int_{-l/2}^{l/2} dx (\sqrt{1 + u'^2[x]} - 1) \approx \int_{-l/2}^{l/2} dx \frac{1}{2} u''^2 x^2 = \frac{1}{12} u''^2 l^3 \quad (\text{G.2})$$

For convenience, we now regard the tensile stress instead of force; the elongation increases the tensile stress by $\sigma = \sigma_0 + E \Delta l / l$, the resonance frequency gets thereby shifted by (c : proportionality constant)

$$f = c \sqrt{\sigma} \approx f_0 \left(1 + \frac{1}{2} \frac{\Delta \sigma}{\sigma_0} \right) = f_0 \left(1 + \frac{1}{24} \frac{E l^2}{\sigma_0} \left(\frac{F_L}{A \sigma_0} \right)^2 \right) \quad (\text{G.3})$$

Related considerations concerning a beam rather than a string can be found in Ref. [1].

With the values given in table G.1, the application 20 V leads to a frequency upshift of 5.6 kHz, significantly less than the downshift observed in the experiment.

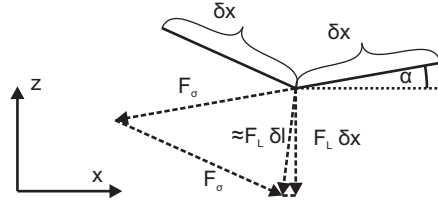


Figure G.1: Forces acting on neighboring segments of a string under tensile stress

designation	symbol	value
resonance frequency	f_0	10 MHz
Young's Modulus	E	160 GPa
prestress	σ_0	830 MPa
force per length	F_L	5 nN/ μm
cross sectional area	A	$0.1 \cdot 0.2 \mu\text{m}^2$

Table G.1: Calculation parameters of the pulled string

G.2 Supplement to Dielectric Actuation

G.2.1 Electrical heat dissipation

The mutual resistance between the on-chip electrodes is measured to be higher than 10 G Ω ; 12 pairs of electrodes are always connected in parallel. With the applied d.c. voltage not exceeding 20 V, this yields a maximum thermal contribution of 4 nW per driving electrode. The incident r.f.-power in these experiments does not exceed 1 mW. The mutual capacitance of the electrodes is simulated to be approximately 1.5 fF. Therefore, the electrical current within the electrodes does not exceed 0.3 μA at 10 MHz. The ohmic resistance of a gold electrode of 30 μm length can be estimated not to exceed several ohms, yielding a local dissipation below 1 pW. Correspondingly, r.f.-heating is insignificant. The thermal conductance of silicon at room temperature is about 150 W/Km. Thus, assuming a near resonator dissipation of 4 nW and a thermal bath in 100 μm distance, this would lead to an increase in temperature of about 1.5 μK and can be neglected.

G.2.2 Electrical sensitivity

In order to increase the sensitivity, the demonstrated direct detection scheme can be replaced with an extended gate architecture incorporating a LC circuit. The change of capacitance of the detection electrodes with mechanical motion is thereby converted into the change of resonance frequency of the circuit. This scheme yields a significantly higher sensitivity, see ref. [2]. Our simulations predict a relative capacitance change with mechanical motion of the beam of approximately

$1/C \cdot \partial C/\partial d \approx 10^{-4}/\text{nm}$. We assume that the added circuitry is designed carefully, avoiding extra capacitance. For a LC resonance frequency of $2\pi \cdot 5 \text{ GHz}$, this would correspond to a frequency shift of $2\pi \cdot 50 \text{ kHz/nm}$. Comparing these values to those published recently [2], a sensitivity close to $5 \text{ fm}/\sqrt{\text{Hz}}$ should be obtainable. However, as this measurement setup includes superconducting striplines, low temperature will be required to greatly improve the sensitivity.

G.2.3 Long-term drift of the resonance frequency

At d.c. bias of several volts all resonators that were investigated showed long-term drifts of the resonance frequency in the kHz regime. Application of a bias $V_{\text{d.c.}} \neq 0$ results in a downshift in frequency while not strongly affecting the resonant amplitude, independent of the sign of the bias. The long time constant observed in the response is unlikely to result from simple heating. Charging can explain qualitatively the above observation if the dominant charge accumulates beneath the resonator, where it causes a frequency shift without significantly changing the amplitude. We therefore investigated the influence of the thickness of the residual silicon dioxide layer that is left of the sacrificial layer after underetching the resonator and that is used to insulate the transduction electrodes, but found little influence (see Fig. G.2). Further investigations to yield a better understanding of these drift phenomena, and in particular their temperature dependence, are currently in preparation. In the results presented in the main text we minimised these long term drifts by either measuring on a sufficiently short time scale or by periodically reversing the d.c. bias (e.g. in Fig. 3a in the main paper).

G.3 Nonlinear characteristics of a vibrating prestressed string

The variables used in this section are the same as in section G.1. The calculation is independent of the harmonic, we therefore regard the spatial profile of the fundamental mode of a vibrating string; it is given by [1] (a : peak amplitude):

$$u[x] = a \cos(x/(2l)) \quad (\text{G.4})$$

The elongation is calculated by integrating over the length; the result is expanded in a

$$\Delta l = 2 \int_{-l/2}^{l/2} dx (\sqrt{1 + u'[x]^2}) = l \left(\frac{\pi^2}{4} \frac{a^2}{l^2} - \frac{3\pi^4}{64} \frac{a^4}{l^4} + o[(a/l)^6] \right) \quad (\text{G.5})$$

A change in beamlength causes a change in energy U ; it applies

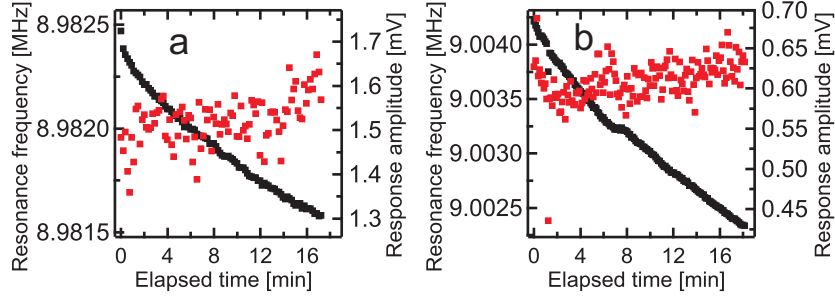


Figure G.2: **Long-term drift of the resonance frequency for two samples.** Electrostatically induced drift of the resonator eigenfrequency and amplitude. The bias voltage is abruptly changed from 0 to -5 V. Subsequently the frequency response is measured repeatedly. With elapsing time, the eigenfrequency (black dots) shows a drift to lower values whereas there is almost no overall change in the amplitude (red dots). To investigate the influence of the silicon dioxide insulating layer, devices with different thickness are compared. **a**, Silicon dioxide sacrificial layer completely removed. The insulating layer has the typical thickness of natural oxides. **b**, Residual silicon dioxide layer with a thickness of about 100 nm, which is about 25 % of the initial sacrificial layer. This device geometry is considered in the main text. In both cases the drifts are comparable.

$$dU = F[\Delta l]d\Delta l = A \left(\sigma_0 + \frac{\Delta l}{l} E \right) d\Delta l \quad (\text{G.6})$$

Replacing elongation by amplitude, $a[\Delta l]$, one obtains up to $o[(a/l)^4]$:

$$dU = A \left(\sigma_0 + E \frac{\pi^2 a^2}{4l^2} \right) \left(\frac{\pi^2 a}{2l} - \frac{3\pi^4 a^3}{8l^3} \right) da \quad (\text{G.7})$$

The restoring force divided by the effective mass of the oscillator $m_{\text{eff}} = 1/2\rho Al$ therefore writes

$$\frac{F[a]}{m_{\text{eff}}} = \frac{1}{m_{\text{eff}}} \frac{dU}{da} = \frac{\pi^2 \sigma_0}{\rho l^2} a + \left(\frac{\pi^4 E}{4\rho l^4} - \frac{3\pi^4 \sigma_0}{4\rho l^4} \right) a^3 \quad (\text{G.8})$$

From the first term, one can easily deduce the resonance frequency of a string ($f = 1/(2l)\sqrt{\sigma_0/\rho}$); the residual terms are the cubic corrections. The first term in the brackets arises as the stress increases under elongation, the second is a correction of the amplitude-dependent elongation; as $\sigma_0 \ll E$ it can be safely neglected.

G.4 Supplement to On-chip Detection

G.4.1 Device Dimensions

In order to compare our results to (potential) future work, the device geometry is given in greater detail here. It is displayed in Fig.G.3, which was taken under an angle of 45 degrees. The beam dimensions are $100 \cdot 200 \text{ nm}$ (height, width, respectively). The underlying gold electrodes are placed symmetrically beneath the resonator with a distance of 350 nm below the bottom of the resonator. The holes in the silicon dioxide are patterned with a rectangular PMMA etch mask of dimensions $2 \cdot 1.5 \mu\text{m}$ (x-, y-direction). The resulting depressions reflect these dimensions, yet the expected edges are significantly rounded with a radius of curvature of 400 nm . From the upper corner, the depressions lower with a constant slope through the remaining silicon dioxide of 50 nm thickness to the underlying silicon within a vertical distance of 300 nm . The resulting area of the exposed silicon is an ellipse of dimensions $400 \cdot 900 \text{ nm}$ (x-, y-direction), which is half covered by the gold electrodes. The area of the Schottky contact is therefore approximately $0.3 \mu\text{m}^2$.

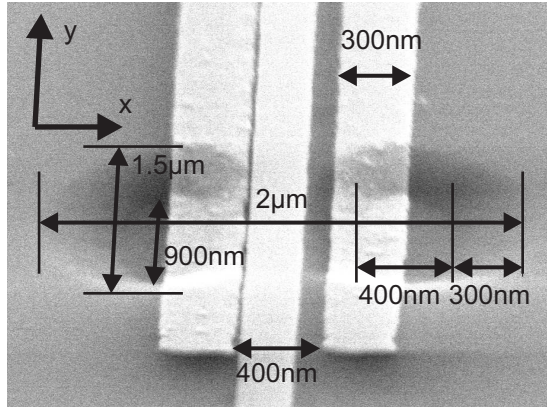


Figure G.3: Dimensions of the Schottky contact and its surroundings

G.4.2 Heating of the beam

We apply a simple model calculation in order to exclude heating effects of the beam. Reported absorption coefficients for silicon nitride [3] do not exceed 1 dB/cm , this number translates into an absorbed fraction of 10^{-6} when passing through 100 nm as in our experiment. The absorbed power is therefore lower than $P_{\text{ab}} = P_{\text{in}} \cdot 10^{-6} = 1 \text{ nW}$. To estimate the effect of heating, we apply a rough model by assuming that half of the beam (centered around its midpoint) has uniformly elevated temperature. Assuming the residual beam to be the bottleneck of heat transportation yields a temperature change of $(A, l$ are cross sectional area and residual beam length; see

name	character	value
Young's Modulus	E	100 GPa
tensile stress	σ_0	830 MPa
coefficient of thermal expansion	α	$3.3 \cdot 10^{-6}/\text{K}$
thermal conductivity	c	15 W/(m K)
cross sectional area	A	$0.1 \cdot 0.2 \mu\text{m}^2$
residual beam length	l	$0.5 \cdot 35 \mu\text{m}$
incident optical power	P_{in}	1 mW
frequency shift	δf	700 Hz

Table G.2: Beam parameters

also Table G.4.2)

$$\Delta T = \frac{1}{2} \frac{P_{\text{abl}} l / 2}{c A} \approx 15 \text{ mK} \quad (\text{G.9})$$

We now calculate the temperature difference necessary to cause the observed frequency shift. We consider only the effect of the uniformly warmer part of the resonator. It has been shown, that the resonance frequency of the beam is dominated by the high built-in stress [4]; from which we also obtain the elastic parameters E , σ . As the frequency is proportional to the square root of the stress, one obtains (see Table G.4.2)

$$\begin{aligned} \frac{\delta f}{f} &= \frac{1}{2} \frac{\delta \sigma}{\sigma} = \frac{E \alpha T}{4 \sigma} \\ T &= 4 \frac{\delta f}{f} \frac{\sigma}{E \alpha} \approx 1 \text{ K} \end{aligned} \quad (\text{G.10})$$

A rise in temperature of 1 K is therefore required to explain the observed shift in resonance frequency with illumination intensity in clear contrast to the above estimate.

G.5 Perturbation solution of the Duffing equation

As this calculation can be found in detail in textbooks [5] and publications [6], the focus here is to legitimate the utilized simplifications. The Duffing equation writes (please note that in order to be consistent with the publication, $x[t]$ denotes now the displacement, complementary to the previous sections, $Q, \omega_0, \alpha_3, \sigma, k$ are quality factor, (angular) resonance frequency, nonlinear restoring component, detuning from resonance and actuation strength):

$$x''[t] + \frac{\omega_0}{Q}x'[t] + \omega_0^2x[t] + \alpha_3x[t]^3 = k \cos[(\omega_0 + \sigma)t] \quad (\text{G.11})$$

We seek resonant solutions when actuating close to the eigenfrequency $\omega \approx \omega_0$, equation. Rewriting the restoring force yields:

$$\frac{F}{m} = \omega_0^2x[t] + \alpha_3x[t]^3 = \omega_0^2 \left(1 + \frac{\alpha_3}{\omega_0^2}x[t]^2 \right) x[t] \quad (\text{G.12})$$

One can therefore regard the action of the nonlinearity as to detune the natural resonance frequency with increasing amplitude. We shall treat the actuation regime in which the detuning is small $1 \gg \alpha_3x[t]^2/\omega_0^2$. Close to the eigenfrequency the amplitude of the oscillation is enhanced (up to the quality factor Q). Hence in eq. G.11, the actuation term is small when compared with the kinetic or elastic term $x''[t], \omega_0^2x[t] \ll k$. Therefore we expand the differential equation to write:

$$x''[t] + \epsilon \frac{\omega_0}{Q}x'[t] + \omega_0^2x[t] + \epsilon\alpha_3x[t]^3 = \epsilon k \cos[(\omega + \sigma)t] \quad (\text{G.13})$$

To lowest order, the solution is a fast oscillation multiplied by a slowly varying (complex) amplitude, this shall be emphasized by introducing another ϵ in the argument. The introduction of ϵ merely helps to sort the terms, later on it will be set to 1.

$$x[t] = A[\epsilon t] \exp[i\omega_0 t] + c.c. + \epsilon x_1[t] \quad (\text{G.14})$$

In table G.3 all these perturbation simplifications are listed, including approximate experimental values. The ansatz is chosen to solve eq. G.13 to lowest order (ϵ^0). The equation linear in ϵ is regarded, for simplification a new time variable is introduced $t_1 \equiv \epsilon t$.

$$2i\omega_0 A'[t_1] + 3\alpha_3 A[t_1]^2 A^*[t_1] + i\frac{1}{Q}\omega_0 A[t_1] - \frac{1}{2}k \exp[i\sigma t_1] = 0 \quad (\text{G.15})$$

As the response is thereby separated into several time scales, the applied approximation is called "Method of Multiple Scales".

To (analytically) solve the algebraic equation, $A[t_1] \exp[i\omega_0 t]$ is chosen to yield a resonant oscillation; ϵ is now set to 1, thereby $t_1 = t$.

$$A[t] = \frac{1}{2} (a[t] \exp[i(\sigma t - \gamma[t])] + c.c.) \quad \text{with } a[t], \gamma[t] \text{ real} \quad (\text{G.16})$$

One therefore arrives at the two coupled equations ($f = 1/(2\pi)(\omega_0 + \sigma)$: actuation frequency) that describe amplitude and phase of the oscillation ($x[t] = a[t] \cos[2\pi f t + \gamma[t]]$).

$$\begin{aligned}
a'[t] &= -\frac{\pi f_0 a[t]}{Q} + \frac{k \sin[\gamma[t]]}{4\pi f_0} \\
\gamma'[t] &= 2\pi(f - f_0) - \frac{3\alpha_3 a[t]^2}{16\pi f_0} + \frac{k \cos[\gamma[t]]}{4\pi f_0 a[t]}
\end{aligned} \tag{G.17}$$

To calculate the steady-state response, one sets $a'[t] = \gamma'[t] = 0$ in eq. G.17. The resulting cubic equation can be analytically solved [6] (even avoiding complex numbers), yet the solution is somewhat lengthy and shall not be given here.

designation	simplification	experimental value
small detuning	$\alpha_3/\omega_0^2 x[t]^2 \ll 1$	1/1000
high Q	$1/Q \ll 1$	1/10000
near resonance	$ f - f_0 \ll f_0$	1/1000
time scales	$\partial_t A[t] \ll A[t] f_0$	1/1000

Table G.3: **Perturbation Approximations and their relative strength**

G.6 Supplement to Damping Characteristics

G.6.1 Damping Model

In a Zener model, an oscillating strain $\epsilon(t) = \Re[\epsilon[\omega] \exp[i\omega t]]$ and its accompanying stress $\sigma[t] = \Re[\sigma[\omega] \exp[i\omega t]]$ are out-of phase, described by a frequency-dependent, complex elastic modulus $\sigma(\omega) = E[\omega]\epsilon[\omega] = (E_1[\omega] + iE_2[\omega])\epsilon[\omega]$. This leads to an energy loss per oscillation in a test volume $\delta V = \delta A \cdot \delta s$ of cross-section δA and length δs .

$$\Delta U_{\delta V} = \int_T dt \underbrace{EA\epsilon[t]}_{\text{force}} \cdot \underbrace{\frac{\partial}{\partial t}(s\epsilon[t])}_{\text{velocity}} = \pi \delta A \delta s E_2 \epsilon^2 \tag{G.18}$$

We now employ this model for our case, namely a pre-stressed, rectangular beam of length l , width w and height h , corresponding here to the x,y,z-direction, respectively. The origin of the coordinate system is centered in the beam. The resonator performs oscillations in the z-direction and, as we consider a continuum elastic model, there will be no dependence on the y-direction. For a beam of high aspect ratio $l \gg h$ and small oscillation amplitude, the displacement of the m -th mode can be approximately written $u_m[x, y, z] = u_m[x]$. During oscillation, a small test volume within the beam undergoes oscillating strain $\epsilon_m[x, z, t]$.

This strain arises because of the bending of the beam as well as its elongation as it is displaced. The stress caused by the overall elongation is quadratic in displacement,

therefore it occurs at twice the oscillating frequency.

$$\begin{aligned}\epsilon_m[x, z, t] &= \underbrace{\frac{1}{2} \left(\frac{\partial}{\partial x} u_m[x] \Re[\exp[i\omega t]] \right)^2}_{\text{elongation}} + \underbrace{z \frac{\partial^2}{\partial x^2} u_m[x] \Re[\exp[i\omega t]]}_{\text{bending}} \\ &= \frac{1}{2} \left(\frac{\partial}{\partial x} u_m[x] \right)^2 \frac{1}{2} (1 + \Re[\exp[2i\omega t]]) + z \frac{\partial^2}{\partial x^2} u_m[x] \Re[\exp[i\omega t]] \quad (\text{G.19})\end{aligned}$$

Inserting this into eq. G.18 and integrating over the cross-section $w \cdot h$, the accompanying energy losses can be seen to separate into elongation and displacement caused terms.

$$\Delta U_{w \cdot h} = \pi s E_2 [2\omega] \frac{wh}{8} \left(\frac{\partial}{\partial x} u_m[x] \right)^4 + \pi s E_2 [\omega] \frac{wh^3}{12} \left(\frac{\partial^2}{\partial x^2} u_m[x] \right)^2 \quad (\text{G.20})$$

Integrating over the length yields the total energy loss of a particular mode $\Delta U = \int_{-l/2}^{l/2} dx \Delta U_{w \cdot h}$. In the case that E_2 is only weakly frequency-dependent, it turns out that for our geometries the elongation term is several orders of magnitude ($10^5 - 10^7$) smaller than the term arising from the bending. The energy loss therefore may be simplified and writes

$$\Delta U \approx \Delta U_{\text{bending}} = \pi E_2 \frac{wh^3}{12} \int_{-l/2}^{l/2} dx \left(\frac{\partial^2}{\partial x^2} u_m[x] \right)^2 \quad (\text{G.21})$$

G.6.2 Elastic Energy of a Pre-Stressed Beam

A volume δV subject to a longitudinal pre-stress σ_0 stores the energy $U_{\delta V}$ when strained; E_1 is assumed to be frequency independent in the experimental range (5-100 MHz)

$$U_{\delta V} = sA \left(\sigma_0 \epsilon + \frac{1}{2} E_1 \epsilon^2 \right) \quad (\text{G.22})$$

To apply this formula to the case of an oscillating pre-stressed beam, we insert eq. G.19| $_{t=0}$ (maximum displacement) and integrate over the cross-section to obtain

$$U_{w \cdot h} = \frac{1}{2} E_1 \left(\frac{1}{4} wh \left(\frac{\partial}{\partial x} u_m[x] \right)^4 + \frac{1}{12} wh^3 \left(\frac{\partial^2}{\partial x^2} u_m[x] \right)^2 \right) + \frac{1}{2} swh \sigma_0 \left(\frac{\partial}{\partial x} u_m[x] \right)^2 \quad (\text{G.23})$$

Analog to eq. G.20 we can omit the first term in the brackets; integrating over the length yields

$$U \approx \int_{-l/2}^{l/2} dx \left(\underbrace{\frac{1}{2} wh \sigma_0 \left(\frac{\partial}{\partial x} u_m[x] \right)^2}_{\text{elongation}} + \underbrace{\frac{1}{24} E_1 wh^3 \left(\frac{\partial^2}{\partial x^2} u_m[x] \right)^2}_{\text{bending}} \right) \quad (\text{G.24})$$

We can therefore divide the total energy into parts arising from the elongation and the bending of the beam. Depending on the magnitude of the pre-stress, either of the two energies can dominate as seen in Fig. 3a of the main text. We have checked that the kinetic energy $U_{\text{kin}} = 1/2\rho(\omega_m)^2 \int_{l/2}^{l/2} dx (u_m[x])^2$; ($\omega_m/(2\pi)$, ρ : resonance frequency, material density, respectively) equals the total elastic energy, as expected.

G.6.3 Frequency-dependent Loss Modulus

There is no obvious reason that the imaginary part of Young's modulus E_2 should be completely frequency-independent. We therefore assume that E_2 obeys a (weak) power-law and chose the ansatz:

$$E_2[f] = E_2(f/f_0)^a \quad (\text{G.25})$$

Fitting our data with the thus extended theory, we achieve a very precise agreement of measured and calculated quality factors, as seen in Fig. S1. The resulting exponent is $a = 0.075$; E_2 varies therefore by 20% when f changes by one order of magnitude.

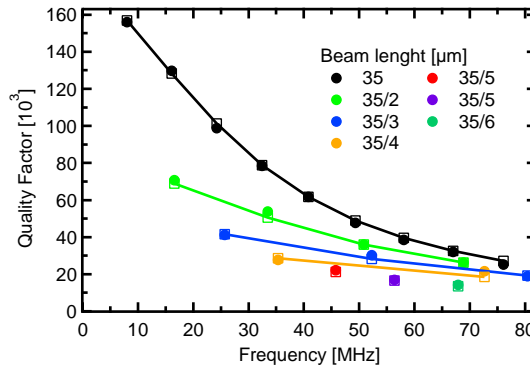


Figure G.4: **Resonance frequencies and quality factors of the resonators**
 a Measured quality factor and resonance frequency of several harmonics of beams with different lengths (color-coded) are displayed as filled circles (same data as in Fig. 2 of the main text). The resonance frequencies are reproduced by a continuum model; we calculate the quality factors using a model based on the strain caused by the displacement. In contrast to Fig. 2 of the main text and Fig. S2 we here allow E_2 to be (weakly) frequency-dependent.

G.6.4 Linewidth of the Mechanical Resonance

The elastic energy of a harmonic oscillator is given by $U = 1/2m_{\text{eff}}\omega_0^2x_0^2$ with m_{eff} , ω_0 , x_0 being effective mass, resonance frequency and displacement, respectively.

If we assume the effective mass to be energy-independent, it applies $\omega_0 \propto \sqrt{U}$. Recalling the definition of the quality factor $Q = 2\pi U/\Delta U \propto U$, one obtains for the for the Full Width at Half Max (FWHM) of the resonance

$$\Delta\omega = \frac{\omega_0}{Q} \propto \frac{\sqrt{U}}{U/\Delta U} = \frac{\Delta U}{\sqrt{U}} \quad (\text{G.26})$$

As in the main text, the energy depends on the applied overall tensile stress. Figure G.5 shows a numerical calculation of the resulting linewidth vs. applied stress; one can see that increase in energy loss per oscillation is dominated by the increase in energy, resulting in a decreased linewidth. The exact effective mass is included in this calculation; as it changes by less than 20%, the above assumption is justified.

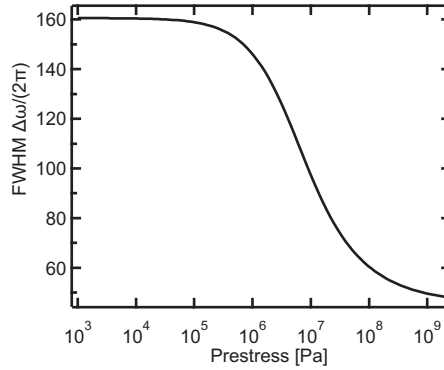


Figure G.5: **Linewidth of the mechanical resonance** The calculated linewidths (FWHM) for the fundamental mode of the beam with $l = 35\mu\text{m}$ are displayed vs. applied overall stress.

G.6.5 Microscopic Damping Mechanisms

We start with clamping losses as discussed, e.g., in ref. [7, 8], i. e. the radiation of acoustic waves into the bulk caused by inertial forces exerted by the oscillating beam. With a sound velocity in silicon of $v_{\text{Si}} \approx 8\text{ km/s}$, the wavelength of the acoustic waves radiated at a frequency of 10 MHz from the clamps into the bulk will be greater than $500\mu\text{m}$, and thus substantially larger than the length of our resonators. Considering each clamping point as a source of an identical wave propagating into the substrate, one would expect that mostly constructive/destructive interference would occur for in-/out-of-phase shear forces exerted by the clamping points, respectively. With clamping losses being important, one would therefore expect that spatially asymmetric modes with no moving center of mass exhibit significant higher quality factors than symmetric ones^a. Another way to illuminate this difference is that

^aI. Wilson-Rae, private communication

symmetric modes give rise to a net force on the substrate, whereas asymmetric modes yield a torque. Since the measurement (Fig. 2) does not display such an alternating behavior of the quality factors with mode index m (best seen for the longest beam), clamping losses are likely to be of minor importance.

The next damping mechanism we consider are phonon-assisted losses within the beam. At elevated temperatures, at least two effects arise, the first being thermoelastic damping: because of the oscillatory bending, the beam is compressed and stretched at opposite sides. Since such volume changes are accompanied by work, the local temperature in the beam will deviate from the mean. For large aspect ratios as in our case, the most prominent gradient is in the z direction. The resulting thermal flow leads to mechanical dissipation. We extend existing model calculations [9] to include the tensile stress of our beams. Using relevant macroscopic material parameters such as thermal conductivity, expansion coefficient and heat capacity we derive Q -values that are typically three to four orders of magnitudes larger than found in the experiment. Therefore, heat flow can be safely neglected as the dominant damping mechanism. In addition, the calculated thermal relaxation rate corresponds to approximately 2 GHz, so the experiment is in the so-called adiabatic regime. Consequently, one would expect the energy loss to be proportional to the oscillation frequency, in contrast to the assumption of a frequency independent E_2 and our experimental findings.

Another local phonon-based damping effect is the Akhiezer-effect [10]; it is a consequence of the fact that phonon frequencies are modulated by strain, parameterized by the Grüneisen tensor. If different phonon modes (characterized by their wave vector and phonon branch) are affected differently, the occupancy of each mode corresponds to a different temperature. This imbalance relaxes towards a local equilibrium temperature, giving rise to mechanical damping. In a model calculation applying this concept to the oscillatory motion of nanobeams [11], the authors find in the case of large aspect ratios length/height that the thermal heat flow responsible for thermoelastic damping dominates the energy loss by the Akhiezer effect. We thus can safely assume this mechanism to be also negligible in our experiment.

G.6.6 Reduced Quality Factor

We fabricated a set of resonators, shown in Fig. S1a, that showed lower quality factors than the ones presented in the main text (Fig. 2); we attribute this reduction to a non-optimized RIE-etch step. As in the main article, it is possible to reproduce the quality factors using a single fit parameter, namely the imaginary part of Young's modulus E_2 . The ratio of the two sets of quality factors is displayed in Fig. S1 b and can be seen to be around 1.4 with no obvious dependence on resonance frequency, mode index or length. A non-optimized etch step causes additional surface roughness and the addition of impurities, thereby increasing the density of defect states. As there is no obvious reason why another damping mechanism should be thereby influenced, we interpret this as another strong indication that the dominant

microscopic damping mechanism is caused by localized defect states.

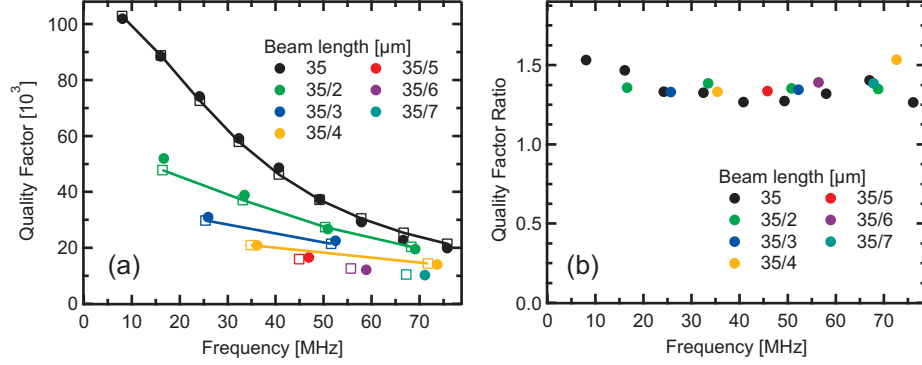


Figure G.6: **Comparison of the resonance frequencies and quality factors of the sets of resonators** **a** Measured quality factor and resonance frequency of several harmonics of beams with different lengths (color-coded) are displayed as filled circles. The resonance frequencies are reproduced by a continuum model; a model based on the strain caused by the displacement allows us to calculate the quality factors, shown as hollow squares. The uniform reduction of the Q-factors is attributed to a non-optimized RIE-etch. **b** The ratio of the quality factors of the two sets resonators (Fig. 2 main article and Fig. S2a) are displayed vs. frequency, being approximately constant.

G.6.7 Spatially Inhomogeneous Loss Modulus

Our model calculation assumes a spatially homogeneous imaginary Young's Modulus E_2 . In the view of thickness-dependent quality factors of Micro-Cantilevers [12] and our own experimental findings, we show that a generalization has no influence to our model.

We let E_2 now depend on the position along the direction of displacement of the resonator $E_2 = E_2[z]$. The elastic energy is obviously not affected. The energy loss now reads with $\epsilon[x, z] \equiv z\epsilon_0[x]$:

$$\Delta U = \pi \int_V E_2[z] \epsilon[x, z]^2 = \pi w \int_{-h/2}^{h/2} dz z^2 E_2[z] \cdot \int_{-l/2}^{l/2} dx \epsilon_0[x]^2 \quad (\text{G.27})$$

The integral can be separated into the x and z direction; we now regard the ratio of two different modes (i, j) with the same $E_2[z]$ (irrespective of whether the indices refer to different harmonics or beam lengths):

$$\frac{\Delta U_i}{\Delta U_j} = \frac{\int_h dz z^2 E_2[z]}{\int_h dz z^2 E_2[z]} \cdot \frac{\int_l dx \epsilon_{i,0}^2}{\int_l dx \epsilon_{j,0}^2} \quad (\text{G.28})$$

The ratio of the energy loss and therefore the quality factors can be seen not to be influenced by the exact z -dependence, the same applies if one regards $E_2 = E_2[y]$. In other words, our model will hold true for any variance but cannot resolve these either.

G.7 Nonlinear Damping

In this chapter, we will further specify the contributions of the neglected terms in the damping (eq. G.18) and stored energy (eq. G.19). The neglected terms constitute the slope of the spatial profile; it is on the order of "amplitude/anti-node separation" and therefore much less than one. These terms enter the equation to the fourth order in oscillation amplitude whereas the dominant ones are quadratic. At moderate amplitudes they can therefore be safely neglected.

Yet at high amplitudes their contribution increases; Figs. G.7(a,b) show a calculation of the energies (dissipations) involved vs. oscillation amplitude. At high amplitudes, the quality factor (i.e. the ratio of the sums of both) can be seen to degrade at high amplitudes, see Fig. G.7(c).

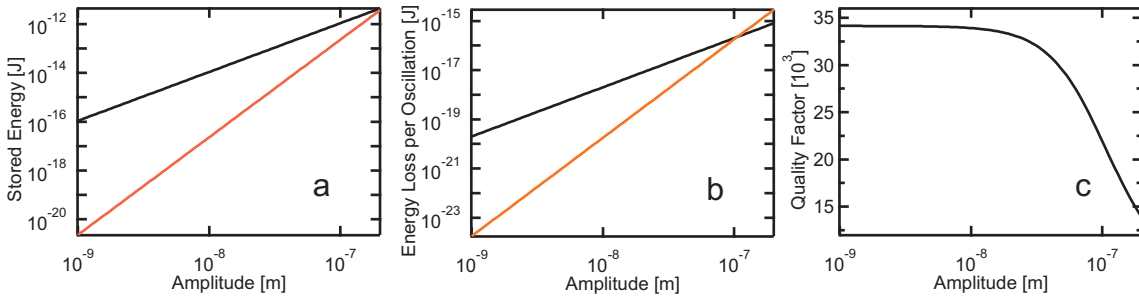


Figure G.7: **(Non)linear Energies and Losses** The calculated elastic energies **a**, energy losses **b** are shown vs. oscillation amplitude, separated into linear (black) and nonlinear (red) constitutes. The 9th harmonic of a 35 μm beam is regarded. **c** The resulting quality factor exhibits clear deviations at large amplitudes.

Yet, in complete analogue to the hardening string (see chapters 2,G.3) nonlinear effects set in, the critical amplitude (the onset of bistability) can be calculated from the data in Fig. G.7(b). The restoring force of a nonlinear oscillator is integrated to yield the energy (see eq. G.11).

$$\frac{F}{m} = \omega_0^2 x + \alpha_3 x^3 \Rightarrow U = \underbrace{\frac{1}{2} m \omega_0^2 x^2}_{\equiv U_2[x]} + \underbrace{\frac{1}{8} m \alpha_3 x^4}_{\equiv U_4[x]} \quad (\text{G.29})$$

The critical amplitude writes [5]:

$$x_{\text{crit}} = \frac{2\sqrt{2}\omega_0}{3^{3/4}\sqrt{Q}\alpha_3} = x\sqrt{\frac{U_2}{U_4}} \frac{\sqrt{2}}{3^{3/4}\sqrt{Q}} \quad (\text{G.30})$$

From the figure it can be estimated that at an amplitude of ≈ 200 nm the energies are equal; one therefore calculates a critical amplitude of 0.8 nm. However, a clear deviation in quality factor requires 50 nm amplitude, almost two orders of magnitude higher and therefore difficult to measure. The hysteresis at that amplitude can be estimated with a similar calculation to be approximately 1 MHz.

References

- [1] W. Weaver, S. P. Timoshenko, and D. H. Young, *Vibration Problems in Engineering* (Wiley, New York, 1990).
- [2] C. A. Regal, J. D. Teufel, and K. W. Lehnert, “Measuring nanomechanical motion with a microwave cavity interferometer” *Nat. Phys.* **4**, 555 (2008).
- [3] N. Daldosso, M. Melchiorri, F. Riboli, F. Sbrana, L. Pavesi, G. Pucker, C. Kom-pocholis, M. Crivellari, P. Bellutti, and A. Lui, “Fabrication and optical characterization of thin two-dimensional Si₃N₄ waveguides” *Mat. Sci. Semicon. Proc.* **7**, 453–458 (2004).
- [4] Q. P. Unterreithmeier, S. Manus, and J. P. Kotthaus, “Coherent detection of nonlinear nanomechanical motion using a stroboscopic downconversion technique” *Appl. Phys. Lett.* **94**, 263 104 (2009).
- [5] A. H. Nayfeh and D. T. Mook, *Nonlinear Oscillations* (Wiley, New York, 1995).
- [6] B. Yurke, D. S. Greywall, A. N. Pargellis, and P. A. Busch, “Theory of amplifier-noise evasion in an oscillator employing a nonlinear resonator” *Phys. Rev. A* **51**, 4211–4229 (1995).
- [7] Z. Hao, A. Erbil, and F. Ayazi, “An analytical model for support loss in micro-machined beam resonators with in-plane flexural vibrations” *Sens. Actuators, A* **109**, 156–164 (2003).
- [8] I. Wilson-Rae, “Intrinsic dissipation in nanomechanical resonators due to phonon tunneling” *Phys. Rev. B* **77**, 245 418 (2008).
- [9] R. Lifshitz and M. L. Roukes, “Thermoelastic damping in micro- and nanomechanical systems” *Phys. Rev. B* **61**, 5600–5609 (2000).
- [10] A. Akhiezer, “On the absorption of sound in solids” *J. Phys. - USSR* **1**, 277–287 (1939).
- [11] A. A. Kiselev and G. J. Iafrate, “Phonon dynamics and phonon assisted losses in Euler-Bernoulli nanobeams” *Phys. Rev. B* **77**, 205 436 (2008).
- [12] K. Y. Yasumura, T. D. Stowe, E. M. Chow, T. Pfafman, T. W. Kenny, B. C. Stipe, and D. Rugar, “Quality factors in micron- and submicron-thick cantilevers” *J. Microelectromech. S.* **9**, 117–125 (2000).

References

Danksagung

Mehreren Personen möchte ich für das Gelingen der vorliegenden Arbeit danken.

Mein ganz besonderer Dank gilt Prof. Jörg Kotthaus, der mir ermöglicht hat an seinem Lehrstuhl die Promotion durchzuführen. Obwohl die Zusammenarbeit mit einigen Anfangsschwierigkeiten versehen war, ist es nicht zuletzt seiner Philantropie, seinem verblüffenden Langmut, physikalischem Überblick und unermüdlichen Einsatz zuzuschreiben, dass die vorliegende Arbeit gelingen konnte.

Thomas Faust hat erst als Werkstudent und dann als Diplomand die Arbeit begleitet und wesentlich zu den (Mess-)ergebnissen beigetragen.

Eva Weig hat das Projekt des dielektrischen Antriebes mitgetragen, auch hierfür mein herzlicher Dank.

Stephan Manus hat mit großer Erfahrung zu fast jedem Projekt elektrische Schaltungen und Know-How zur Verfügung gestellt, die dadurch erst ermöglicht wurden.

Prof. Florian Marquardt und Ignacio Wilson-Rae möchte ich für ihre Diskussions über das Dämpfungsprojekt danken.

Einige Mitglieder des Lehrstuhles versehen (mehr oder weniger im Hintergrund) die Aufgabe, den Betrieb am Laufen zu halten. Hier ist (wie so oft) Bert Lorentz zu Danken der das Tagesgeschäft bis zu Kämpfen gegen die Gebäudeverwaltung mit großer Geduld führt. Martina Jüttner stellt mit unbürokratischem Einsatz eine sehr hilfreiche Schnittstelle zur Verwaltung und administrativen Problemen dar. Philipp Altpeter und Reinhold Rath, die mit bisher nicht gekanntem Einsatz und Kompetenz das reibungslose Arbeiten im Reinraum ermöglichen. Wolfgang Kurpas und Pit haben sich um technische Belange und Heliumversorgung gekümmert. Daniela Taubert hat mit beeindruckendem Sachverstand und großer Hilfsbereitschaft das Management der Computer-Administration zunehmend übernommen, ihr gilt mein ganz besonderer Dank.

Einige Kollegen des Lehrstuhles haben besonders dazu beigetragen, eine gute Atmosphäre zu schaffen; aufgrund einer längeren Liste wird (halbwegs) chronologisch geordnet: Clemens, Martin, Georg und Xaver haben durch ihre stets gute Laune Heiterkeit verbreitet. Die Mitglieder der Kaffeerrunde: Daniel, Johannes, Gunnar, Eric, Jan und Thomas für erbauliches Fett-Ansetzen im fröhlichen Miteinander.

Und schließlich meinen Eltern, die mir mein Studium ermöglicht haben, meiner

gesamten Familie für ihre Wärme und Anteilnahme.

Lebenslauf

Quirin Unterreithmeier, geboren am 02.09.1979 in Augsburg, Deutschland, ledig.

- 1986 - 1990** Friedrich-Ebert Grundschule Augsburg
- 1990 - 1999** Holbein Gymnasium Augsburg
- 1999** Abitur
- 1999 - 2000** Grundwehrdienst in der Bundeswehr
- 2000 - 2007** Physikstudium an der Technischen Universität München
- 2002** Vordiplom
- 2004 - 2005** Auslandsstudium an der Université Joseph Fourier, Grenoble
- 2006 - 2007** Diplomarbeit mit dem Thema: *Charakterisierung nanomechanischer Resonatoren unter Zugspannung*
- 2007** Diplom
- 2007-2010** Promotionsstudium und wissenschaftlicher Mitarbeiter am Center for Nanoscience und Fakultät für Physik, Ludwigs-Maximilians-Universität München